

AMERICAN UNIVERSITY OF BEIRUT

EVOLUTION AND NUCLEOSYNTHESIS IN
1 TO $12M_{\text{sun}}$ STARS

by
GHINA FAWZI MAHMOUD HALABI

A dissertation
submitted in partial fulfillment of the requirements
for the degree of Doctor of Philosophy
to the Department of Physics
of the Faculty of Arts and Sciences
at the American University of Beirut

Beirut, Lebanon
December 2014

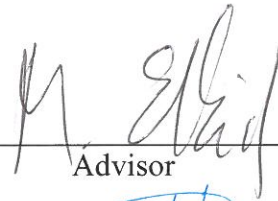
AMERICAN UNIVERSITY OF BEIRUT

EVOLUTION AND NUCLEOSYNTHESIS IN
1 TO $12M_{\text{sun}}$ STARS

by
GHINA FAWZI MAHMOUD HALABI

Approved by:

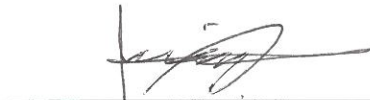
Dr. Mounib El Eid
Professor of Physics



Advisor

Dr. Jordi Jose
Professor of Physics

Member of Committee



Dr. Jihad Touma
Professor of Physics

Member of Committee



Dr. Bradley Meyer
Professor of Physics

Member of Committee



Dr. Leonid Klushin
Professor of Physics

Member of Committee

Date of dissertation defense: December 9, 2014

AMERICAN UNIVERSITY OF BEIRUT

THESIS, DISSERTATION, PROJECT RELEASE FORM

Student Name: Mahmoud Ghina Fawzi
Last First Middle

Master's Thesis Master's Project Doctoral Dissertation

I authorize the American University of Beirut to: (a) reproduce hard or electronic copies of my thesis, dissertation, or project; (b) include such copies in the archives and digital repositories of the University; and (c) make freely available such copies to third parties for research or educational purposes.

I authorize the American University of Beirut, **three years after the date of submitting my thesis, dissertation, or project**, to: (a) reproduce hard or electronic copies of it; (b) include such copies in the archives and digital repositories of the University; and (c) make freely available such copies to third parties for research or educational purposes.

Signature  Date Feb. 5. 2015

ACKNOWLEDGMENTS

... and the story has been told. Five years of work are here compiled into a 100-page book. These pages were a challenging attempt to explain my work in stellar evolution, yet they fall short of expressing the galaxy of feelings that came with it. The excitement, desperation, exuberance, hope... are property of the heart.. of another story, to be told elsewhere, somewhere.. maybe.

Feelings of gratitude, however, are due here and now, especially that the acknowledgments section is probably the most read part in a PhD thesis. I extend my deep thanks to those who undoubtedly made this work possible. Special thanks for my advisor, DR. MOUNIB EL EID. His German precision, American brevity and Lebanese humor made working with him rewarding and equally enjoyable. Thank you for your patience, support and constructive criticism. I owe you not only a large part of my experience and know-how, but also much of my enthusiasm for working in stellar evolution.

Gratitude and recognition are addressed to my committee members DR. BRAD MEYER, DR. JIHAD TOUMA, DR. JORDI JOSE and DR. LEONID KLUSHIN. Thank you for being part of this and for your feedback that greatly improved the quality of this work. I'm indebted to BRAD for his patience, continuous support and great help in improving the code. I thank JORDI for his support, positive vibes, enthusiasm and ideas; it's a pleasure to have known him and worked with him closely. I'm deeply grateful for the support that I have received from the Physics department at AUB, facilitated by the consecutive chairs DR. SAMIH ISBER and DR. GHASSAN ANTAR.

I believe the physics department owes much of its charm and dynamicity to its administrative assistant MRS. JOUMANA ABI FALAH. Thank you for being a great friend, for caring and being so ready to help. Thank you for the laughs, the vents and the good times. My 24/7 technical support however, is a couple of meters away from the physics department. SAAD ITANI, IT lab technician at the Faculty of Engineering & Architecture, thank you for being so available and for making things work like magic.

A big bunch of thanks goes to my colleagues in the department. You make the days and nights enjoyable and the long hours of work bearable. Thank you for our Abu Afif lunches, for the baseball games and dance competitions in the graduate room, for the drinks after work and the many awesome discussions about life, science and Miley Cyrus. I also owe much of my life's awesomeness to my friends. Thank you for being there and for the euphoric Sunday escapes.

As the love grows bigger, words become less. I would have never made it without the support and love of my family. This is to Nour my blueberry cheesecake, to Jad my absolute love and joy, to mom and dad.

AN ABSTRACT OF THE THESIS OF

Ghina Fawzi Mahmoud for Doctor of Philosophy
Major: Physics

Title: Evolution & Nucleosynthesis in 1 to 12 M_{sun} Stars

Physical aspects of the evolution and nucleosynthesis in stars in the mass range (1-12) M_{\odot} , where M_{\odot} denotes the solar mass, of solar-like initial composition are thoroughly investigated in this work. Stars in this mass range are very numerous in the Galaxy. They evolve after reaching the red giant branch (RGB) to the peculiar phase of asymptotic giant branch (AGB), where they exhibit thermal pulsations. These pulsations facilitate the physical conditions for the formation of about half of the trans-iron elements and their isotopes in the Galaxy via the s-process nucleosynthesis. Light elements like carbon and fluorine are also partially produced in this stellar site.

Stars in the above mass range are evolved using a well-tested hydrodynamic stellar evolution code with up-to-date physics input. The investigations were performed along different directions as follows.

(a) On the RGB phase, stars experience the first envelope mixing event that changes the surface abundances. Basic stellar parameters and surface abundances are compared with observations. This approach has improved the estimation of the stellar masses of an observed sample of red giants and helped constrain the amount of convective mixing in low mass stars.

(b) Stars of $M \geq 4M_{\odot}$ exhibit excursion in the Hertzsprung-Russell diagram to higher effective temperatures in what is called the "blue loop", which characterizes the evolution through the Cepheid instability strip. The impact of key nuclear reactions and the treatment of mixing on the characteristics of blue loops is investigated.

(c) Modeling AGB stars is challenged by the complex behavior of convective mixing during thermal pulsations. This work aims to understand the physical conditions for the operation of s-process nucleosynthesis, which requires the activation of the main neutron source via $^{13}\text{C}(\alpha, n)^{16}\text{O}$ that feeds the s-process calculation. The role of convective mixing in the formation of this neutron source is investigated and an extended nuclear reactions network was introduced to carry on the s-process nucleosynthesis calculation.

(d) The last part of the thesis investigates the complex structure and burning conditions of the upper mass range under consideration. Stars of $M \gtrsim 8M_{\odot}$ evolve to the Super AGB (SAGB) phase and either form ONe white dwarfs or undergo supernova explosion. The important role of convection and the carbon fusion reaction rate on the evolution of stars in this mass range is investigated. The final chapter provides a summary of the outcome of this work.

Contents

1	Introduction	1
1.1	Main Phases of Stellar Evolution	4
1.1.1	The Main-sequence	4
1.1.2	The Red Giant Branch	6
1.1.3	The Asymptotic Giant Branch	11
1.1.4	The Super Asymptotic Giant Branch	14
1.1.5	Observational evidence of the different evolutionary phases	14
2	Method of Calculation	16
2.1	Stellar Evolution Code	16
2.1.1	Treatment of mass-loss	17
2.1.2	Convective mixing	19
2.2	Nuclear reaction network	20
2.2.1	Reactions of the CNO cycle	21
2.2.2	Carbon-burning reaction rate	22
2.2.3	The s-process	24
3	Evolution Prior the Early-AGB phase	31
3.1	LMS: The Core Helium-flash	31
3.2	IMS: The Blue Loop	34
3.2.1	Results of the evolution during the blue loop phase	35

3.2.2	Effects of overshooting on the blue loops	37
3.2.3	Comparison with Observations	42
3.2.4	Comparison with Other Investigations	45
3.3	Red Giant Stars: Evolution & Mass Determination	47
4	Nucleosynthesis Prior the Early-AGB phase	51
4.1	CNO Surface Abundances in Red Giants	51
4.2	Overview of observations	54
4.3	Comparison with observations & other investigations	55
4.4	Calculated surface abundances with overshooting	58
4.5	Effect of modified nuclear reaction rates	61
4.5.1	Effect on the $^{16}\text{O}/^{17}\text{O}$ ratio	61
4.5.2	Effect on the $^{14}\text{N}/^{15}\text{N}$ ratio	63
5	Evolution & Nucleosynthesis in the AGB phase	66
5.1	Evolutionary Scenario	67
5.1.1	The Thermally Pulsating AGB Phase	67
5.1.2	Exploring Third Dredge Up	71
5.2	Nucleosynthesis in the AGB phase	73
5.2.1	Formation of the ^{13}C pocket	73
5.2.2	s-process nucleosynthesis	78
6	Evolution & Nucleosynthesis in the SAGB Phase	82
6.1	Evolution of a $9M_{\odot}$ star	83
6.1.1	The carbon-burning phase	86
6.2	Effect of the $^{12}\text{C}+^{12}\text{C}$ fusion rate on M_{up}	91
6.3	Effect of core overshooting	92
6.4	Comments on the effect of mass-loss	92

7 Conclusion & Future Work	94
7.1 Summary	94
7.2 Future Work	98
Appendix 1	100
Appendix 2	105
Appendix 3	116

List of Figures

1-1	A schematic diagram showing the different burning phases and final stages experienced by solar metallicity stars according to their initial mass. Note that the transition masses are sensitive to model assumptions and subject to modification. A similar figure can be found in Karakas & Lattanzio (2014).	2
1-2	Reactions involved in the branchings of the proton-proton chain (Guenther & Demarque 1997).	4
1-3	The CNO cycle(s). Unstable isotopes are represented by dashed circles, and the dashed line shows leakage out of the chains (Arnould et al. 1999).	5
1-4	Energy generation rate by the CNO cycle and pp chain. The pp chain dominates in the lower temperature range and for stars of masses $\lesssim 1.5M_{\odot}$, while the CNO cycle is the dominant source for higher temperatures. The transition temperature is about 18×10^6 K. (Retrieved from https://people.nsl.msu.edu).	6
1-5	The evolution of a $5M_{\odot}$ star in the HR diagram, see text.	7
1-6	Upper panel: The evolution of the convective structure of a $5M_{\odot}$ star. Black regions are convective and white regions are radiative. Lower panel: the hydrogen luminosity (red), helium luminosity (blue) and the total star's luminosity (black). The numbers marked correspond to the same numbers in Fig. 1-5.	9
1-7	A schematic representation of the synthesis of ^{12}C (Rolfs & Rodney 1988).	11

1-8	Fractional mass reached by the convective envelope at FDUP (dashed line) and SDUP (solid line). SDUP is deeper only in models of stellar masses $> 4M_{\odot}$. M_{DUP} is the mass shell reached by the dredge up.	12
1-9	The HR-diagram of the globular cluster M3 showing the visible magnitude versus the color index B-V. The positions of the main-sequence, the red giant branch (RGB), the horizontal branch (HB), and the asymptotic giant branch (AGB) are indicated (Lattanzio & Wood 2004).	15
2-1	The mass-loss rates in a $3M_{\odot}$ sequence vs. the Mira pulsational period as compared to the observed mass-loss rates labeled in the upper left panel. The mass-loss rate predicted by our calculation is consistent with the two mass-loss regimes experienced by these giants. See text for more details.	18
2-2	The $^{12}\text{C}+^{12}\text{C}$ reaction rates used in this work.	23
2-3	The rates in Fig. 2-2 are shown normalized to the CF88 rate.	23
2-4	Simple chain along the s-process path in the Z-N diagram.	25
2-5	The s-process path (solid line) in a Z-N diagram. The s-process follows closely the valley of β -stability, bypassing the r- and p-process nuclei (Rolfs & Rodney 1988).	25
2-6	The product of the neutron-capture cross section and the solar system abundances, relative to $\text{Si}=10^6$ (σN), as a function of the atomic mass of s-only nuclei. The solid lines represent theoretical calculations for a single exponential distribution of neutron exposure, and for the sum of two such distributions (Rolfs & Rodney 1988).	28
2-7	Cosmic abundances of the heavy elements as a function of the atomic weight. Nuclei with closed neutron shells ($N=50, 82$ and 126) show narrow abundance peaks. Broader peaks correspond to nuclei 4-10 mass units below the closed neutron shells (Rolfs & Rodney 1988).	29

3-1	Selected evolutionary tracks of sequences in the mass range $1.2 - 7.3M_{\odot}$ (as indicated), calculated from the main sequence to the Early-AGB phase.	32
3-2	Evolutionary sequences in the $T_c - \rho_c$ plane for selected stellar masses as indicated. The lines marked by the degeneracy parameter η indicate the regions of increasing degeneracy.	33
3-3	Evolution of the star's luminosity and the luminosities due to hydrogen and helium burning during the core helium flash in a $2M_{\odot}$ sequence. Time is set to zero at central He ignition.	33
3-4	Evolutionary tracks in the HR diagram for the indicated stellar masses evolved from the zero-age main sequence till the end of core helium burning. The only difference between the two cases is the used N14 rate: N-rate (left), C-rate (right). See text.	36
3-5	Evolutionary tracks of stars of masses $5M_{\odot}$ (dashed line), $6M_{\odot}$ (solid line) and $7M_{\odot}$ (dot-dashed line) for values of γ_{ov} as indicated, with $f = 0.25$. See text.	38
3-6	Energy generation rate by H-shell burning (E_H), temperature profile (T) and the hydrogen profile (X_H) as a function of interior mass of the considered $6M_{\odot}$ star for $\gamma_{ov} = 0$ (sequence A, solid lines) and 0.5 (sequence B, dashed lines). The snapshot is taken at $X_c(\text{He}) = 0.5$ for both sequences, which marks the onset of the loop in sequence B. Note that the hydrogen abundance is shifted upwards to $2X_H + 6$ in order to match the scale of the right-side axis.	39
3-7	Same as Figure 3-6, but for sequence B with $\gamma_{ov} = 0.1$ (dashed lines) and sequence C with $\gamma_{ov} = 0.5$ (solid lines). The snapshot is taken at $X_c(\text{He}) = 0.5$ which marks the onset of the loop in sequence B.	40
3-8	The evolutionary sequences calculated with the C-rate, and with $\gamma_{ov} = 0.1$. Note how the previously suppressed loops are now restored.	40

3-9	Left panel: The loop of a $6M_{\odot}$ in the standard calculation (solid line) and with core and envelope overshooting (dashed line). Right panel: Same as Fig. 3.6, calculated with the C-rate for the two cases: standard calculation (solid lines) and with core and envelope overshooting (dashed lines). . . .	41
3-10	Sequences of mass $5-12M_{\odot}$ obtained with the C-rate and $\gamma_{ov} = 0.1$. The triangles denote the observed Galactic Classical Cepheids by Fernie et al. (1995). Observations by Schmidt (1984) are indicated by asterisks and closed circles which represent Cepheid stars and yellow giants in open clusters respectively. The temperature range of the instability strip predicted by the models agrees with that of the observed Cepheids and yellow giants.	43
3-11	The luminosities and the range of the instability strip of the predicted models (a) to (e) shown in Table 3.2. Circles mark the blue edge, while triangles mark the red edge. The initial masses of the models are also shown, while the masses of the evolved models (M_{RGB}) are listed in Table 3.2.	46
3-12	The bolometric magnitude (M_{bol}) versus effective temperature (T_{eff}) diagram showing evolutionary tracks of stars of mass $(1.2-7)M_{\odot}$. Observations by Tsuji08 are also shown.	48
3-13	The evolutionary tracks covering advanced phases together with the observed red giants, see text.	49
3-14	Comparison of the masses of the observed sample of stars with other works as indicated.	49
4-1	Abundance profiles after core H-burning for several products of the CNO cycle in the stellar masses $1.4M_{\odot}$ (upper left), $2M_{\odot}$ (upper right), $3M_{\odot}$ (lower left) and $5M_{\odot}$ (lower right). The solid lines mark the deepest penetration in mass of the convective envelope, while the dashed lines mark the deepest penetration with overshooting. See text for details.	53

4-2	Calculated $^{16}\text{O}/^{17}\text{O}$ ratios after FDUP (solid line) and SDUP (dashed line) versus stellar mass. Calculation by Boothroyd & Sackmann (1999), Abia et al. (2012) and Karakas & Lattanzio (2014) are also shown. Observations are shown as data points.	57
4-3	$^{16}\text{O}/^{17}\text{O}$ ratio when overshooting below the convective envelope is applied in the three cases A, B and C where each corresponds to a different efficiency of overshooting as discussed in text.	58
4-4	Envelope overshooting used in this study cannot explain the low observed $^{12}\text{C}/^{13}\text{C}$ ratios in low mass stars. Note that the results shown from Tautvaišienė et al. (2010) are only for stars with solar-like and near solar composition. Calculations by other groups are also shown for comparison.	59
4-5	The nitrogen abundance calculated for the 21 giants. Abundances after FDUP without and with overshooting (red solid line and dashed blue line, respectively) and after SDUP without and with overshooting (black dotted and dot-dashed lines, respectively). The observational values are by Tsuji08 using two methods: standard abundance analysis (filled black circles) and the curve-of-growth (COG) method (blue astrisks) (see Tsuji08 for details).	60
4-6	The $^{16}\text{O}/^{17}\text{O}$ ratio calculated with 4 different sets of compilations of reaction rates. Left panel shows the case with standard mixing and the right panel is that with overshooting. Several observational data are also included.	62
4-7	The SA13 set of rates without overshooting (left panel) and with overshooting (right panel) (see text for details). We show the median rates (solid line), their upper limits (dot-dashed) and lower limits (dashed). Observational data are the same as those in Fig. 4.6.	63
4-8	$^{14}\text{N}/^{15}\text{N}$ ratio calculated after FDUP (black solid line) and SDUP (black dashed line). The values by El Eid (1994) after FDUP (red dotted line) and SDUP (blue dot-dashed line) are included for comparison.	64

5-1	A schematic (not to scale), showing the structure of a $3M_{\odot}$ star in the E-AGB phase in the standard calculation. The coordinates of important zones are given in mass (left) and radius (right) in solar units.	67
5-2	Evolutionary characteristics of a $3M_{\odot}$ star of solar-like initial composition. Left panel: Evolution in the HR diagram. Right panel: Time evolution of the stellar luminosity (thick line), helium luminosity (solid line) and hydrogen luminosity (dashed line) during the TP-AGB phase.	68
5-3	The detailed structure of a single pulse during the evolution of a $3M_{\odot}$ star. Shown are the helium shell luminosity (blue solid line), the hydrogen shell luminosity (black dashed line) and the total luminosity (red solid line). Note that the star's total luminosity remains essentially constant throughout the pulse.	69
5-4	The convective structure associated with the different phases of one pulse (Lattanzio & Wood 2003).	69
5-5	Present calculation showing the 14 th and 15 th thermal pulses of a $3M_{\odot}$ sequence and the associated PDCZs. Convective regions are shown in black and radiative regions in white. In order to show two pulses clearly on the same graph, the time scale between them is interrupted since the interpulse occurs at a much longer time scale compared to that of the pulse.	70
5-6	The 8 th pulse of a $3M_{\odot}$ sequence calculated when overshooting is applied at all convective boundaries (see text for details). The time has been reset at the onset of the previous pulse. The H-shell burns just below the convective envelope. TDUP operates at the end of the pulse, before the H-shell gets re-activated, and produces a ^{13}C pocket which is the neutron source for the <i>s</i> -process. The protons are mixed downward a depth of a few $10^{-4}M_{\odot}$, and the PDCZ is up to a few $10^{-2} M_{\odot}$ in mass.	72

5-7	The panels show the abundance profiles of the core-envelope transition zone, particularly, the region where the ^{13}C pocket is formed in a $3M_{\odot}$ sequence at different times following the 8 th thermal pulse as indicated. Time is set to zero at the onset of the pulse. Overshooting is applied at all convective boundaries (see text).	74
5-8	Spectra of stars in the Large Magellanic Cloud with some of the strongest molecular bands identified (Lattanzio & Wood 2003).	78
5-9	The s-process path through the Zr, Nb and Mo isotopes. Notice that there are two unstable Zr isotopes: long-lived ^{93}Zr and short-lived ^{95}Zr . Thick lines show the main path of the s-process, while the thinner lines show the less important branchings (Nicolussi et al. 1998).	80
6-1	Left panel: Evolutionary track in the HR diagram of the $9M_{\odot}$ sequence. Labeled phases are described in text. Right panel: Evolution of the convective structure during the H-, He- and C-burning phases. The thin dashed line marks the position of the H-burning shell. Labels are the same as those in left panel. t^* is the time left until the end of calculation in years, i.e. $t^*=t_f-t$	84
6-2	Mass fractions of the major isotopes and the temperature profile at the end of He-burning. The mass is in solar units (M_{\odot}).	85
6-3	The abundance profiles of major isotopes at different times after the ignition of carbon-burning as indicated. The value of the central density is also shown in each panel.	86
6-4	Evolution of the convective structure during the H-, He- and C-burning phases of the $9M_{\odot}$ sequence calculated with the CF88 rate. t^* is the time left until the end of calculation in years, i.e. $t^* = t_f - t$	89
6-5	Mass fractions of the major isotopes and the temperature profiles in the helium-exhausted core at different times during carbon burning with CF88 rate ($t=0$ marks the onset of carbon burning).	90

Chapter 1

Introduction

Stars are known to be the production site of all the chemical elements and their isotopes in the universe, except hydrogen, helium, deuterium and traces of lithium and beryllium, which were produced in the primordial nucleosynthesis. Due to the shape of the Initial Mass Function (IMF), stars in the mass range $(1-12)M_{\odot}$ are quite numerous. Moreover, their lifetimes span a large range of magnitudes, from 20 million to 10 billion years during which they experience diverse nucleosynthesis processes that produce chemical elements which eventually get ejected into the interstellar medium. This makes them major and substantial contributors to the chemical composition of our Milky Way galaxy and other galaxies.

The main focus of this thesis is to study the evolutionary phases of stars in the mass range $(1-12)M_{\odot}$, given their important contribution to the chemical inventory of the Galaxy. The initial mass and composition primarily determine the evolution of a star, and consequently its chemical signature. For solar-like initial composition stars, an overview of the general characteristics of their evolution as determined by the initial main-sequence mass is shown in Fig. 1-1. It is emphasized that the transition masses characterizing the mass ranges are not precisely fixed but are rather sensitive to model assumptions as shall be discussed later in Section 6.2.

As seen in Fig. 1-1, three mass ranges concerned with this work are distinguished:

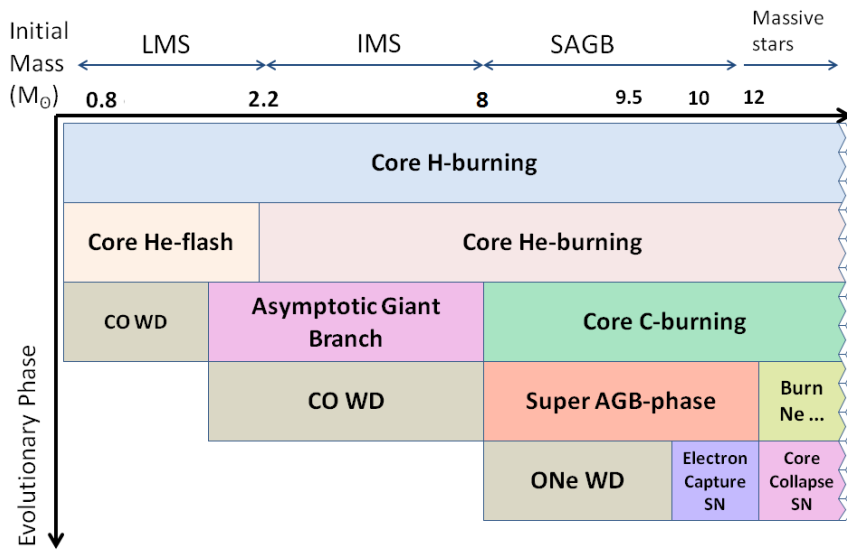


Figure 1-1: A schematic diagram showing the different burning phases and final stages experienced by solar metallicity stars according to their initial mass. Note that the transition masses are sensitive to model assumptions and subject to modification. A similar figure can be found in Karakas & Lattanzio (2014).

(a) low mass stars (LMS), in the mass range $0.8 \lesssim M/M_{\odot} \lesssim 2.2$, (b) intermediate mass stars (IMS) in the mass range $2.2 < M/M_{\odot} < 8$, and (c) stars of masses $\gtrsim 8M_{\odot}$, which are called Super Asymptotic Giant Branch (SAGB) stars, when they reach the AGB phase.

Introducing these mass ranges is rather preferential and convenient, based on the fact that each range is characterized by certain distinctive physical phenomena. The LMS evolve through the peculiar phase of the core He-flash due to unstable nuclear burning under electron degenerate conditions. IMS do not reach central temperatures required for carbon ignition, so they eventually form CO white dwarfs (CO WDs). However, SAGB stars are able to ignite central carbon, and may eventually form oxygen-neon (ONe WDs) (see Fig. 1-1). The evolution prior the early AGB phase is discussed in details in Chapter 3. The nucleosynthesis and abundance yields during this phase are presented in Chapter 4. The evolution and nucleosynthesis of the AGB phase are discussed in detail in Chapter 5. The evolution towards the SAGB phase of the more massive stars is discussed in Chapter 6. These stars may experience supernovae (SN) explosions and thus are important for the formation of heavy elements.

During the late phases of evolution, mass-loss by stellar wind becomes important especially in the more massive stars. Mass-loss is included in the calculations for the whole mass range. Details on the mass-loss treatment are provided in Chapter 2.

Stellar modeling using numerical simulation provides information on the structure of the whole star during its different phases of evolution. However, this simulation includes some free parameters, and thus, observations are needed to possibly constrain the parameters involved in the evolutionary models. Spectroscopic observations and circumstellar dust grains can be used as effective constraints on the theoretical models as well as on the nucleosynthesis yields.

In this work, we compare the model predictions with observations, regarding general stellar properties and surface compositions. This may help to improve the physical assumptions underlying the calculated stellar models. In particular, the effect of key nuclear reaction rates and the treatment of convective mixing will be of central interest.

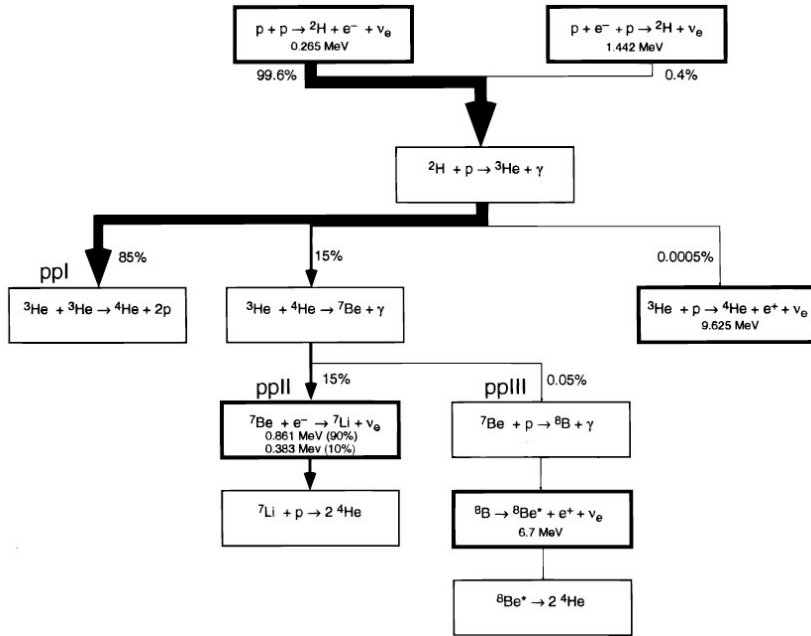


Figure 1-2: Reactions involved in the branchings of the proton-proton chain (Guenther & Demarque 1997).

1.1 Main Phases of Stellar Evolution

1.1.1 The Main-sequence

Stars of solar-like composition (Population I) are formed in giant molecular clouds having the composition 70% hydrogen, 28% helium and 2% all other elements. A complicated process of a collapse and fragmentation phase follows (not our aim to describe here) which leads to the formation of a protostar, observed for the first time in the HR-diagram as a “T-Tauri” star. When the star reaches the “zero-age main sequence”, it has achieved hydrostatic and thermal equilibrium as a consequence of core H-burning, during which hydrogen is transformed into helium. However, there are two burning modes of this fusion process: the proton-proton (pp) chain and the CNO cycle. The involved nuclear reactions are shown in Figs. 1-2 and 1-3 for the pp chain and CNO cycle, respectively.

Although both nuclear burning processes occur simultaneously during core H-burning,

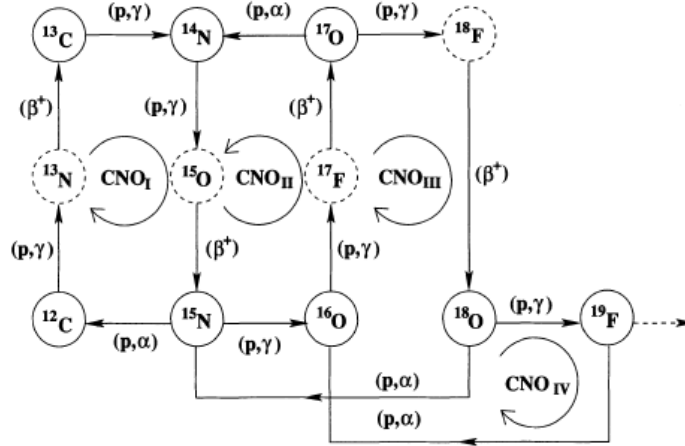


Figure 1-3: The CNO cycle(s). Unstable isotopes are represented by dashed circles, and the dashed line shows leakage out of the chains (Arnould et al. 1999).

the CNO cycle is not effective in population I stars unless the main-sequence mass is $\geq 1.5M_{\odot}$. The reason is that the nuclei involved in the CNO cycle have larger proton numbers than in case of the pp-chain, thus they have larger Coulomb barriers. Consequently, higher temperatures are required for the operation of the CNO cycle. Fig. 1-4 illustrates the “transition temperature” for the operation of this cycle, which is about $18 \times 10^6 \text{K}$.

Fig. 1-5 is a Hertzsprung-Russell (HR) diagram which shows several evolutionary phases. We select the $5M_{\odot}$ star, since it experiences almost all evolutionary phases under consideration. The core H-burning proceeds between the positions 1 to 3. After core H-burning, an overall contraction phase starts from position 3 to 4, during which the temperature increases everywhere, especially in the layers surrounding the hydrogen-exhausted inner region (He-core) where a hydrogen-abundance gradient exists. This causes hydrogen burning to proceed in a shell surrounding the He-core. This phase starts after position 4 in Fig. 1-5. The energy flux of this shell burning inflates the star’s outer layers which leads to a decrease in the surface temperature, so that the star evolves to the red giant branch (RGB) (pt. 5). It is well known that the opacity increases in

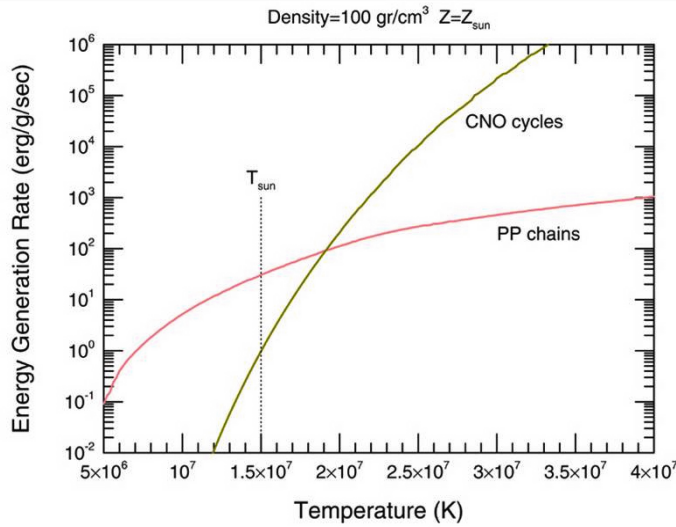


Figure 1-4: Energy generation rate by the CNO cycle and pp chain. The pp chain dominates in the lower temperature range and for stars of masses $\lesssim 1.5M_{\odot}$, while the CNO cycle is the dominant source for higher temperatures. The transition temperature is about $18 \times 10^6 \text{K}$. (Retrieved from <https://people.nslc.msu.edu>).

the outer layers during this expansion, so that the radiative temperature gradient, being directly related to the opacity, exceeds the adiabatic temperature gradient. Consequently, envelope convection sets in, which characterizes the RGB phase, marked by the positions 5 to 7 in Fig. 1-5.

1.1.2 The Red Giant Branch

On the RGB, the star is very luminous owing to the increased radius, despite the decreased effective temperature. This is a consequence of the Stephan-Boltzmann law relating the luminosity (L) to the radius (R) and the effective temperature (T_{eff}) by:

$$L = 4\pi R^2 \sigma T_{eff}^4 \quad (1.1)$$

This relation shows that the luminosity depends both on the radius and temperature of a star. In fact, despite the decreasing surface temperature of an expanding star, the

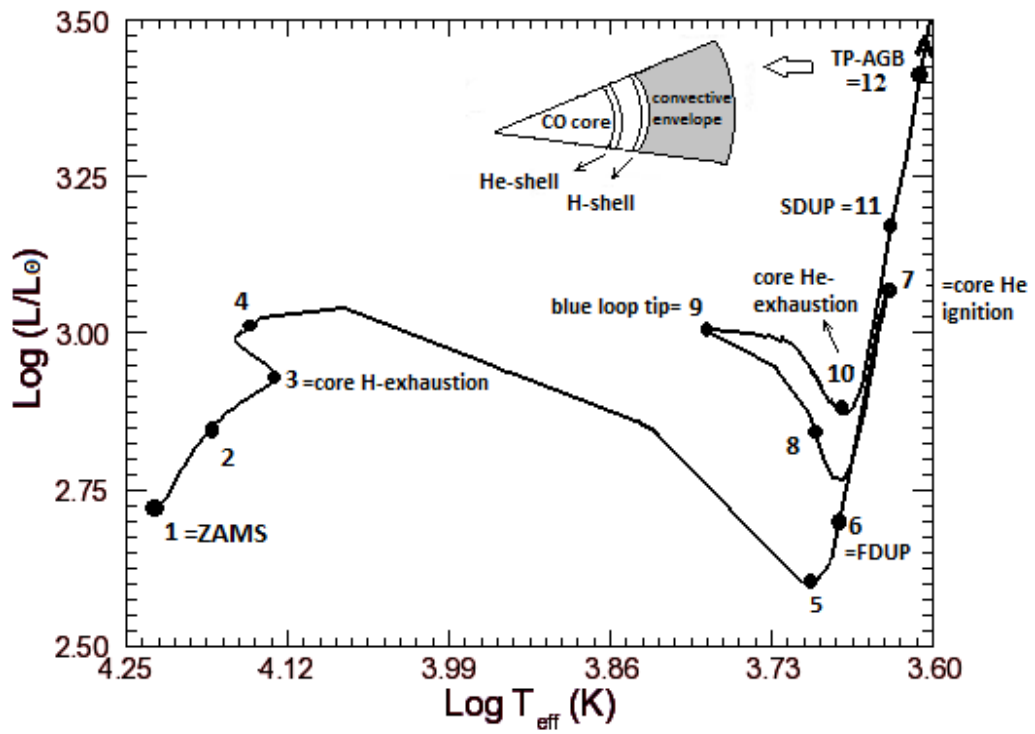


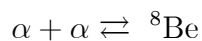
Figure 1-5: The evolution of a $5M_{\odot}$ star in the HR diagram, see text.

luminosity will increase because of the larger radius. This relation is used as a boundary condition to construct stellar models, assuming a blackbody surface (see Appendix 1).

The formation of the convective envelope is shown in Fig. 1-6a, which illustrates the evolution of the internal structure of the $5M_{\odot}$ star from its center to its surface. Position 6 marks the maximum extension of the convective envelope, or the “*First Dredge Up*” (FDUP). This is the first phase that alters the surface composition of the star since envelope convection mixes up the products of the H-burning to the surface, mainly ^4He , ^{12}C , ^{13}C , ^{14}N and ^{17}O . Analyzing these modified surface abundances is an important tool to get more insight into the internal structure of the star during this phase. This is discussed in details in Chapter 4.

As the star ascends the RGB, its core contracts until the central temperature is high enough to ignite helium at 10^8K (pt. 7 in Fig. 1-5). At this stage, the luminosity of the star is supplied by the central He-burning and the shell hydrogen burning from pt. 7 to 9 as seen in Figs. 1-5 and 1-6b. The helium burning process is remarkable in nuclear astrophysics and leads to the synthesis of ^{12}C in the universe, the fourth abundant element after ^1H , ^4He and ^{16}O . While the simultaneous interaction of three α particles to form ^{12}C is energetically possible, the probability for this process is too small to account for the observed ^{12}C abundance.

This problem was first solved by Salpeter (1952a,b) who proposed a two-step process. In the first step, two α -particles react to form ^8Be . But this is an unstable nucleus whose ground state has a width of 2.5eV. This corresponds to a lifetime of only 2.6×10^{-16} sec. Although short, this lifetime is much longer than the transit time of 10^{-19} sec of two α particles of kinetic energies corresponding to the Q-value. The result is that a small concentration of ^8Be nuclei is formed in equilibrium with the two α -particles:



Given the condition in red giant cores of $T = 10^8\text{K}$ and $\rho = 10^8\text{kg/m}^3$, and using the Saha equation (see Rolfs & Rodney 1988 for details), one obtains for the number

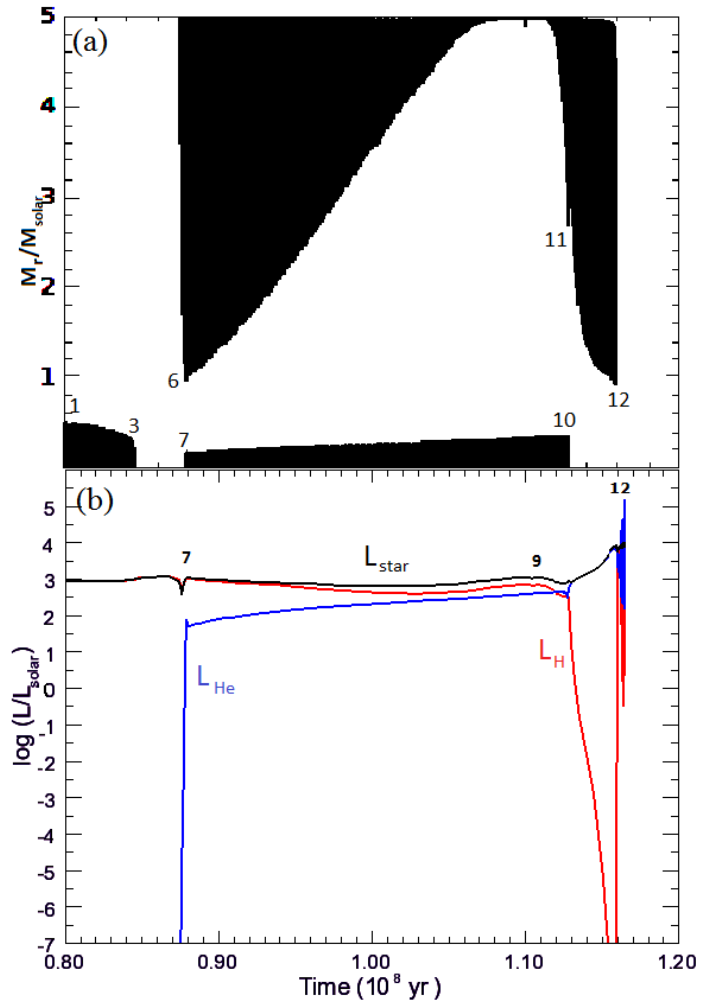
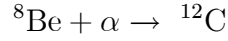


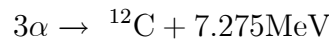
Figure 1-6: Upper panel: The evolution of the convective structure of a $5M_{\odot}$ star. Black regions are convective and white regions are radiative. Lower panel: the hydrogen luminosity (red), helium luminosity (blue) and the total star's luminosity (black). The numbers marked correspond to the same numbers in Fig. 1-5.

densities $N(^8\text{Be})/N(^4\text{He}) = 5.2 \times 10^{-10}$. This means that there's about one ^8Be nucleus for 10^9 He nuclei. In a second step, an additional α -particle is captured by ^8Be to form ^{12}C :



The net effect is that three α -particles are combined in this way to form ^{12}C , and this is called “triple-alpha process”. This carbon creation is unique in a sense, and it is a masterpiece of creation which enables the existence of the human being in our universe (El Eid 2005). What is more remarkable concerning this process is what has been firstly recognized by Hoyle et al. (1953), who showed that the observed ^{12}C abundance can only be obtained if the reaction $^8\text{Be}+\alpha$ takes place through an s-wave resonance at 7.654MeV in the ^{12}C nucleus. This resonance was not known, but has been found about four years later by Cook et al. (1957). This was an impressive prediction of the property of a nucleus based on astrophysical grounds.

A summary of carbon creation by the triple- α process is shown in Fig. 1-7 and its net effect is:



The role of this reaction in the evolution of stars is very remarkable as shall be seen later. The reason is its strong temperature and density dependence. The energy generation rate of the triple- α reaction near $T=10^8\text{K}$ is found to be (Rolfs & Rodney 1988):

$$\varepsilon(3\alpha) = 4 \times 10^{-8} \rho^2 X_\alpha^3 (T/10^8)^{41} \quad (\text{erg/g. sec})$$

where X_α is the mass fraction of the He-nuclei. The temperature dependence is striking and leads to the core He-flash in low mass stars ($M \leq 2.2M_\odot$) of solar-like initial metallicity, and to shell He-flashes (or thermal pulsations) on the AGB. This will be

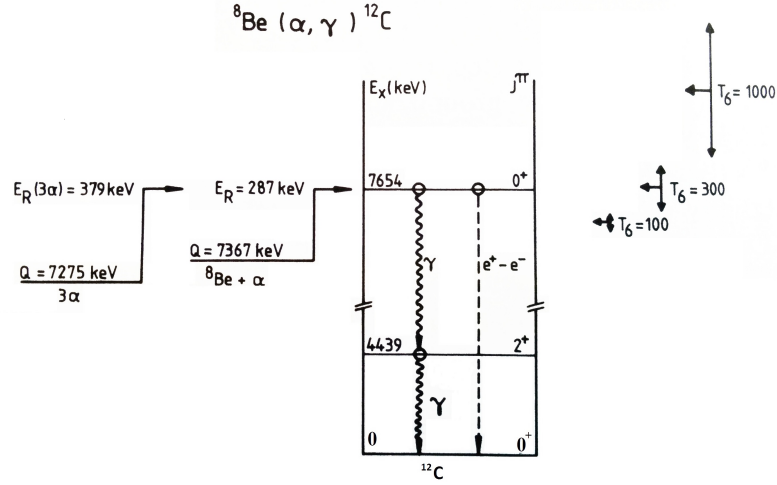


Figure 1-7: A schematic representation of the synthesis of ^{12}C (Rolfs & Rodney 1988).

described in Sections 3.1 and 5.1, respectively.

At the beginning of He-burning, the dominant reaction is the triple- α reaction until $X_c(\text{He}) \simeq 0.1$. Then as the temperature rises, ^4He becomes rather rare and with the increasing abundance of ^{12}C , the reaction $^{12}\text{C}(\alpha, \gamma)^{16}\text{O}$ gradually takes over. This reaction determines the final C/O ratio.

The evolution from point 8 to 10 in Fig. 1-5 is characterized by the formation of blue loops in the HR diagram during which the star burns He in its core and H in a surrounding shell. The tip of the blue loop is characterized by a maximum H-shell luminosity, marked by pt. 9 in Figs. 1-5 and 1-6b. Blue loops are discussed in details in Section 3.2. After the star evolves back to the RGB, it has completed core He-burning. It is now on the AGB phase (beyond pt. 10).

1.1.3 The Asymptotic Giant Branch

Position 10 in Fig. 1-5 marks the stage of core He-exhaustion, after which the core contracts again while shell H-burning leads to an expansion causing the envelope to

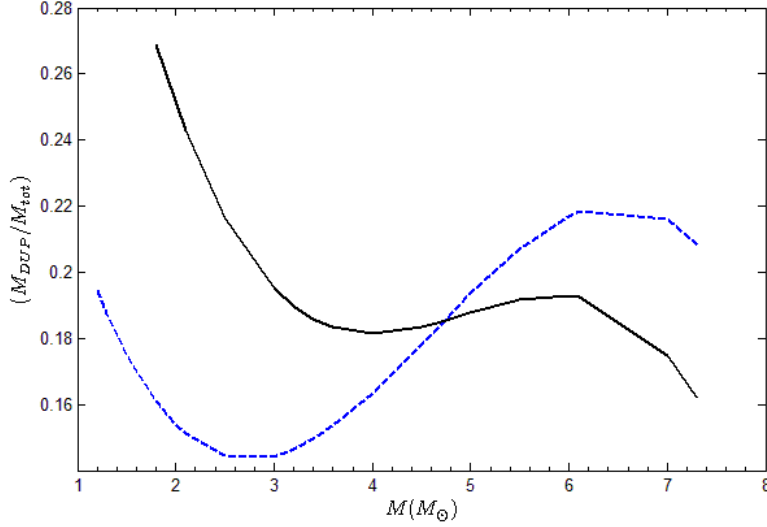


Figure 1-8: Fractional mass reached by the convective envelope at FDUP (dashed line) and SDUP (solid line). SDUP is deeper only in models of stellar masses $> 4M_{\odot}$. M_{DUP} is the mass shell reached by the dredge up.

become convective (pt. 11 in Fig. 1-6a). This phase is called “*Second Dredge Up*” (SDUP), which has an effect in stars of $M > 4M_{\odot}$, where the convective envelope mixes up to the surface the products of shell H-burning (${}^4\text{He}$, ${}^{12}\text{C}$, and ${}^{14}\text{N}$). The SDUP is rather sensitive to the efficiency of the H-burning shell, which acts as an entropy barrier in stars of $M \leq 4M_{\odot}$ preventing a deeper penetration of the convective envelope. However, for solar metallicity stars with $M > 4M_{\odot}$, the release of gravitational energy due to core contraction and the increased energy flux from the shell He-burning cause the outer layers to expand. This expansion drives the H-shell to low temperatures and it becomes temporarily extinct. This is shown in the drop in the hydrogen luminosity (L_{H}) beyond pt. 9 in Fig. 1-6b where L_{H} is the integrated energy generation rate. The expansion leads to the formation of a convective envelope, or SDUP. This convective episode smears out the composition discontinuity left over by the FDUP and therefore, it introduces further changes in the surface abundances of these stars.

Fig. 1-8 serves to compare the FDUP and SDUP where it shows the maximum

penetration of the convective envelope at first and second dredge up phases as a function of the initial stellar mass. We find that the deepest penetration of the FDUP occurs in stars of mass $\approx 2.5M_{\odot}$. The extension of the convective envelope is clearly very sensitive to the stellar mass and the phase of evolution. The efficacy of the H-shell burning is mainly determining how extended the convective envelope will be. The H-shell source leads to an expansion which is most pronounced in stars of masses near $2.5M_{\odot}$.

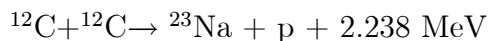
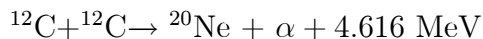
The fact that SDUP doesn't penetrate deeper than FDUP in masses less than 4 to $5M_{\odot}$ is of key importance, especially in low mass stars, because it implies that the observed surface abundances of these stars on the AGB phase are actually "inherited" from the RGB phase. We shall come back to this point later in Chapter 4.

The structure of the star on the AGB is characterized by a core essentially consisting of C and O, the main products of He-burning, surrounded by a He-burning shell and a H-burning shell (see insert in Fig. 1-5). This phase is divided into two parts: the early AGB (E-AGB) and the thermal pulsation phase (TP-AGB). The difference between the two phases can be explained by the behavior of the H-shell and He-shell burning in Fig. 1-6b. At the end of core He-burning, the star is on the E-AGB phase, where the main energy source in the star is the H-burning shell, which supplies the star's luminosity. Below the H-shell source, the stellar layers contract as the H-shell "rains down" fresh helium onto the He-shell. This raises the temperature in the He-rich layers and leads to He-ignition. Since the triple- α reaction is highly temperature sensitive, the enhanced burning of the He-shell causes a strong expansion in the form of a flash or pulse, called thermal pulse, causing the star to expand. It gradually pushes the H-shell outwards in mass (to lower temperatures) until the H-shell becomes less effective. When the He flash ends, the star contracts, and the H-shell gets re-ignited. The ensuing evolutionary phase is the TP-AGB, during which both burning shells control the thermal pulsations (point 12 in Figs. 1-5 and 1-6b). This phase and its importance are described in details in Chapter 5.

1.1.4 The Super Asymptotic Giant Branch

Stars that attain the central conditions for hydrostatic carbon burning evolve to the SAGB phase. This phase is similar to the AGB phase, but the thermal pulsations and mass-loss lead to the formation of an oxygen-neon white dwarf (ONe WD). SAGB stars may also develop massive degenerate cores that undergo electron-capture reactions and subsequent explosion. This is called electron-capture supernova (EC-SNe).

Since the carbon burning rate plays an important role in this context, we summarize its main features here and describe more details in Section 2.2.2. The $^{12}\text{C}+^{12}\text{C}$ fusion reaction has two main channels responsible for the energy production by carbon fusion:



In addition, ^{23}Na is transformed to ^{24}Mg via $^{23}\text{Na} + \text{p} \rightarrow ^{24}\text{Mg}+\gamma$

Thus, the most abundant species left over from core C-burning are ^{20}Ne , ^{23}Na , and ^{24}Mg in addition to ^{16}O formed previously during He-burning. The details of evolution during the SAGB phase are discussed in Chapter 6.

1.1.5 Observational evidence of the different evolutionary phases

When Hertzsprung-Russell diagrams of globular clusters were first obtained in the 1950s, the asymptotic merging of the AGB and the RGB was regarded as a branching, and the direction of evolution was unknown. After Schwarzschild and Härm (1965) evolved a low mass star past the Horizontal Branch and *up* the AGB, Sandage and Walker (1966) were probably the first to use the term “asymptotic” (according to Lattanzio & Wood (2003)). Fig. 1-9 shows the HR diagram of the globular cluster M3. Several phases which we have described are shown. Note that the main sequence phase is a densely populated region in the HR diagram since stars spend almost 90% of their lifetime in this phase. The diagram also shows RGB and AGB stars. Such a diagram is a clear evidence of stellar evolution over a very long time scale. In case of M3, the “turn-off” mass indicates an age in excess of 10^{10} years.

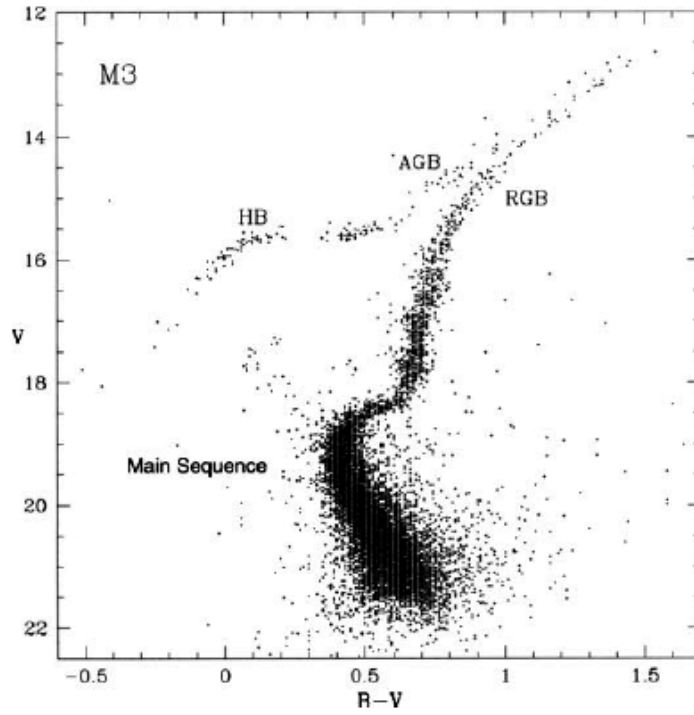


Figure 1-9: The HR-diagram of the globular cluster M3 showing the visible magnitude versus the color index $B-V$. The positions of the main-sequence, the red giant branch (RGB), the horizontal branch (HB), and the asymptotic giant branch (AGB) are indicated (Lattanzio & Wood 2004).

Chapter 2

Method of Calculation

2.1 Stellar Evolution Code

The evolution of stars in the considered mass range is carried out using our hydrodynamic computational program (or code) “HYADES”, which is based on a one-dimensional implicit Lagrangian scheme. Details on the physics of this code can be found in my Master’s thesis (G. Mahmoud 2009) and details on the numerical method can be found in Shaya (1999). Discretized stellar structure equations (Kippenhahn and Weigert (1990) or see Appendix 1) are solved using Newton–Raphson iteration in five dimensions, on an adaptive grid. The equation of state incorporated in the code can handle different degrees of electron-degeneracy and includes coulomb corrections. Suitable central and surface boundary conditions are used to construct the stellar models, which are evolved through the different burning phases. The OPAL opacities are used (Iglesias & Rogers 1996) and for temperatures below about 6000K we use the Rosseland mean opacities calculated by Alexander & Ferguson (1994), which include the effects of molecules on the opacities. A basic description of this code is given by El Eid et al. (2009) and references therein, and more recent calculations with this code are presented in Halabi et al. (2012).

In the context of this thesis, several improvements have been introduced into the code which are discussed in the next sections. These are as follows:

- (a) Treatment of mass-loss by stellar wind
- (b) Treatment of convective mixing
- (c) Updated thermonuclear reaction rates and extending the network of nuclear reactions including neutron-capture reactions in order to study the production of heavy elements in AGB stars.

2.1.1 Treatment of mass-loss

Mass-loss by stellar wind has an important effect on the evolution of stars, and thus, requires a suitable treatment. Mass-loss rates are included in the present calculation using semi-empirical mass-loss rates adjusted to the global parameters of the stars. In particular, we adopt the mass-loss rates according to a Mira pulsation period (P) suggested by Vassiliadis & Wood (1992):

$$\log(P/\text{days}) = -2.07 - 0.9 \times \log\left(\frac{M_{ZAMS}}{M_{\odot}}\right) + 1.94 \times \log\left(\frac{R}{R_{\odot}}\right) \quad (2.1)$$

For $P < 300$ days, we use the mass-loss rate suggested by Reimers (1975), given by

$$\dot{M}_R = \eta \times 4 \times 10^{-13} \times \frac{LR}{M} \quad (2.2)$$

where L , R and M are the luminosity, radius and mass, respectively, in solar units, and η is a free parameter. We take $\eta = 1$ for stars of mass below $4M_{\odot}$ which means effective mass-loss, and $\eta = 0.5$ for masses $4M_{\odot}$ and above. For stellar masses $7M_{\odot}$ and above, we use Reimers' formula throughout the whole evolution (we elaborate on the details of this choice in Section 6.4).

In stars of $M < 7M_{\odot}$, for $300 \leq P < 500$ days a more effective rate is used according to Bowen (1988):

$$\dot{M}_B = \dot{M}_R \times 4.83 \times 10^{-9} \left(\frac{M_{ZAMS}}{M_{\odot}}\right)^{-2.1} \left(\frac{L}{L_{\odot}}\right)^{2.7} \quad (2.3)$$

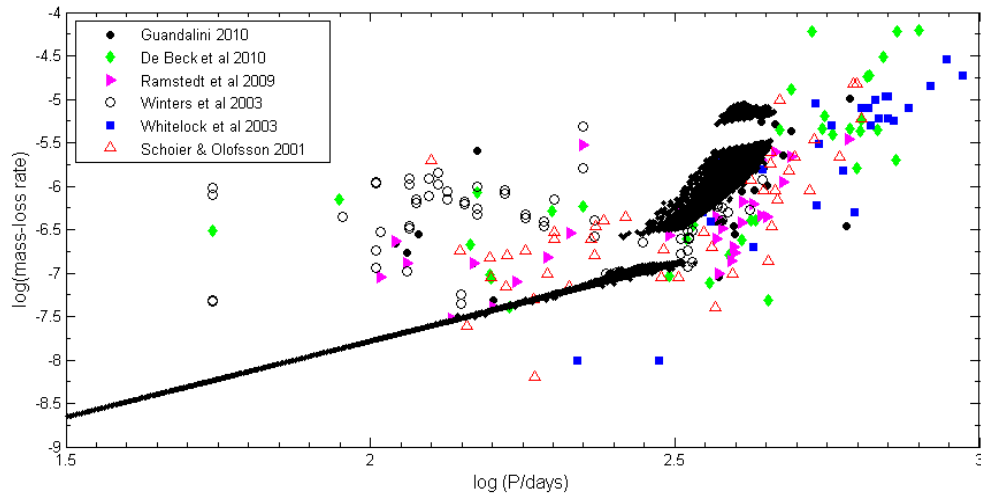


Figure 2-1: The mass-loss rates in a $3M_{\odot}$ sequence vs. the Mira pulsational period as compared to the observed mass-loss rates labeled in the upper left panel. The mass-loss rate predicted by our calculation is consistent with the two mass-loss regimes experienced by these giants. See text for more details.

For $P \geq 500$ days, superwind mass-loss rate during the AGB is used according to the formula suggested by Vassiliadis & Wood (1992)

$$\dot{M}_V = \frac{L}{3 \times 10^8 \times v_{\text{exp}}} \frac{3.15576}{M_{\odot}} \quad (2.4)$$

where v_{exp} is the stellar wind expansion velocity given by $v_{\text{exp}} = -13.5 + 0.056 \times P$.

In order to test the treatment of the mass-loss rate, we show in Fig. 2-1 these rates as a function of the Mira pulsation period for the $3M_{\odot}$ star, together with the observed mass-loss rates obtained from several works. Despite the scatter in the data, two regions can be clearly identified, a region of moderate mass-loss rate up to $\log P = 2.5$, and a more effective mass-loss rate for $\log P > 2.5$. The mass-loss rates used are indicated with black dots, and appear to be reasonably consistent with observations in the two mass-loss regimes.

2.1.2 Convective mixing

Convective mixing of the nuclear species is treated by solving the diffusion equation (El Eid 1995):

$$\frac{dX_i}{dt} = \frac{\partial}{\partial M_r} \left[(4\pi r^2 \rho)^2 D \frac{\partial X_i}{\partial M_r} \right] \quad (2.5)$$

This equation applies in convective regions, provided that the appropriate diffusion coefficient is known. If a region is convective according to the Schwarzschild criterion, that is $\nabla_{rad} > \nabla_{ad}$ (the radiative temperature gradient is larger than the adiabatic one, see Appendix 1), the diffusion coefficient in the equation is given by (Langer et al. 1985):

$$D_c = \frac{1}{3} \alpha^{\frac{2}{3}} H_p \left[\frac{c}{\kappa \rho} g \beta (1 - \beta) \nabla_{ad} (\nabla_{rad} - \nabla_{ad}) \right]^{\frac{1}{3}} \quad (2.6)$$

where α is the mixing length parameter, H_p is the pressure scale height, κ is the opacity c is the velocity of light in vacuum, ρ is the density, g is the gravitational acceleration, β is the gas pressure fraction.

If the extension of a convective zone is determined by the Schwarzschild criterion, a complication arises at the boundary because of the abrupt transition between the convective and radiative regions. This is a crucial and long-standing problem in stellar modeling. The 2D hydrodynamical simulations by Freytag (1996) suggest that the convective boundary can be extended by using eq. 2.5 but with a modified diffusion coefficient derived for 1D calculations and is given by:

$$D_{os}(z) = D_c e^{\frac{-2z}{fH_p}} \quad (2.7)$$

where D_c is the diffusion coefficient at the convective boundary given by eq. 2.6 and $z = |r_{\text{boundary}} - r|$ is the width of the extended region beyond the Schwarzschild boundary. This is calculated using the parameter f , chosen to be 0.25 as suggested by Freytag (1996). With this description, $D_{os}(z)$ is exponentially decreasing as a function of the

geometric distance z in the “overshoot” region. This treatment of extra-mixing, called “overshooting”, is one way of mixing the chemical elements beyond the boundary as determined by the Schwarzschild criterion. This diffusion model is not a unique way, but is more physical than the instantaneous mixing in the overshoot region. This description will be used, and its effect on the internal structure of stars and the nucleosynthesis yields will be explored.

2.2 Nuclear reaction network

A nuclear reactions network is a set of differential equations that describe the rate of change of abundances with time due to diverse nucleosynthesis processes. Knowing the reaction rates at astrophysical conditions allows the calculation of abundances upon integration over a certain time scale. In case of hydrogen burning for example, the abundances change with time according to reactions shown in Fig. 1-2 for the pp chain and in Fig. 1-3 for the CNO cycle. Such reactions are also important for calculating the energy generation rates in stars.

For the sake of illustration, we consider the change of the deuterium nucleus in the pp-chain. The deuterium is produced by $p+p \rightarrow D + e^+ + \nu$. Its destruction is mainly determined by the reaction $D(p, \gamma)^3\text{He}$ (see Rolfs & Rodney 1988). Then, the time dependence of D is given by:

$$\frac{dD}{dt} = r_{pp} - r_{pD} \quad (2.8)$$

In general, $r_{12} = \frac{N_1 N_2}{1 + \delta_{12}} \langle \sigma v \rangle_{12}$ is the reaction rate per particle pair.

In the above equation, N is a number density and $\langle \sigma v \rangle$ is a Maxwellian averaged reaction rate per particle. The quantity δ_{12} is the Kronecker delta introduced to avoid double counting in case of identical particles. Then, the above equation becomes:

$$\frac{dD}{dt} = \frac{N_H^2}{2} \langle \sigma v \rangle_{pp} - N_H N_D \langle \sigma v \rangle_{pD} \quad (2.9)$$

This is a self-regulating equation that can reach a state of quasi-equilibrium $\frac{dD}{dt} = 0$. Then $(N_D/N_H)_e = \langle \sigma v \rangle_{pp} / 2 \langle \sigma v \rangle_{pD}$. With $T=5 \times 10^6 \text{K}$, one gets $(N_D/N_H)_e = 5.6 \times 10^{-18}$. This is very small indeed, but it reflects the fact that the p+p reaction involves the weak force and the electromagnetic force through $D(p,\gamma)^3\text{He}$. In other words, $(N_D/N_H)_e$ is of the same order as the ratio of the strength of these forces. Moreover, this small N_D/N_H ratio indicates that any amount of deuterium that might be present when a star forms will be quickly depleted during hydrogen burning (Iliadis 2007).

This example shows how fundamental nuclear astrophysics is. Without the p+p reaction no elements heavier than helium would exist except in the extreme cases of zero metal stars, where a very small amount of carbon is created by helium burning to establish hot CNO burning.

A general equation that determines the time rate of change of the abundance of individual nuclear species according to the reaction rate is given by eqn. A1.9 in Appendix 1.

2.2.1 Reactions of the CNO cycle

There has been extensive experimental work recently on updated determinations of major reaction rates, including those of the CNO cycle, after the NACRE compilation (Angulo et al. 1999). Significant improvements were introduced and the evaluation of these rates included updated nuclear physics input. We use several recent determinations of these rates. One considered set (Sergi et al. 2014) is obtained using the Trojan Horse method (La Cognata et al. 2010), which is an indirect technique that is able to provide more reliable reaction rate cross-sections at low temperatures where measurements in the astrophysical energy range are available. Other sets we use, obtained by Sallaska et al. (2013) and Iliadis et al. (2010), are evaluated based on Monte Carlo techniques (Longland et al. 2010; Longland 2012; Iliadis et al. 2014). This method provides a median rate which under certain conditions resembles the commonly referred to “recommended” rate, as well as a low rate and a high rate which, unlike the “upper” and “lower” limits of

classical rates, have well-defined statistical meaning. The effect of these determinations on the surface abundances of major elements and isotopes is investigated in Chapter 4.

One particularly important reaction is proton capture on ^{14}N ; represented as $^{14}\text{N}(p, \gamma)^{15}\text{O}$. This reaction controls the efficiency of H-burning by the CNO cycle. Three different determinations of this rate are used: the compilation by the NACRE collaboration (Angulo et al. 1999), the LUNA rate (Imbriani et al. 2005), and the new determination by Adelberger et al. (2011) which was re-evaluated by Halabi et al. (2012). We found interesting effects of this rate on the evolution of IMS, particularly during the blue loop phase, which are discussed in Chapter 3, as well as on the nitrogen surface abundances in red giants discussed in Chapter 4.

2.2.2 Carbon-burning reaction rate

Despite considerable experimental efforts in the past decades, the total $^{12}\text{C}+^{12}\text{C}$ fusion reaction rate remains uncertain by several orders of magnitude at stellar temperatures. Current data do not only show discrepancies in the derived astrophysical S-factor, but also in the possibility of having resonant structures, which makes the extrapolations to low energies extremely uncertain (Pignatari et al. 2013). Moreover, the relative strength between the two main channels (α -channel and p-channel) is poorly determined and still not well established experimentally (Pignatari et al. 2013 and references therein).

In this work four $^{12}\text{C}+^{12}\text{C}$ rates are used: CF88 rate (Caughlan & Fowler 1988), the rate recommended by Pignatari et al. (2013), as well as its upper and lower limits. Figs. 2-2 and 2-3 show how these rates compare in the relevant temperature range.

The recommended rate (CR) is based on the classical extrapolation of the averaged S-factor data using a standard potential model (Gasques et al. 2005) plus the contribution of a single resonance observed at $E_{cm} = 2.13$ MeV (Spillane et al. 2007), and is similar to the standard CF88 rate. The lower limit (CL) of the rate is suggested based on the incompressibility of nuclear matter in heavy ion fusion systematics by including a hindrance term for low-energy fusion processes (Gasques et al. 2007). The upper limit

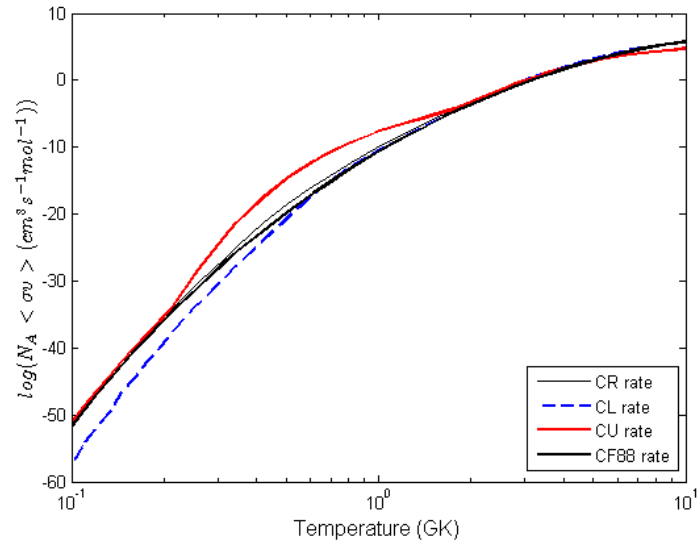


Figure 2-2: The $^{12}\text{C}+^{12}\text{C}$ reaction rates used in this work.

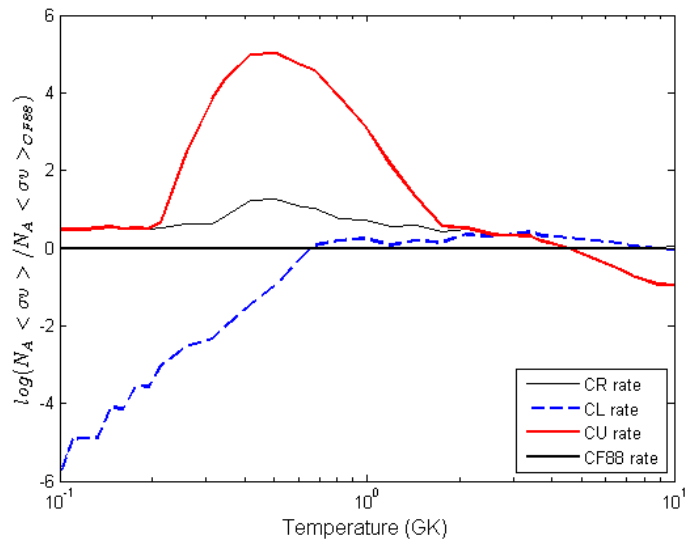


Figure 2-3: The rates in Fig. 2-2 are shown normalized to the CF88 rate.

of the rate (CU) includes an additional term resulting from a possible strong $^{12}\text{C}+^{12}\text{C}$ cluster resonance at $E_{cm} = 1.5$ MeV.

We study the effect of this rate on the critical transition mass (M_{up}), which is the minimum initial stellar mass that attains the conditions for hydrostatic carbon burning, as well as on the composition profiles of the ONe cores. Details are provided in Chapter 6.

2.2.3 The s-process

About half of the elements heavier than iron are produced by the slow neutron capture process (*s*-process) (Gallino et al. 1988; Busso et al. 1993; Straniero et al. 2006; Thé et al. 2007; Lugaro et al. 2014). In this process, nuclei heavier than iron are formed by neutron captures on ^{56}Fe (and heavier) nuclei; therefore, seed nuclei and free neutrons are required.

There are two possible neutron sources for the *s*-process: ^{13}C and ^{22}Ne . In the case of intermediate mass AGB stars, both sources are present but the first neutron source is dominant. The physical conditions of the formation of the neutron sources and their roles are discussed in Chapter 5. Here, the nuclear aspect of the *s*-process is described.

The basic physical principle underlying the *s*-process nucleosynthesis is illustrated in Fig. 2-4. An (n,γ) reaction transforms a $(Z,N-1)$ nucleus to another with (Z,N) . If the resulting nucleus is stable, another neutron capture takes place, but if it is radioactive it undergoes a β^- -decay. Obviously, there is a competition between the lifetimes of neutron capture and β -decay. The characteristic of the *s*-process is $\tau_{n\gamma} \gg \tau_{\beta}$, where τ_{β} is the β -decay lifetime and $\tau_{n\gamma}$ is that of neutron capture. Thus, the neutron-capture is slow compared to β -decay and the *s*-process follows closely the valley of β -stability. This is illustrated in Fig. 2-5. Using this figure, and starting for example at ^{127}I , neutron capture leads to ^{128}I , which is unstable with a lifetime of 2.5 min, thus decays to ^{128}Xe . Following this chain, one sees for example how Barium (Ba) isotopes are produced.

There is a simple way to estimate the required neutron density for the *s*-process,

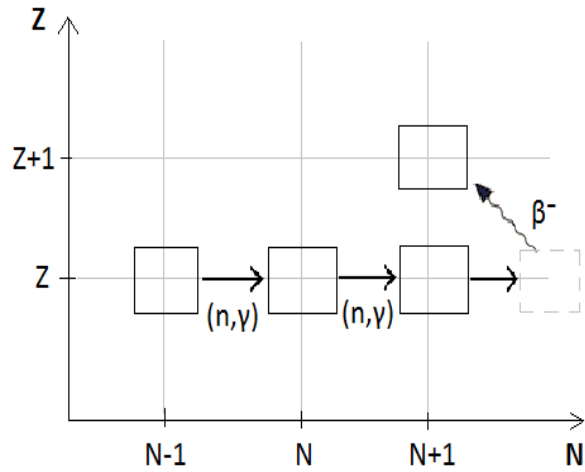


Figure 2-4: Simple chain along the s-process path in the Z-N diagram.

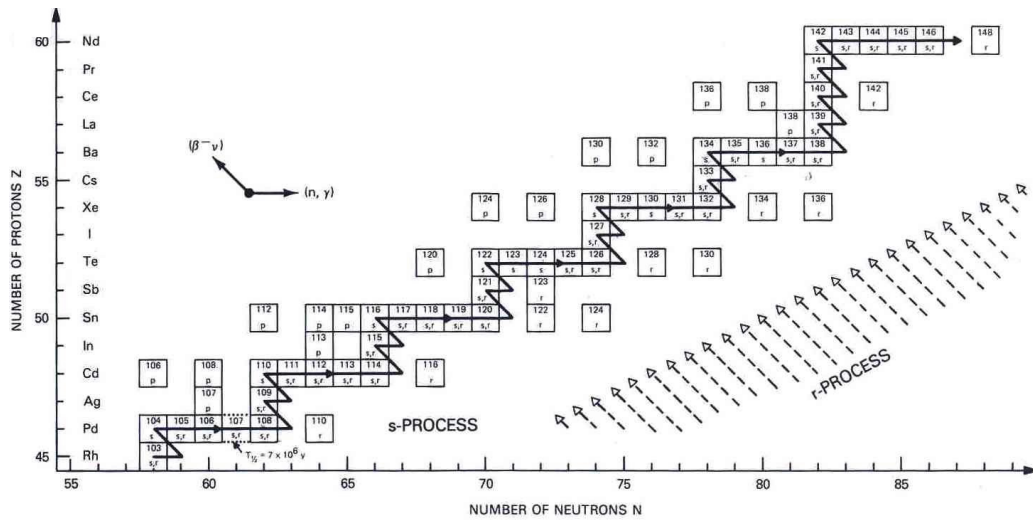


Figure 2-5: The s-process path (solid line) in a Z-N diagram. The s-process follows closely the valley of β -stability, bypassing the r- and p-process nuclei (Rolfs & Rodney 1988).

which yields $N_n = 10^8 \text{neutron/cm}^3$ (Rolfs & Rodney 1988). The condition $\tau_{n\gamma} \gg \tau_\beta$ is compatible with a neutron density of this order, which is achieved in AGB stars during the thermal pulsation as outlined previously. Following the nuclear transmutation along the s-process path illustrated in Fig. 2-4, a set of differential equations can be written that allows to determine the time rate of change of the s-process abundances. The time-dependence of abundance N_A of a stable isobar is written as:

$$\frac{dN_A(t)}{dt} = N_n(t)N_{A-1}(t) \langle \sigma v \rangle_{A-1} - N_n(t)N_A(t) \langle \sigma v \rangle_A - \lambda_\beta(t)N_A(t) \quad (2.10)$$

In this equation, N_n is the neutron number density, $\lambda_\beta = \ln 2/T_{1/2}(t)$ is the β -decay rate at time t if the isotope is radioactive. Clearly, this rate should be obtained according to the physical conditions in the stellar plasma. The quantity $\langle \sigma v \rangle$ is the Maxwellian averaged cross section. The first term in the above equation is the production of the isotope A by neutron capture, the second is its destruction by neutron capture, and the last term is its destruction by β -decay if this occurs.

Note that labeling the abundances only by A is sufficient because A is constant in β -decay, otherwise Z is uniquely defined. The above equation represents a set of coupled differential equations, and can only be solved numerically. A complete network of nuclear reactions, including the s-process, is available (Meyer (2012), <http://sourceforge.net/projects/nucnet-tools>).

The condition $\tau_{n\gamma} \gg \tau_\beta$ applies for the s-process, however, if $\tau_{n\gamma} \approx \tau_\beta$, this leads to the branching along the s-process path. This branching is also interesting and discussed in Chapter 5.

Assuming that the stellar temperature slowly changes during the s-process, one can introduce the neutron flux $\Phi(t)$ as:

$$\Phi(t) = v_T N_n(t) \text{ [neutrons/cm}^3 \cdot \text{s]} \quad (2.11)$$

Where v_T is the thermal velocity. The time-integrated flux τ can then be obtained:

$$\tau = \int_0^t \Phi(t)dt = \int_0^t v_T N_n(t)dt \quad [\text{neutrons/cm}^2] \quad (2.12)$$

Physically, τ measures the total neutron irradiation per unit area. In terms of τ , the rate equation becomes:

$$\frac{dN_A}{dt} = \sigma_{A-1}N_{A-1} - \sigma_A N_A$$

This equation has the tendency to be self-regulating. This means minimizing the difference to reach the steady state equilibrium, or $dN_A/dt = 0$. In other words one obtains:

$$\sigma_A N_A = \sigma_{A-1} N_{A-1} \quad (2.13)$$

or

$$\sigma_A N_A = \text{constant}. \quad (2.14)$$

This is called local equilibrium approximation. Its physical meaning is that the abundance of an element formed by the s-process only builds up until the rate of production is equal to the rate of destruction, i.e. local equilibrium is achieved. $\sigma_A N_A = \text{constant}$ means that a nucleus with a small neutron-capture cross-section in the s-process path must have a large abundance to maintain continuity, and a nucleus with large σ will have a small abundance.

The constancy of $\sigma_A N_A$ manifests itself in the behavior of the Tellurium isotopes ^{122}Te , ^{123}Te , ^{124}Te . These are s-only isotopes, i.e. only produced by the s-process, and are shielded from the contribution of the rapid neutron-capture process (which is a process in which the neutron densities are higher, $n_n \gtrsim 10^{20}\text{cm}^{-3}$, and the neutron capture is rapid compared to β -decay). The ratios of $\sigma_A N_A$ are found to be: $\sigma_N(122) : \sigma_N(123) : \sigma_N(124) = 1.0, 0.99, 0.97$ (Käppeler et al. 1982). Such results are displayed

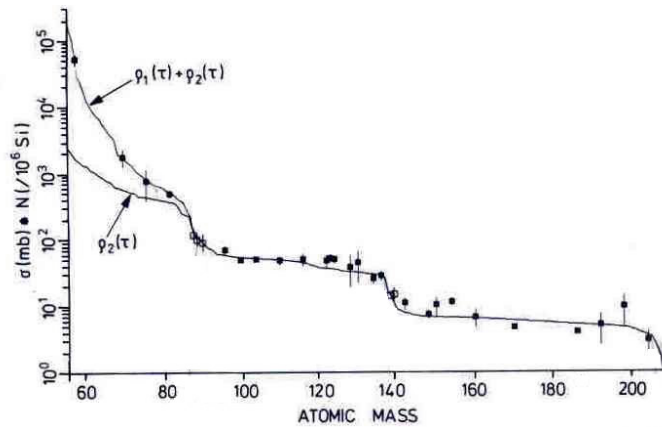


Figure 2-6: The product of the neutron-capture cross section and the solar system abundances, relative to $\text{Si}=10^6$ (σN), as a function of the atomic mass of s-only nuclei. The solid lines represent theoretical calculations for a single exponential distribution of neutron exposure, and for the sum of two such distributions (Rolfs & Rodney 1988).

in Fig. 2-6, which shows plateaus in atomic mass regions between closed neutron shells (magic numbers), $A=90-140$ and $A=140-206$. This is a nice confirmation of the local equilibrium approximation.

In Fig. 2-6, the breaks correspond to $A=84$, 138 and 208, which correspond to the s-process abundance peaks shown in Fig. 2-7. These are found to occur at the magic neutron numbers $N=50$, 82 and 126 where the neutron-capture cross section is very small. Another insight gained from Fig. 2-6 is that σN is not constant over the entire mass region from ^{56}Fe to ^{209}Bi , but is only piecewise flat, and there is an anomalous behavior below $A=80$. This indicates that the equilibrium is not achieved over the entire path of the s-process. This can be understood by investigating the dependence of σN on the neutron exposure τ . To create a significant number of nuclei on the high-mass side of the magic neutron numbers, a large neutron exposure is required. The work by Clayton et al. (1961) showed that a single exposure τ cannot produce the solar distribution, but multiple neutron exposures are needed to overcome the bottlenecks at the magic numbers in Fig. 2-6.

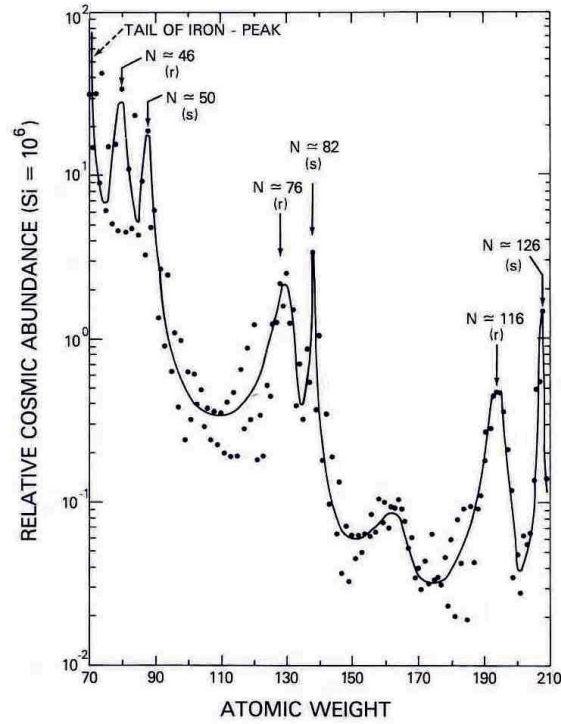


Figure 2-7: Cosmic abundances of the heavy elements as a function of the atomic weight. Nuclei with closed neutron shells ($N=50$, 82 and 126) show narrow abundance peaks. Broader peaks correspond to nuclei 4-10 mass units below the closed neutron shells (Rolfs & Rodney 1988).

As shown by Seeger et al. (1965), an exponential distribution function is suitable. If $\rho(\tau)d\tau$ is the number of iron nuclei that have experienced neutron exposure between τ and $\tau + d\tau$, then:

$$\rho(\tau) = \frac{f(N_{56})_{\odot}}{\tau_o} e^{-\frac{\tau}{\tau_o}} \quad (2.15)$$

where $(N_{56})_{\odot}$ is the total number of initial seed nuclei in the Sun (8.25×10^5 per 10^6 Si), τ_o is a mean exposure considered as a parameter. Note that this is a mathematical description and not a physical requirement. Given that multiple neutron exposures are required, it is interesting to realize that the recurrent thermal pulsations of the AGB stars indeed satisfy this requirement. Based on the analysis to understand the σN curve, it was soon recognized that the s-process has three components:

(a) Weak component that produces most of the s-isotopes with $A < 90$, i.e. from Fe to Sr. This can be described by $\tau_o = 0.06 \text{ mbarn}^{-1}$.

(b) Main component responsible for the formation of the s-isotopes with $90 < A \leq 204$. This can be described by $\tau_o = 0.3 \text{ mbarn}^{-1}$.

(c) Strong component needed to produce the solar system abundance of ^{208}Pb . This can be described by $\tau_o = 7.0 \text{ mbarn}^{-1}$.

All three components are needed to explain the solar system distribution. The site of the weak component is the massive stars of $M \geq 15M_{\odot}$ operating during core He-burning and there is a contribution from shell carbon-burning (see Thé et al. 2007 for details). The main component is associated with thermal pulsations in AGB stars (Herwig 2005). The strong component seems to be essential in low-metallicity AGB stars to produce ^{208}Pb .

Chapter 3

Evolution Prior the Early-AGB phase

The evolutionary tracks of stellar models in the mass range $(1.2-7.3)M_{\odot}$, calculated from the zero-age main sequence up to the Early-AGB (E-AGB) phase are shown in Fig. 3-1. Stars of $M \leq 2.2M_{\odot}$ and solar-like initial composition evolve through the core He-flash, as mentioned in Section 1.1. Those of masses $\gtrsim 3M_{\odot}$ exhibit blue loops initiated at the onset of central helium burning. A detailed discussion on the two evolutionary phases the core He-flash and the blue loop phase is presented in the following sections.

3.1 LMS: The Core Helium-flash

After the end of core hydrogen burning, red giant stars of $M \leq 2.2M_{\odot}$ of solar initial composition, experience the core helium flash (see Kippenhahn & Weigert (1990) for a basic description). This is an interesting evolutionary phase in low mass stars whose underlying physical conditions include a combination of a degenerate core and a strongly temperature dependent reaction rate. However, observations show that it is not a disruptive event, since stars survive this flash and burn He in a quiescent manner afterwards. In what follows, a brief description of this flash is given.

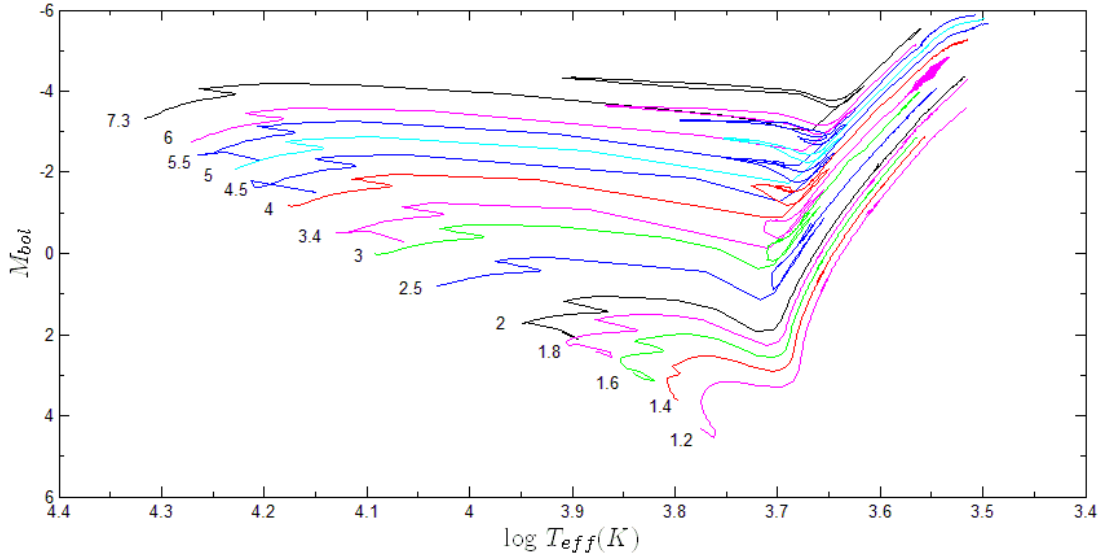


Figure 3-1: Selected evolutionary tracks of sequences in the mass range $1.2 - 7.3M_{\odot}$ (as indicated), calculated from the main sequence to the Early-AGB phase.

The He flash occurs because the strongly temperature-dependent triple- α reaction operates in a strongly electron-degenerate environment (Mocák et al. 2010; Bildsten et al. 2012; Kawaler 2012). Since the pressure is not sensitive to temperature in a degenerate gas, a thermal runaway occurs. As shown in Fig. 3-2, the central density does not vary significantly during the relatively short phase of the helium flash. However, the central temperature increase is remarkable and is required to lift the degeneracy so that the He-burning can then proceed under hydrostatic conditions.

The evolution depicted in Fig. 3-2 illustrates our computational simulation which is consistent with the analytical consideration (Kippenhahn & Weigert 1990). In particular, we find that for stars of $M < 2M_{\odot}$, the helium flash starts off-center owing to the neutrino cooling via the plasma and photo neutrinos when the central density increases beyond the region characterized by the degeneracy parameter $\eta = 5$ (see Fig. 3-2). For stars of mass $2 < M/M_{\odot} \leq 2.2$ the helium flash starts at the center since they evolve at relatively lower central densities.

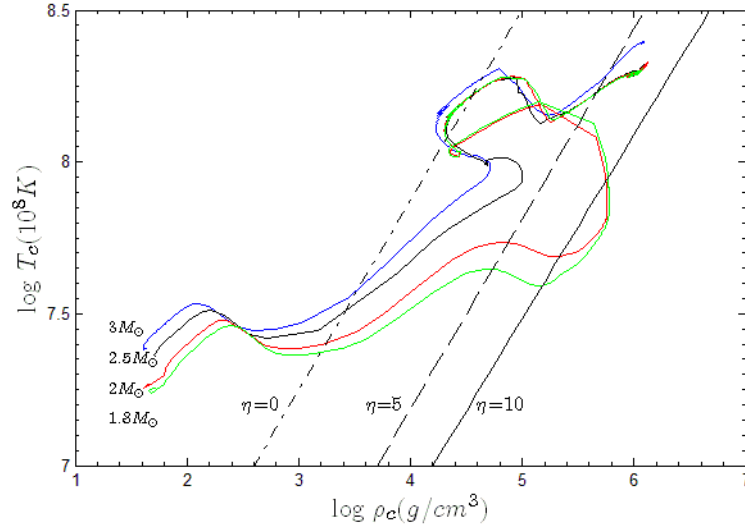


Figure 3-2: Evolutionary sequences in the $T_c - \rho_c$ plane for selected stellar masses as indicated. The lines marked by the degeneracy parameter η indicate the regions of increasing degeneracy.

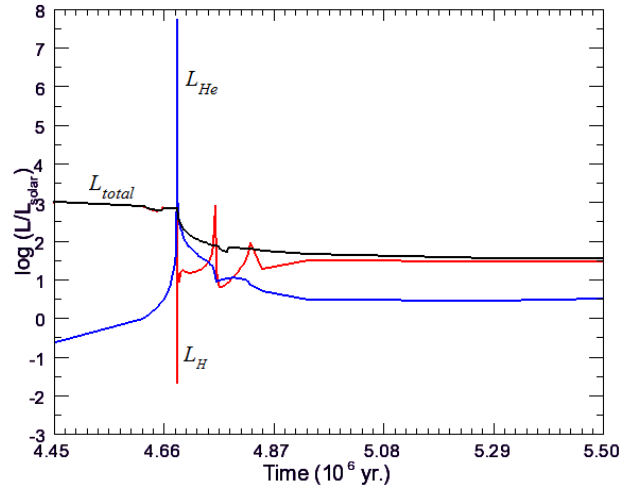


Figure 3-3: Evolution of the star's luminosity and the luminosities due to hydrogen and helium burning during the core helium flash in a $2M_\odot$ sequence. Time is set to zero at central He ignition.

Fig. 3-3 shows the variation of the luminosity of a $2M_{\odot}$ star through the core He-flash as a function of time. It is seen that the luminosity resulting from the He-burning increases flash-like to about $10^8 L_{\odot}$. Most of this power is used to expand the outer layers of the star. At this stage, the temperature is $\approx 2 \times 10^8 \text{K}$, and core degeneracy is almost lifted as it expands and cools. The helium flash is followed by subsequent mini-flashes through which the He-burning propagates until degeneracy is completely removed, He-burning proceeds quiescently in a convective core and the star settles on the *horizontal branch*.

The core helium flash requires very short time steps to accommodate the rapidly changing variables. Complete calculation is performed without interpolation. In our calculation, the time step is of the order of less than a year during the core helium flash. For stars of masses in excess of $2.2M_{\odot}$, no significant degeneracy effects occur, so that core He-burning proceeds under hydrostatic conditions.

3.2 IMS: The Blue Loop

A remarkable and intriguing feature during the evolution of stars in the mass range $4-12M_{\odot}$ is that they develop blue loops after the onset of core helium burning, when they reach the red giant branch (RGB). The blue loop is a crossing in the HR diagram towards higher effective temperatures (blue side) and back to the RGB (pt. 8 to 10 in Fig. 1-5). It is well established that the blue loops are necessary for explaining the observed non-variable yellow giants, supergiants and the δ -Cepheids in open galactic clusters (Mermilliod 1981; Schmidt 1984; Evans 1993; Fernie et al. 1995).

The study of the formation and evolution of the blue loops during core helium burning in IMS involves various aspects of stellar evolution. A basic discussion is given in the text by Kippenhahn & Weigert (1990) and references therein. In particular, the extension of the loops (the location of their bluest tips from the RGB in the HR diagram) depends on the stellar mass and on key reaction rates determining the efficiency of H-shell burning.

It is known that the blue loop is triggered when the hydrogen-shell (H-shell) burning is reinforced during core He-burning (see for example El Eid 1995; Lai & Li 2011). Hydrogen burning by the CNO cycle is controlled by the key bottleneck reaction $^{14}\text{N}(p, \gamma)^{15}\text{O}$ (shortly N14 rate) (see Fig. 1-3). The rate of this reaction was re-evaluated by Adelberger et al. (2011) and found to be reduced by about 40-50% with respect to the rate previously tabulated by the NACRE collaboration (Angulo et al. 1999) in the relevant temperature range. The effect of the N14 rate on the properties of the loop has been previously studied (Xu & Li (2004) and Weiss et al. (2005) for example); however, our work (Halabi et al. 2012) was the first to investigate the effect of this new evaluation of the rate on the blue loop. Using this revised rate, we found a remarkable suppression of the blue loops in intermediate mass stars due to the less efficient H-shell burning. This suppression is challenged by the observations in this part of the HR diagram. The new models in the mass range $5-7M_{\odot}$ have shortened loops that undesirably leave a considerable number of observed stars unexplained.

The efficiency of the rate cannot be de-coupled from the physical conditions in the shell region. Therefore, in order to explain this effect, we studied in detail the physics underlying the loop phenomenon and proposed solutions to restore it. What follows briefly summarizes the main results. The reader may refer to Appendix 2 for details.

3.2.1 Results of the evolution during the blue loop phase

A set of evolutionary sequences of stars in the mass range $5-12M_{\odot}$ with solar-like initial composition $(X, Y, Z) = (0.7, 0.28, 0.02)$ is calculated. The stellar models are evolved from the zero-age main sequence till the end of core helium burning. Three different rate compilations of the N14 rate are adopted:

1. The NACRE collaboration rate (Angulo et al. 1999) (N-rate),
2. The LUNA collaboration rate (Imbriani et al. 2005) (L-rate).
3. A new evaluation of this rate as described in Halabi et al. (2012) (C-rate).

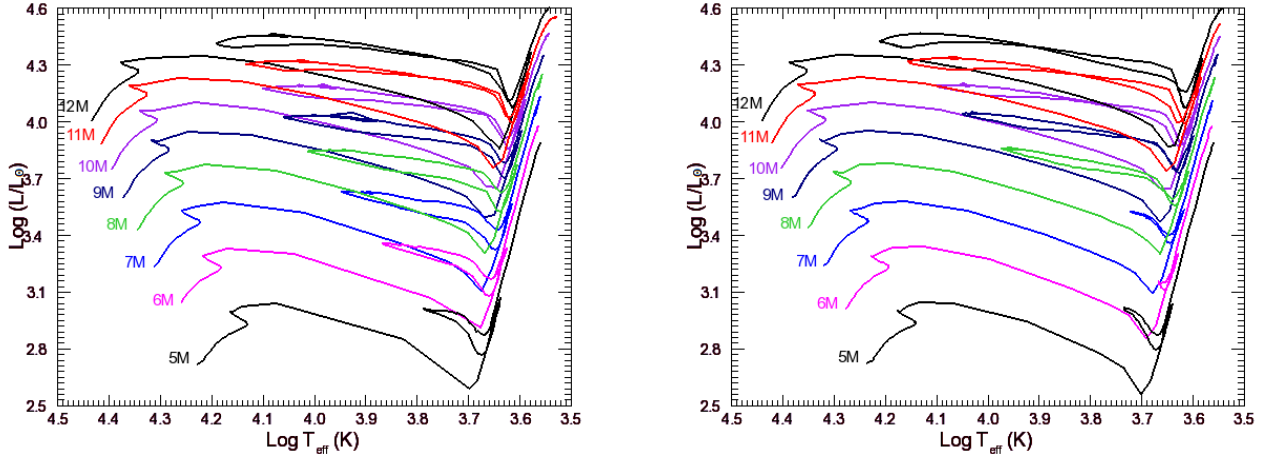


Figure 3-4: Evolutionary tracks in the HR diagram for the indicated stellar masses evolved from the zero-age main sequence till the end of core helium burning. The only difference between the two cases is the used N14 rate: N-rate (left), C-rate (right). See text.

The evolutionary tracks in Fig. 3-4 are obtained with the same input physics except for the N14 rate. The results with the N-rate (left panel) and C-rate (right panel) are presented here. A comparison of the two cases shows an interesting effect of the rate on the blue loops. The extension of the loops in the sequences 5–7 M_{\odot} are significantly reduced with the C-rate. Note that the L-rate shows a similar effect (see Appendix 2).

It is clear that a reduced rate proposed on experimental grounds leads to a severe suppression of the loop in the mass range 5–7 M_{\odot} . Two effects of this rate are identified: one is its influence on the depth of the H-discontinuity during the first dredge up on the RGB prior to the loop phase, and the other effect is its impact on the efficiency of shell H-burning during this phase. These two effects are acting differently depending on the stellar mass range. This is explained as follows:

- a. In case of stellar masses below 5 M_{\odot} , convection in the envelope creates a H-profile that is deep enough in mass, but the temperatures in the layers of shell H-burning are not high enough to enforce the H-shell burning. The evolutionary track thus remains close to the RGB and no extended loop is formed. Thus, a modified N14 rate will not change this conclusion.

b. In case of stellar masses between $5M_{\odot}$ and $7M_{\odot}$, the situation is entirely different. The location of the H-discontinuity created by the envelope convection and the temperatures achieved in the region of the H-discontinuity are both crucial in determining the formation and extension of the loop (see Figure 11 in Appendix 2). The effect of the N14 rate is most pronounced in this mass range and its efficiency plays a decisive role here because the temperatures in the proximity of the H-discontinuity are not as high as those in stars of masses above $7M_{\odot}$. Moreover, the less efficient shell H-burning with the weak C-rate causes an insufficient expansion of the envelope on the RGB (Figure 10 in Appendix 2), which results in a less deep H-profile. The combined effect of these factors causes a severely reduced loop.

c. In case of stellar masses above $7M_{\odot}$, the rate has a marginal influence, because the shell source is strong enough owing to the high temperature encountered in the neighborhood of the H-discontinuity in these stars to initiate a well extended loop.

Since the N14 rate we used is experimentally supported, this suppression of the blue loops in the intermediate mass range should be corrected for in the models in order to explain a large number of observed Cepheid variables and giants. One way to restore the loops is to invoke convective overshooting, which is discussed in the next section.

3.2.2 Effects of overshooting on the blue loops

Core overshooting has been invoked in the context of blue loops in several works (Matraka et al. 1982; Stothers 1991; Neilson et al. 2011). Envelope overshooting at the base of the convective envelope on the RGB also affects the loop properties (Alongi et al. 1991; Stothers & Chin 1991; Lai & Li 2011). In order to test the role of overshooting, we adopt the description outlined in Section 2.1.2, that is extending the edge of the convective region with the modified diffusion coefficient (eqn. 2.7). We consider core overshooting as well as envelope overshooting and describe the results in the following.

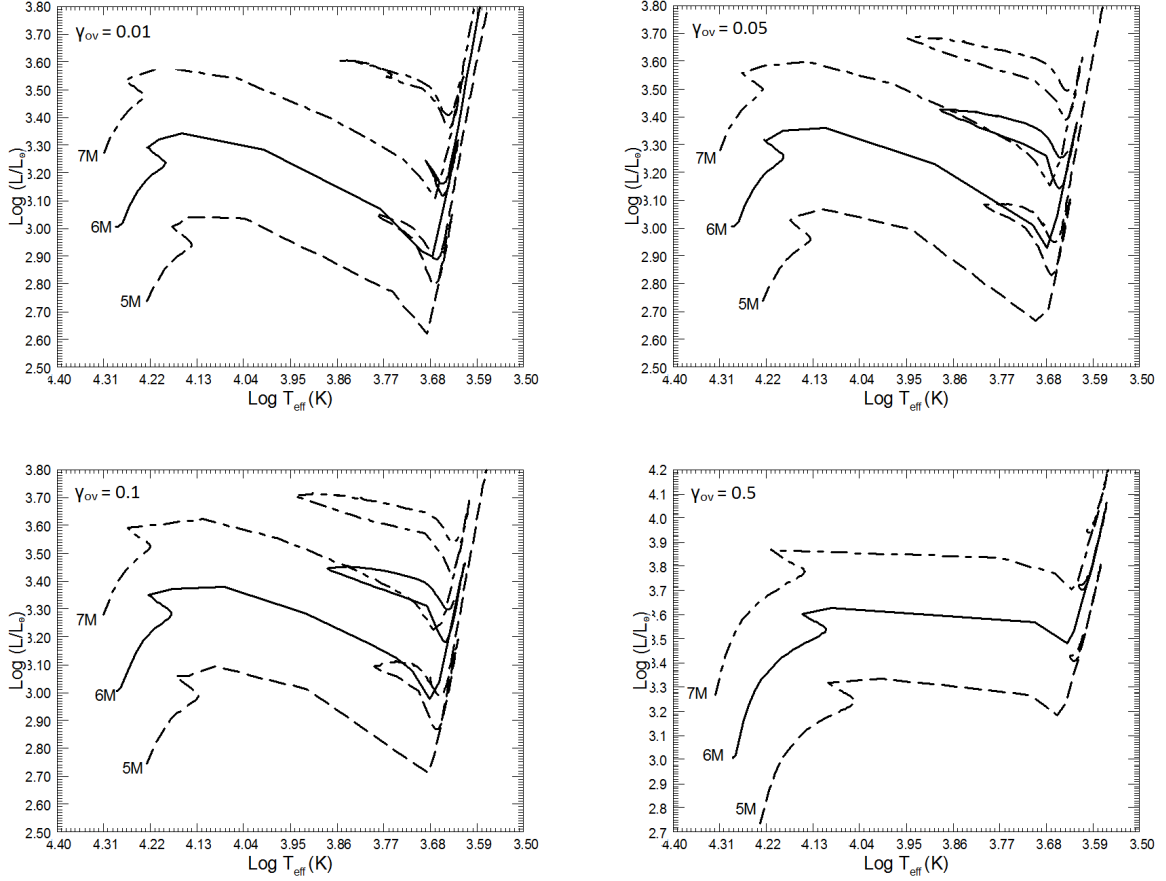


Figure 3-5: Evolutionary tracks of stars of masses $5M_{\odot}$ (dashed line), $6M_{\odot}$ (solid line) and $7M_{\odot}$ (dot-dashed line) for values of γ_{ov} as indicated, with $f = 0.25$. See text.

a. Core overshooting

For the aim of investigating the effect of core overshooting on the blue loops, stellar models of 5, 6 and $7M_{\odot}$ are evolved through central H- and He-burning phases, with the overshooting parameters $f = 0.25$ and $\gamma_{ov} = 0.01, 0.02, 0.05, 0.1, 0.2$ and 0.5 . Fig. 3-5 shows the results with various values of γ_{ov} . The tracks in the HR diagram are indeed sensitive to this variation. In particular, in all the three sequences the loops are completely suppressed for $\gamma_{ov} \geq 0.5$ and they are well extended for γ_{ov} near 0.1 , which we consider to represent moderate core overshooting.

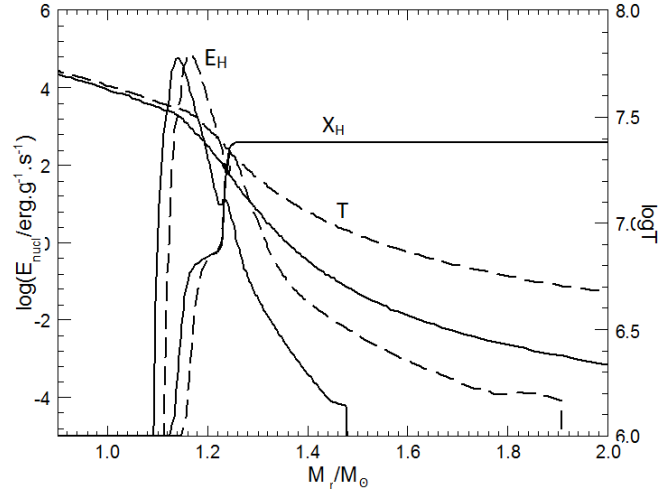


Figure 3-6: Energy generation rate by H-shell burning (E_H), temperature profile (T) and the hydrogen profile (X_H) as a function of interior mass of the considered $6M_\odot$ star for $\gamma_{ov} = 0$ (sequence A, solid lines) and 0.5 (sequence B, dashed lines). The snapshot is taken at $X_c(\text{He}) = 0.5$ for both sequences, which marks the onset of the loop in sequence B. Note that the hydrogen abundance is shifted upwards to $2X_H + 6$ in order to match the scale of the right-side axis.

This behavior is explained by investigating the evolution of shell H-burning. Considering the $6M_\odot$ star, we compare in Fig. 3-6 the energy generation rate due to shell H-burning, the temperature profile and H-profile in the 2 cases: no overshooting ($\gamma_{ov} = 0$, sequence A), and with overshooting ($\gamma_{ov} = 0.1$, sequence B). In sequence B, the H-shell is shifted outwards in mass owing to the larger convective core. It is remarkable that the temperature does not decrease as fast as in the case without overshooting. Consequently, the higher temperature in the H-shell region enforces shell H-burning in this case, which restores the blue loop.

The results with $\gamma_{ov} = 0.5$ (sequence C) are shown in Fig. 3-7, in which we compare this sequence to sequence B ($\gamma_{ov} = 0.1$), taken at the same evolutionary phase as in Fig. 3-6. It is clear that in sequence C, the H-burning shell is located too far out in

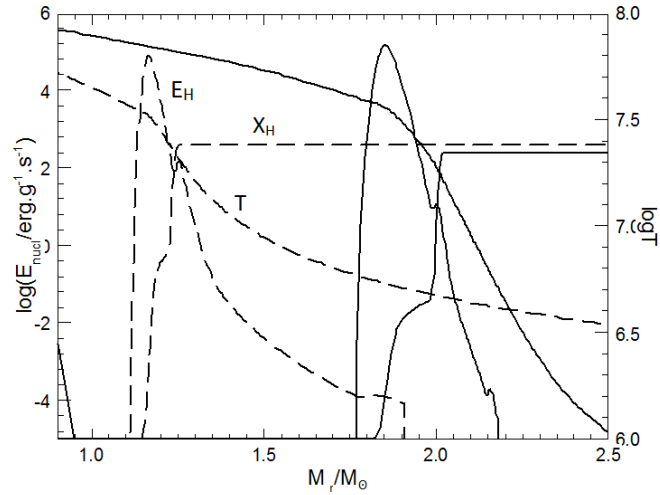


Figure 3-7: Same as Figure 3-6, but for sequence B with $\gamma_{\text{ov}} = 0.1$ (dashed lines) and sequence C with $\gamma_{\text{ov}} = 0.5$ (solid lines). The snapshot is taken at $X_c(\text{He}) = 0.5$ which marks the onset of the loop in sequence B.

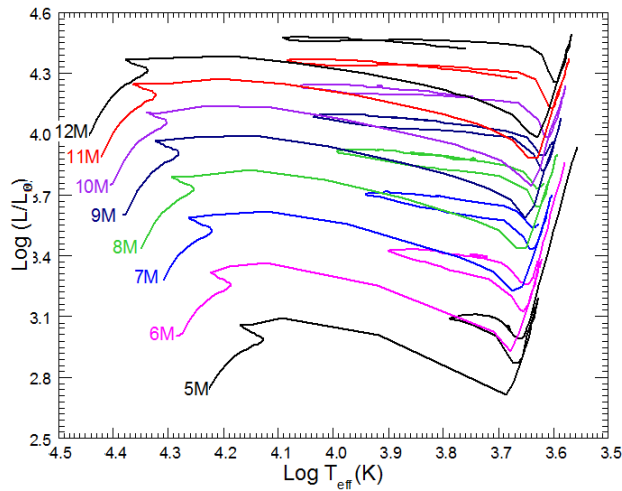


Figure 3-8: The evolutionary sequences calculated with the C-rate, and with $\gamma_{\text{ov}} = 0.1$. Note how the previously suppressed loops are now restored.

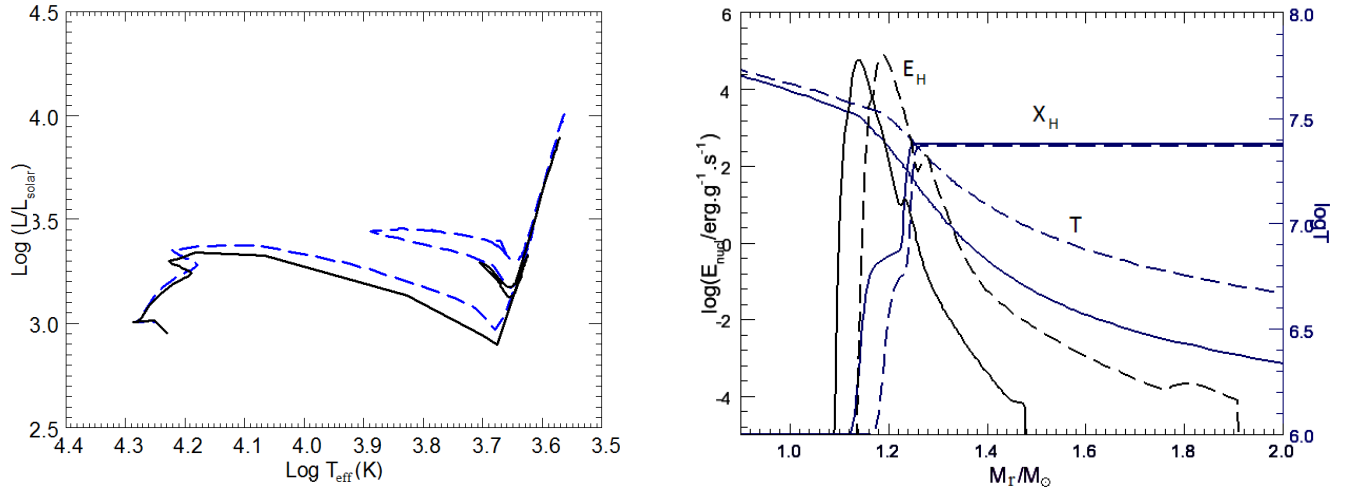


Figure 3-9: Left panel: The loop of a $6M_{\odot}$ in the standard calculation (solid line) and with core and envelope overshooting (dashed line). Right panel: Same as Fig. 3.6, calculated with the C-rate for the two cases: standard calculation (solid lines) and with core and envelope overshooting (dashed lines).

mass, where the temperature is relatively low and thus cannot support efficient burning to initiate a blue loop. Consequently, a parameter $\gamma_{ov} = 0.5$ is not realistic at all.

These results show that the blue loops in IMS may help to constrain the overshooting parameter in the framework of the diffusion model we are using. Adopting $\gamma_{ov} = 0.1$ as our optimal choice, we show in Fig. 3-8 that the blue loops are restored indeed.

b. Core and Envelope overshooting

To elaborate on the above discussion, we consider both core overshooting and envelope overshooting by taking again the $6M_{\odot}$ star as a test case, adopting $\gamma_{ov} = 0.1$ at both convective boundaries with the C-rate.

Fig. 3-9 shows the results. The inspection of the right panel reveals that the effect of core overshooting is to establish higher temperatures in the H-shell region, while envelope overshooting leads to a deeper penetration of the H-profile, i.e. closer to the H-shell source. In this case, the H-shell burning is more efficient and the extension of the loop is restored (left panel of Fig. 3-9). The extension of the loop in this case is similar to that

with core overshooting alone (see the panel corresponding to $\gamma_{ov} = 0.1$ in Fig. 3-5).

The conclusion is that core overshooting is more efficient concerning the blue loop behavior in the mass range specified above.

3.2.3 Comparison with Observations

A comparison with observations may indeed help to support our conclusions in the previous section. A first comparison is shown in Fig. 3-10, where the evolutionary tracks are obtained using the C-rate for the $^{14}\text{N}(p,\gamma)^{15}\text{O}$ and with $\gamma_{ov} = 0.1$. We have concluded that this choice gives the right extension of the blue loop, especially in the mass range $5\text{-}7M_{\odot}$. Superimposed on the evolutionary tracks are observed data for 17 observed yellow giants and supergiants and 9 Cepheids according to Schmidt (1984) as well as a large number of observed Cepheids (over 500) by Fernie et al. (1995), from the online Galactic classical Cepheids database (David Dunlap Observatory).

A nice agreement can be seen between the data and the theoretical tracks, so the treatment of overshooting with $\gamma_{ov} = 0.1$ is rather reasonable and justified.

Another comparison with observations concerns the ratio τ_b/τ_r , which corresponds to the evolutionary time spent during core helium-burning on the blue side of the loop to that on the red side of the HR diagram (RGB). The ratio is obtained by taking the dividing temperature at $\log T = 3.7$ which corresponds to the classification of the giants between G and K spectral classes (Lai & Li 2011). This ratio is useful because it can be associated with the observed number ratio of blue to red giants in clusters N_b/N_r . Such an association has been used in previous works (Stothers 1991; El Eid 1995; Lai & Li 2011). In Halabi et al. (2012), we showed how the three used N14 rates affect the ratios τ_b/τ_r of the sequences: 5, 6 and $7M_{\odot}$. It was found that the C-rate causes a systematic reduction in the τ_b/τ_r ratio mostly in the mass range $(5\text{-}10)M_{\odot}$ (see Table 1 and discussion in Appendix 2 for details).

In order to see how core overshooting affects the τ_b/τ_r ratio, Table 3.1 shows the theoretically predicted τ_b/τ_r for the 3 sequences: 5, 6 and $7M_{\odot}$ as obtained with the

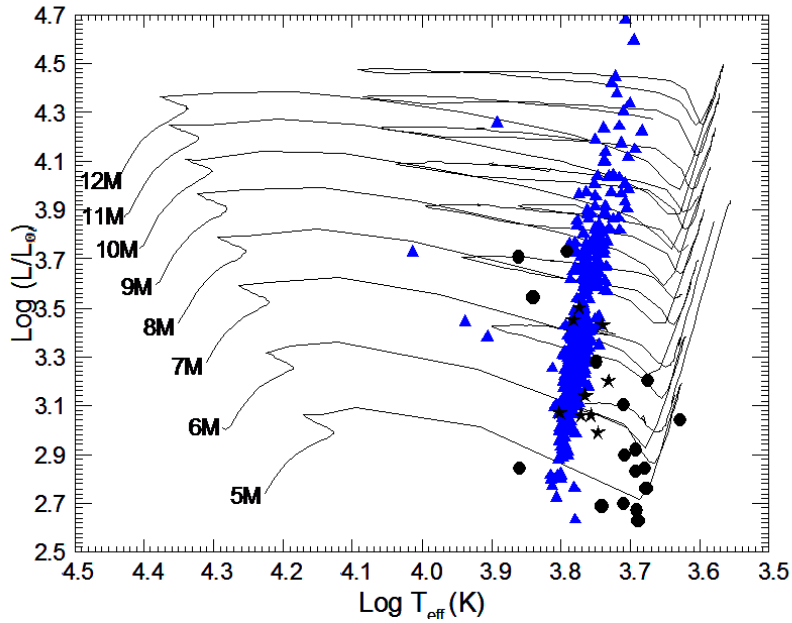


Figure 3-10: Sequences of mass 5-12M_⊙ obtained with the C-rate and $\gamma_{ov} = 0.1$. The triangles denote the observed Galactic Classical Cepheids by Fernie et al. (1995). Observations by Schmidt (1984) are indicated by asterisks and closed circles which represent Cepheid stars and yellow giants in open clusters respectively. The temperature range of the instability strip predicted by the models agrees with that of the observed Cepheids and yellow giants.

Table 3.1: The theoretically predicted ratio τ_b/τ_r for different values of the overshooting parameter γ_{ov} for the three sequences 5, 6 and $7M_\odot$.

M(M_\odot)	$\gamma_{ov} =$	0	0.05	0.1	0.2	0.5
5		0.19	1.16	1.3	0.65	0
6		0	1.63	2.14	1.8	0
7		0.454	3.587	5	2.49	0

C-rate and with $\gamma_{ov} = 0, 0.05, 0.1, 0.2$ and $0.5H_p$. The Table exhibits several features:

1. τ_b/τ_r is a steadily increasing function of the stellar mass in the considered mass range, except for the cases where the loop is suppressed ($\tau_b/\tau_r = 0$).
2. τ_b/τ_r increases when γ_{ov} is increased from 0 to 0.1. For $\gamma_{ov} > 0.1$, τ_b/τ_r starts to decrease in the 3 sequences. This feature was shown in Fig. 3-5, and the reason of suppression of the loop with $\gamma_{ov} = 0.5$ is explained in the previous section.

The direct comparison between τ_b/τ_r ratio and the observed number ratio N_b/N_r is not easy because such observations are subject to large uncertainties that are mainly due to the lack of observations of obscured faint red giants. Therefore, we shall not expect a very precise agreement between the observed N_b/N_r and the theoretical τ_b/τ_r . The observed ratio by Stothers (1991) is $N_b/N_r = 1.7 \pm 0.4$ for young clusters. Carson & Stothers (1976) found values of 0.33 and 1.0 for middle aged clusters and young clusters for the two age groups of masses roughly $5M_\odot$ and $7M_\odot$ respectively. Maeder & Meynet (1989) pooled the data for both young and intermediate age clusters and found the value to be $N_b/N_r \approx 1$. We find that the observed values are compatible with the results obtained with the choice $\gamma_{ov} = 0.1$.

Another comparison is possible with the results by Criscienzo et al. (2012). They provide an interpretation of the properties of observed Galactic and Magellanic classical Cepheids using pulsation models that are based on updated model atmospheres. Depending on the chemical composition, mass and luminosity of the star, their proposed pulsation models define a temperature range that corresponds to the position of the instability strip boundaries (extension of the blue loop). We use their values of luminosities

Table 3.2: Predicted model properties (M , L and T_{eff}) of Classical Cepheids adopted from Criscienzo et al. (2012). M_{RGB} denotes the theoretical mass of our evolved models in the region of observations in the HR diagram. (r) denotes the red edge of the instability strip and (b) denotes its blue edge.

label	M/M_{\odot}	M_{RGB}/M_{\odot}	$\log L/L_{\odot}$	$T_{eff} (r)$	$T_{eff} (b)$
a	5	4.96	3.070	5600	6050
b	6.25	5.92	3.420	4950	5550
c	7	6.87	3.650	4650	5450
d	9	8.73	4.000	4350	5150
e	11	11.3	4.400	3850	4850

and temperatures corresponding to solar metallicity stars of masses 5, 6, 7, 9 and $11M_{\odot}$. Since core overshooting increases the luminosity of the star during the blue loop, a constraint on the luminosity of individual models can be useful. The adopted values are shown in Table 3.2 and the comparison with the tracks are shown in Fig. 3-11. The observationally inferred luminosities, effective temperatures and masses largely agree with our theoretical models with $\gamma_{ov} = 0.1$. Note that in our models, mass-loss is taken into account, with the mass-loss rates outlined in Section 2.1.1. Therefore, we do not compare the masses given by Criscienzo et al. (2012) to the initial mass but rather to the mass of the evolved model, which is denoted by M_{RGB} . The values agree to a high extent (less than 5% difference) (Halabi 2014).

To conclude, and based on the several observations presented, we favor a core overshooting distance of $0.1H_p$ in stars of masses 5 to $12M_{\odot}$.

This particular value of core overshooting will be used to study its effect on the critical progenitor mass that produces an ONe white dwarf in the post-AGB phase in stars in the mass range $(8-12)M_{\odot}$. Details are provided in Chapter 6.

3.2.4 Comparison with Other Investigations

After having found a reasonable choice for the amount of convective overshooting that is justified by several observational data, it is useful to compare this value to that favored by other investigations. Among the many works on the effect of core overshooting on

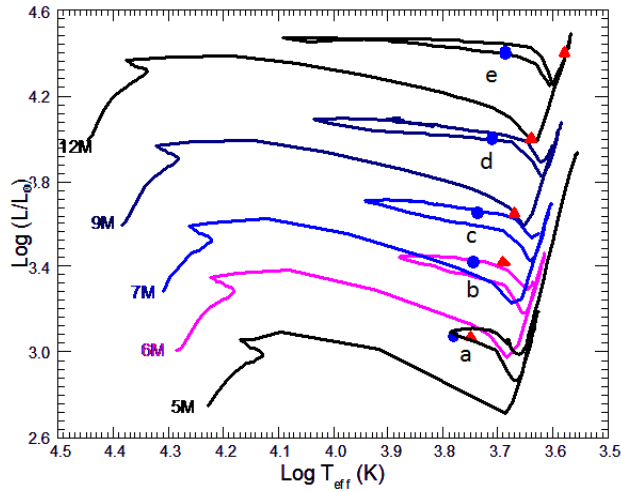


Figure 3-11: The luminosities and the range of the instability strip of the predicted models (a) to (e) shown in Table 3.2. Circles mark the blue edge, while triangles mark the red edge. The initial masses of the models are also shown, while the masses of the evolved models (M_{RGB}) are listed in Table 3.2.

the blue loop, we choose the ones that use a similar treatment of convective mixing and overshooting, so that a direct comparison with their results is possible. In these works, the overshooting distance is also expressed in terms of the pressure scale height, i.e. $d_{ov} = \gamma_{ov} H_p$.

Aerts et al. (2003) and Dupret et al. (2004) use observed seismic data to constrain the amount of overshooting and find $\gamma_{ov} = 0.10 \pm 0.05$. Ventura et al. (2005), Claret (2007), Cassisi & Salaris (2011), Neilson et al. (2012) and Prada Moroni et al. (2012) suggest $\gamma_{ov} = 0.2$ based on photometric studies of open clusters and observational data of eclipsing binary systems. Neilson & Langer (2012) suggest that the value of γ_{ov} required to match the same observations ranges between $0.2 - 0.35$. Briquet et al. (2012) suggest $\gamma_{ov} \sim 0.1$ for some variables. This comparison indicates that our choice is in general agreement with other investigations as well.

3.3 Red Giant Stars: Evolution & Mass Determination

In this part, we use the grid of evolutionary tracks of $(1.2-7.3)M_{\odot}$ stars presented in Fig. 3-1 in order to determine the stellar mass of observed red giants. Determining the mass of these observed giants will be helpful later on to investigate their isotopic surface abundances and constrain important physical process by comparing the theoretical predictions with observations.

We consider a sample of red giants observed by Tsuji (2008) (hereafter Tsuji08) whose details are given in Table 1 in Appendix 3. The effective temperatures are determined using the infrared flux method (Blackwell 1980). The bolometric luminosities are obtained by integrating the spectral energy distributions and the Hipparcos parallaxes are used to determine the absolute bolometric magnitudes.

The evolutionary tracks are shown in Fig. 3-12 in addition to the observational values of M_{bol} and T_{eff} . It is important to mention that this mass determination is not sensitive to overshooting. In IMS the luminosity, and consequently, the bolometric magnitude M_{bol} are sensitive to core overshooting prior the AGB phase, but not along the AGB. This can be clearly seen in the left panel of Fig. 3-9, which shows that the evolutionary track of a $6M_{\odot}$ star obtained in the standard calculation coincides with that obtained with overshooting along the AGB phase. Similarly, overshooting does not affect the luminosity of the LMS during their ascent along the RGB phase. Thus, our mass determination is not influenced by overshooting.

It is also important to note that a direct comparison of the theoretical temperature to that inferred observationally wouldn't have been possible if the sample stars are pulsating Mira variables, in which case a radius cannot be strictly defined and any comparison would not hold (Baschek et al. 1991; Lebzelter et al. 2010). Even the term effective temperature may become questionable for the very evolved AGB stars featuring strong pulsations and mass-loss. However, in this sample, the stars are on the RGB or E-

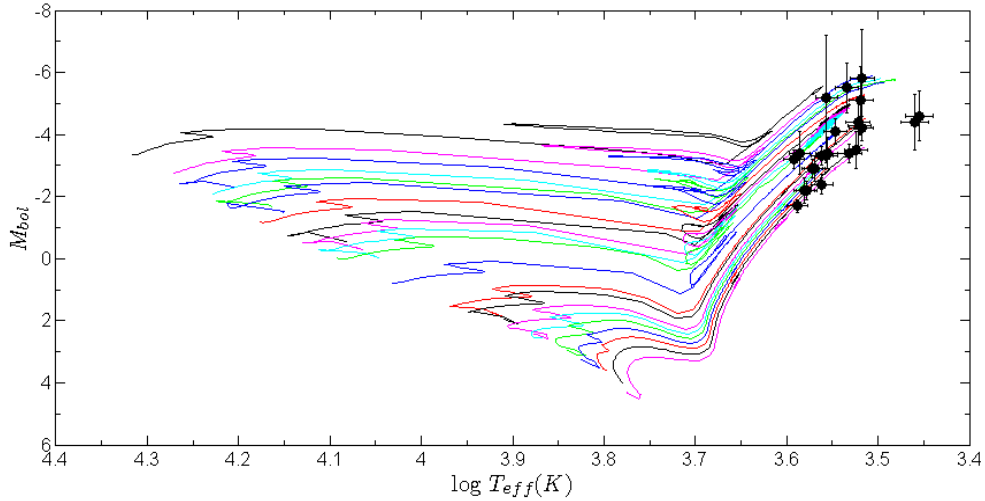


Figure 3-12: The bolometric magnitude (M_{bol}) versus effective temperature (T_{eff}) diagram showing evolutionary tracks of stars of mass $(1.2-7)M_{\odot}$. Observations by Tsuji08 are also shown.

AGB phase, and thus, have not yet experienced any thermal pulsations. This makes such a comparison between the theoretical effective temperature and the observationally inferred one rather possible and valid. The theoretical bolometric magnitude is obtained according to the well known relation: $M_{bol} = 4.75 - 2.5 \log(L/L_{\odot})$ (Karttunen 2003).

It is clearly seen in Fig. 3-13 that the tracks describe well the advanced evolutionary stage of these stars. Fig 3-14 shows the derived masses and how they compare to those by Tsuji08 and to other observational determinations. The error on the mass is determined from the error bars on M_{bol} and T_{eff} from Tsuji08. The values are also listed in Table 2 in Appendix 3. It can be seen that the masses determined in this work are systematically lower than those obtained by Tsuji08. We attribute this to two main reasons:

(a) The stars are evolved to the stage where they are observed, that is, we do not use any extrapolated tracks. The masses by Tsuji08 are based on evolutionary tracks of Claret (2004) extrapolated at temperatures below 3200K for almost half of the sample, which may introduce errors.

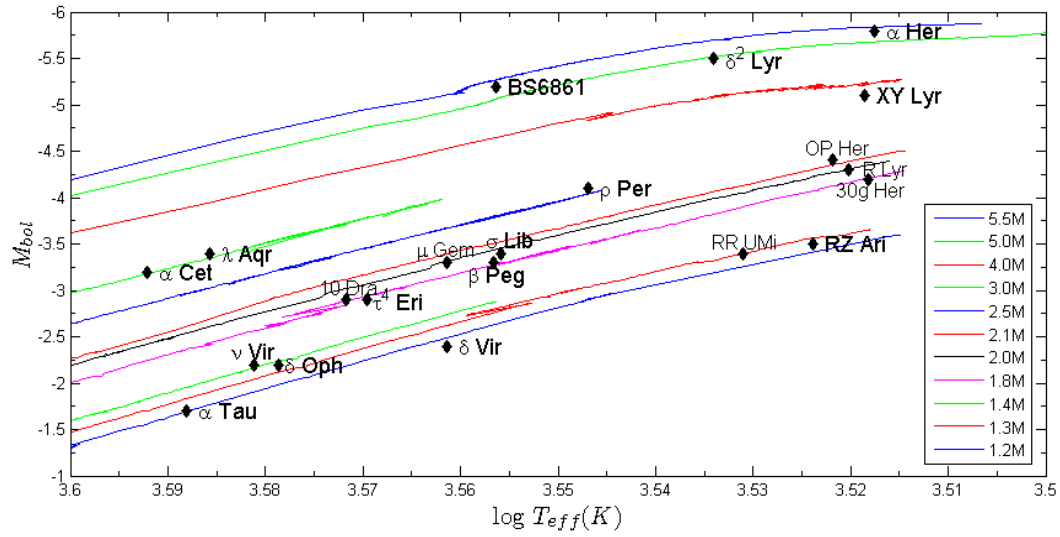


Figure 3-13: The evolutionary tracks covering advanced phases together with the observed red giants, see text.

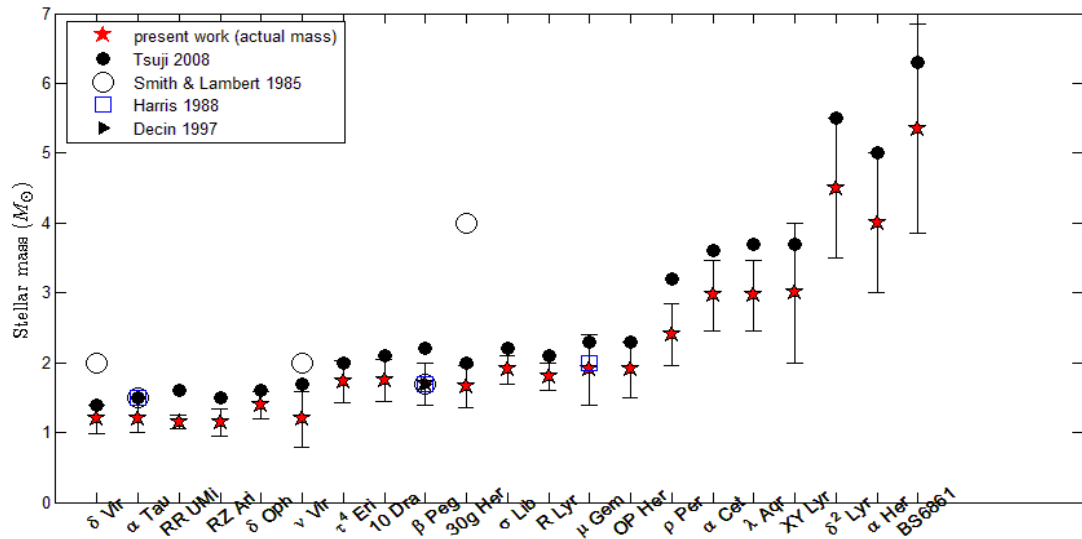


Figure 3-14: Comparison of the masses of the observed sample of stars with other works as indicated.

(b) We have taken into consideration mass-loss effects, which become significant for more massive stars, as can be seen in Fig 3-14.

Moreover, it is clear that our errors on the mass are generally lower than those by Tsuji08. Calculating the tracks up to advanced stages helps to get better estimation of the masses of red giants. Having obtained the masses of the observed sample, we are able to identify the evolutionary stage of the stars and we can compare their CNO surface abundances to the observational values, which is described in the next Chapter.

Chapter 4

Nucleosynthesis Prior the Early-AGB phase

4.1 CNO Surface Abundances in Red Giants

In this section, we present the results obtained for the CNO surface abundances of the sample of stars evolved till the early AGB phase and compare them with the CNO isotopic ratios inferred from observations (Halabi & El Eid 2014 (MNRAS), submitted and under revision). First, the abundance profiles of the CNO isotopes and those of H and He prior to the FDUP are shown in Figs. 4-1. In order to study the variation of these abundance profiles as a function of the initial stellar mass, we selected the masses 1.4, 2, 3 and $5M_{\odot}$. Several features can be identified in these figures:

(a) The isotope ^{13}C is produced near the middle of the star by the CN cycle in all cases. This reflects the relatively low temperatures required for the production of this isotope in stars by the CN-cycle (see Fig. 1-3).

(b) The ^{17}O profile is remarkable, showing a steep gradient in the central region of the star. This is because ^{17}O is produced by the ON cycle which requires higher temperatures to become effective.

(c) The isotope ^{18}O is rapidly converted to ^{15}N by the reaction $^{18}\text{O}(p, \alpha)^{15}\text{N}$.

(d) The elements ${}^4\text{He}$ and ${}^{14}\text{N}$ are produced, being the typical products of the CNO cycle.

These results are well known in the literature, but it is important to understand the surface abundances resulting after FDUP and SDUP for different stellar masses. It is also important to study the modification of these abundances by extra mixing or overshooting as discussed earlier. The efficiency of FDUP in changing the surface abundances is linked to the maximum penetration of the convective envelope on the RGB. In Fig 4-1, the solid vertical line marks the maximum penetration by convective mixing that results from applying the Schwarzschild criterion of convection. The dashed vertical line is that resulting when overshooting is considered (as described in Section 2.1.2).

After FDUP, the change in the surface composition depends on the profile of the isotope formed in the star. The peak of the ${}^{13}\text{C}$ profile is located in the middle part of the star, so that envelope convection is able to smear out the profile which causes an increase of the ${}^{13}\text{C}$ surface abundance, or a decrease in the ${}^{12}\text{C}/{}^{13}\text{C}$ ratio. The ${}^{17}\text{O}$ abundance profile is of particular interest. The production of ${}^{17}\text{O}$ is highly dependent on the stellar mass because it is mainly in the inner part of the star. Therefore, its profile exhibits a steep gradient at the region of maximum convective penetration. Fig. 4-1 (upper panel) shows that in stars of $M \leq 2M_{\odot}$ envelope convection does not completely smear out the ${}^{17}\text{O}$ peak. This makes the ${}^{17}\text{O}$ profiles sensitive to mixing in stars of $M \leq 2M_{\odot}$, so that any additional mixing below the envelope will increase the surface abundance of ${}^{17}\text{O}$. This effect is less pronounced for stars with $M \geq 3M_{\odot}$ (Fig. 4-1 (lower panel)), where the ${}^{17}\text{O}$ bump is fully engulfed by the “formal” convective envelope, so overshooting will not significantly alter the surface abundance of these stars.

Comparing the calculated abundances with the observed data can be very useful to improve the treatment of convective mixing and constrain overshooting in the stellar interiors, especially in low mass stars. However, a direct comparison is not an easy task since this comparison is model-dependent on both theoretical and observational grounds.

On one hand, deriving the C and O ratios observationally involves several sources of

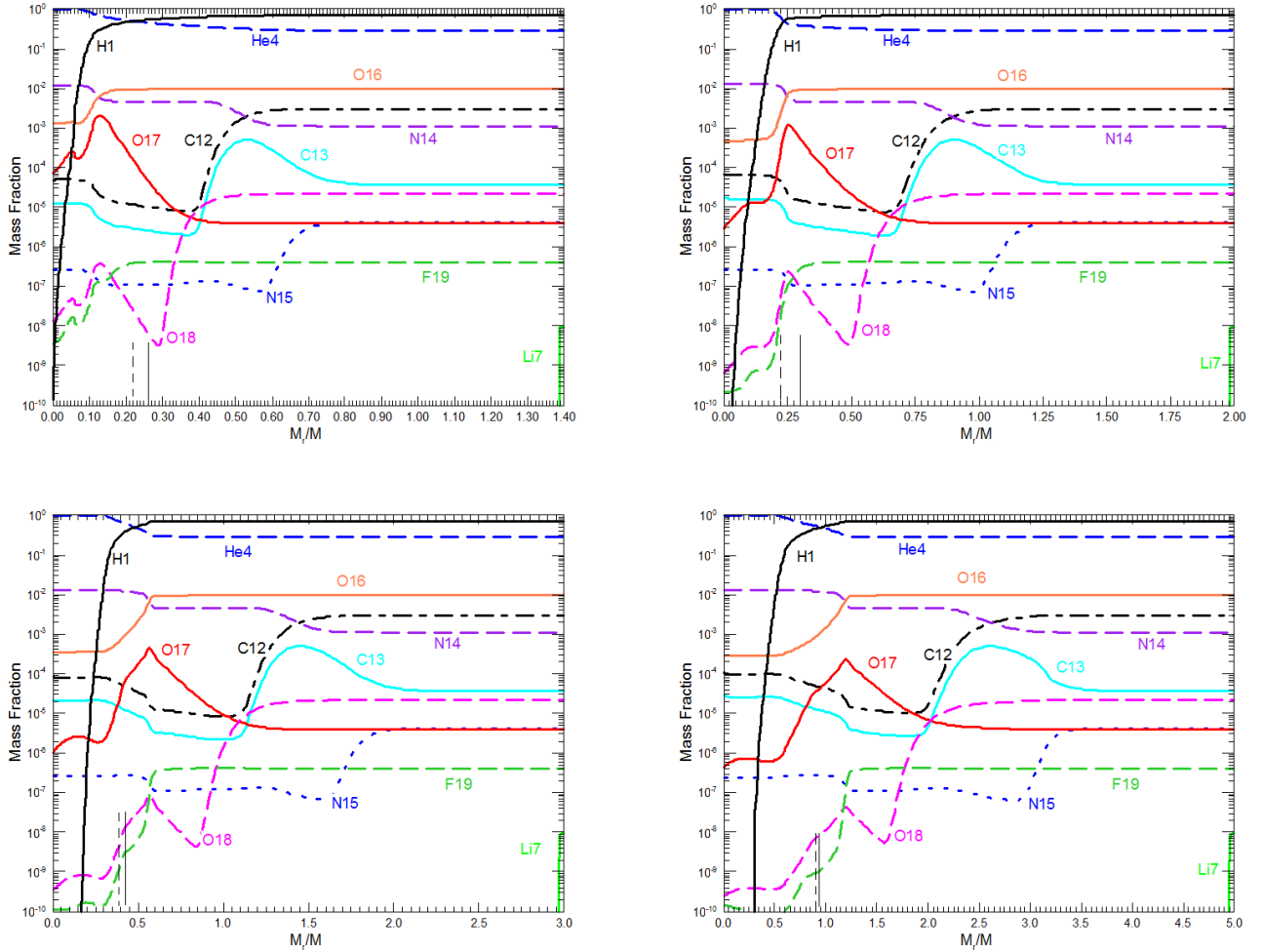


Figure 4-1: Abundance profiles after core H-burning for several products of the CNO cycle in the stellar masses $1.4M_{\odot}$ (upper left), $2M_{\odot}$ (upper right), $3M_{\odot}$ (lower left) and $5M_{\odot}$ (lower right). The solid lines mark the deepest penetration in mass of the convective envelope, while the dashed lines mark the deepest penetration with overshooting. See text for details.

uncertainty like the dispersion in the ratios obtained from different lines, and inaccuracy in the atmospheric model parameters. Systematic errors may also be present, such as the uncertainty in the continuum position and departures from local thermodynamic equilibrium (LTE) (Abia et al. 2012), in addition to the difficulties that are inherent in the spectral analysis of very cool stars. The fact that atmospheric values are model-dependent causes discrepancies between observational results among different groups, and consequently, affect the subsequent discussion (Ramstedt & Olofsson 2014). On the other hand, theoretical models are also challenged by uncertainties in convective mixing, mass-loss and nuclear reaction rates, where standard FDUP models often face difficulties in explaining C and O surface abundances, particularly in LMS. This comparison is nonetheless beneficial for a better understanding.

4.2 Overview of observations

A large body of observational data is available for the CNO abundances in the envelopes of RGB stars (Lambert & Reis 1981; Harris & Lambert 1984a,b; Lambert et al. 1986; Harris et al. 1988; Gilroy & Brown 1991; Tsuji 1991; Charbonnel 1994; Tsuji 2008; Tautvaišienė et al. 2010; Piau et al. 2011). Despite the involved uncertainties and limitations, these data provide a powerful tool to get insight into the internal structure of evolved stars. To compare our theoretical predictions of these elements and their ratios with observations, the abundances of a sample of red giants observed by Tsuji08 are considered.

The $^{16}\text{O}/^{17}\text{O}$ ratios are based on a line-by-line analysis of the isolated lines of $^{12}\text{C}^{16}\text{O}$, $^{13}\text{C}^{16}\text{O}$, and $^{12}\text{C}^{17}\text{O}$ abundances. The $^{16}\text{O}/^{17}\text{O}$ ratio of the same object differs considerably among different observations due to the aforementioned uncertainties in describing the properties of the relatively cool atmospheres of red giants. These uncertainties are introduced as error bars (see Appendix 3). We also consider the $^{16}\text{O}/^{17}\text{O}$ ratios by several others observations.

4.3 Comparison with observations & other investigations

Table 4.1 summarizes the values obtained for $^{16}\text{O}/^{17}\text{O}$, $^{12}\text{C}/^{13}\text{C}$ and $^{14}\text{N}/^{15}\text{N}$ after the FDUP and SDUP (for masses $\geq 3M_{\odot}$) with standard convective mixing (no overshooting) together with those inferred from observations by Tsuji08 and others. It is important to note that the stars of the sample analyzed by Tsuji08 are advanced in evolution, but did not experience the third dredge up during the AGB phase. This is evident from the surface carbon abundances (Tsuji 2014, private communication). Thus, the comparison can be restricted to the effects of FDUP and SDUP only. Fig. 4-2 shows these results as a function of the stellar mass, along with the theoretical predictions by Boothroyd & Sackmann (1999), Abia et al. (2012) and Karakas & Lattanzio (2014) as well as available observations for comparison. We note that the data points marked by filled triangles represent stars whose weak lines couldn't be measured at all for $^{12}\text{C}/^{17}\text{O}$, and thus their $^{16}\text{O}/^{17}\text{O}$ ratios are not well determined, but rather, only a lower limit is provided (Tsuji08).

This figure shows that for masses below $2M_{\odot}$, the predicted $^{16}\text{O}/^{17}\text{O}$ ratios are higher than most of the data points obtained from observations. This discrepancy shows that more ^{17}O needs to be mixed to the surface in order to lower the $^{16}\text{O}/^{17}\text{O}$ ratio in the models. This may be achieved by applying overshooting at the bottom of the convective envelope. This need for overshooting has been suggested in several investigations (Sweigart & Mengel 1979; Charbonnel 1994, 1995; Boothroyd et al. 1995; Denissenkov & Weiss 1996; Palemrini et al. 2011) as well as in connection with the evolution of field giants (Charbonnel & Do Nascimento 1998; Gratton et al. 2000), open clusters (Luck 1994; Tautvaišienė et al. 2000, 2005), globular clusters (Pilachowski et al. 2003; Shetrone 2003; Recio-Blanco & de Laverny 2007) as well as to explain isotopic ratios in pre-solar grains (Palmerini et al. 2013; Busso et al. 2014).

As shown in Fig. 1-8 in Chapter 1, in stars of mass less than 4 to $5M_{\odot}$ the SDUP

Table 4.1: M_{RGB} (in solar units) and the surface number abundances after FDUP and SDUP (if any, listed in parenthesis): a : surface abundances with standard mixing (present work), b : Tsuji08, g : Harris and Lambert (1984b), h : H85: Harris et al. (1985), i : Smith and Lambert (1990), j : Decin et al. (2003), k : Maillard (1974), l : Hinkle et al. (1976).

Object	M_{RGB}	$^{16}\text{O}/^{17}\text{O}^a$	$^{16}\text{O}/^{17}\text{O}^b$	$^{16}\text{O}/^{17}\text{O}$	$^{12}\text{C}/^{13}\text{C}^a$	$^{12}\text{C}/^{13}\text{C}^b$	$^{12}\text{C}/^{13}\text{C}$	$^{14}\text{N}/^{15}\text{N}^a$
δ Vir	1.19	2370	> 2500		32	12.3 ± 1.2	16 ± 4^i	551
α Tau	1.2	2370	> 1000	600_{+130}^{-150g}	30	10.6 ± 1.0	$10 \pm 2^{i,j}$	551
				525_{+250}^{-125g}			9 ± 1^g	
RRUMi	1.15	2006	> 2000		30	10.0 ± 0.8		598
RZ Ari	1.14	2006	607 ± 48		30	7.9 ± 0.8		598
δ Oph	1.39	1500	387 ± 68		29	11.1 ± 0.9		690
ν Vir	1.39	1500	> 2000		29	8.7 ± 1.3	12 ± 2^i	690
τ^4 Eri	1.73	461	687 ± 14		24	12.4 ± 0.3		963
10 Dra	1.74	461	151 ± 11		24	14.8 ± 1.6	12 ± 3^i	963
β Peg	1.7	462	> 2500	1050_{+500}^{-250g}	24	7.7 ± 0.5	8 ± 2^i	963
				$\geq 100^g$			5 ± 3^j	
30g Her	1.65	462	211 ± 42	$675_{-175}^{+175} h$	24	12.5 ± 1.1	10 ± 2^i	963
σ Lib	1.9	301	> 1500		22	7.5 ± 0.3		1126
R Lyr	1.8	301	368 ± 44		22	6.4 ± 0.3		1126
μ Gem	1.9	301	798 ± 73	$325_{+150}^{-75} g$	22	10.5 ± 1.2	13 ± 2^i	1126
				$\geq 100^g$				
OP Her	1.9	246	329 ± 31		22	11.3 ± 1.2		1103
ρ Per	2.4	234	> 1000		22	9.7 ± 1.0	15 ± 2^i	1307
α Cet	2.96	318(317)	586 ± 47		21(21)	11.1 ± 0.8	10 ± 2^j	1460(1501)
λ Aqr	2.96	318(317)	> 1000		21(21)	7.9 ± 1.4		1460(1501)
XY Lyr	3.0	424(395)	223 ± 16		21(20)	15 ± 0.4		1528(1610)
δ^2 Lyr	4.5	400(378)	465 ± 41		21(20)	16.2 ± 1.5		1503(1629)
α Her	4.0	424(402)	102 ± 8	180_{+70}^{-50g}	21(20)	11.1 ± 0.7	$17 \pm 4^{g,l}$	1538/1642
				200_{+25}^{-25g}				
				$\approx 450^g$				
				450_{+50}^{-50k}				
BS 6861	5.35	424(402)	> 1000		21(20)	48.5 ± 2.9		1538(1642)
Initial		2620			90			270

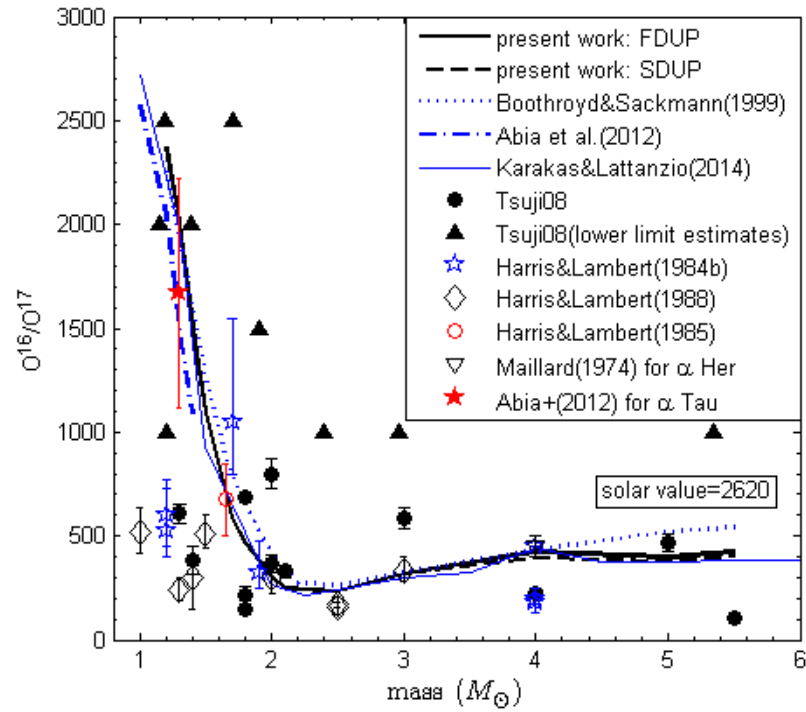


Figure 4-2: Calculated $^{16}\text{O}/^{17}\text{O}$ ratios after FDUP (solid line) and SDUP (dashed line) versus stellar mass. Calculation by Boothroyd & Sackmann (1999), Abia et al. (2012) and Karakas & Lattanzio (2014) are also shown. Observations are shown as data points.

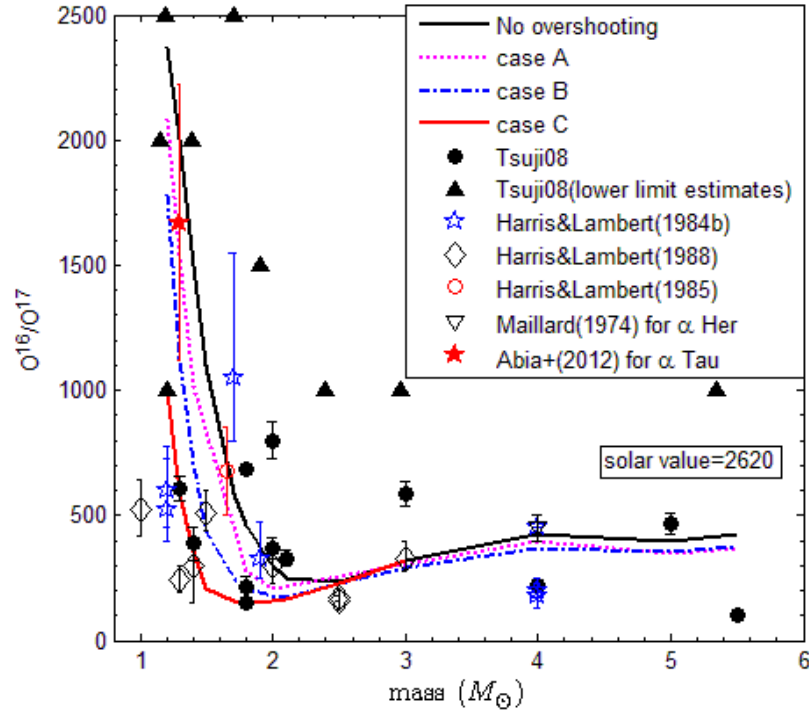


Figure 4-3: $^{16}\text{O}/^{17}\text{O}$ ratio when overshooting below the convective envelope is applied in the three cases A, B and C where each corresponds to a different efficiency of overshooting as discussed in text.

doesn't penetrate deeper than the FDUP, and thus does not introduce significant change to the surface composition. Therefore, in order to account for the discrepancy between calculated and observed values of $^{16}\text{O}/^{17}\text{O}$ in low mass stars, extra mixing below the convective envelope is required on the RGB phase, and not only on the AGB.

4.4 Calculated surface abundances with overshooting

Envelope overshooting is applied as outlined in Sect. 2.1.2 over a depth of $0.7H_p$, $1H_p$ and $1.3H_p$, which are labelled A, B and C, respectively. Fig. 4-3 shows the $^{16}\text{O}/^{17}\text{O}$

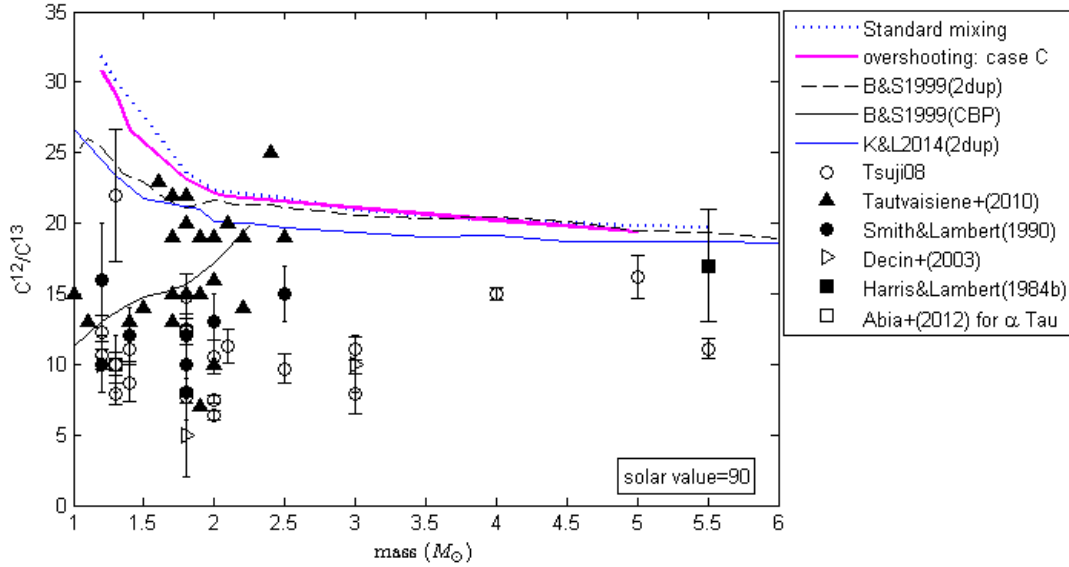


Figure 4-4: Envelope overshooting used in this study cannot explain the low observed $^{12}\text{C}/^{13}\text{C}$ ratios in low mass stars. Note that the results shown from Tautvaišiene et al. (2010) are only for stars with solar-like and near solar composition. Calculations by other groups are also shown for comparison.

ratios obtained with the three cases. We find that case C provides the best estimate of the overshooting distance in low mass stars. It is noted that overshooting only has a minor effect in stars of $M \geq 3M_{\odot}$. This is expected and can be explained in terms of the ^{17}O abundance profile in these stars shown in Figs. 4-1. The calculated and observed values for these stars are generally in a good agreement.

However, Fig. 4-4 shows that a problem arises in explaining the carbon isotopic abundances in stars of $M \leq 2M_{\odot}$, where overshooting cannot explain the low $^{12}\text{C}/^{13}\text{C}$ ratios observed in these giants. The calculation using standard mixing by Boothroyd & Sackmann (1999) and Karakas & Lattanzio (2014) show a similar problem. $^{12}\text{C}/^{13}\text{C}$ ratios close to 10 and below cannot be obtained by this model of overshooting at the base of the convective envelope with the ^{12}C profile as in Fig. 4-1. A mixing process seems to

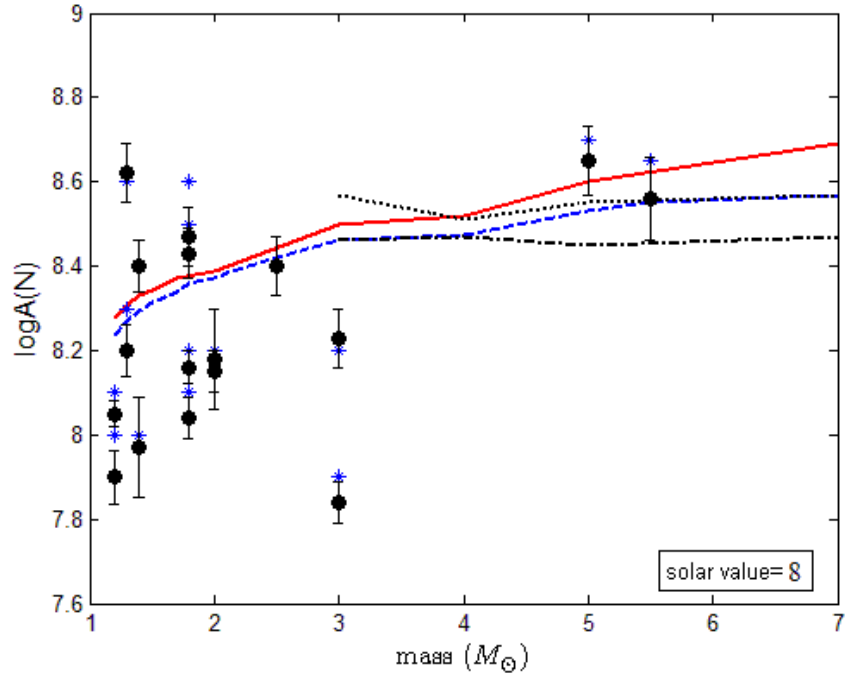


Figure 4-5: The nitrogen abundance calculated for the 21 giants. Abundances after FDUP without and with overshooting (red solid line and dashed blue line, respectively) and after SDUP without and with overshooting (black dotted and dot-dashed lines, respectively). The observational values are by Tsuji08 using two methods: standard abundance analysis (filled black circles) and the curve-of-growth (COG) method (blue astrisks) (see Tsuji08 for details).

be required in low-mass stars ($< 2M_{\odot}$) which can reduce the abundance of ^{12}C by mixing it to the hotter regions of the H-burning shell, allowing for some nuclear processing. Such mixing process is linked to the long evolutionary time of the low-mass stars while ascending the RGB. As discussed in some details in Karakas & Lattanzio (2014), the so-called “thermohaline mixing” or “salt-finger instability” seem to be one reasonable description of this extra mixing in low-mass red giant stars. Fig. 4-1 shows that this extra mixing used by Boothroyd & Sackmann (1999) and referred to as “cool bottom processing” (CBP), can explain the low $^{12}\text{C}/^{13}\text{C}$ ratios observed in low mass stars. This ratio still poses an unsolved problem in stellar modelling and remains unsettled in our models.

Fig. 4-5 shows the nitrogen abundances after FDUP and SDUP with and without overshooting. Given the scatter in the observed data, we find that, in general, our theoretical prediction reasonably reproduces the observationally inferred data for this element.

4.5 Effect of modified nuclear reaction rates

4.5.1 Effect on the $^{16}\text{O}/^{17}\text{O}$ ratio

In order to investigate the effect of proton-capture nuclear reaction rates on the $^{16}\text{O}/^{17}\text{O}$ ratios, we adopt four different evaluations of the reactions $^{16}\text{O}(p, \gamma)^{17}\text{F}$, $^{17}\text{O}(p, \gamma)^{18}\text{F}$ and $^{17}\text{O}(p, \alpha)^{14}\text{N}$ as discussed in Section 2.2.1. In particular, we study the $^{16}\text{O}/^{17}\text{O}$ ratios of the observed sample with the compilations of the ^{17}O production and destruction reactions as obtained by Sergi et al. (2014) (SE14), Sallaska et al. (2013) (SA13), Iliadis et al. (2010) (IL10) and Chafa et al. (2007) (CH07). The results are shown in Fig. 4-6 for both cases: standard mixing (left panel) and envelope overshooting (right panel). The difference between the reaction rates does not show significant variation in the $^{16}\text{O}/^{17}\text{O}$ ratios. All considered rates fail to explain observations if overshooting is not included. The more recent determinations of the rate, in particular SE14, SA13 and IL10, yield

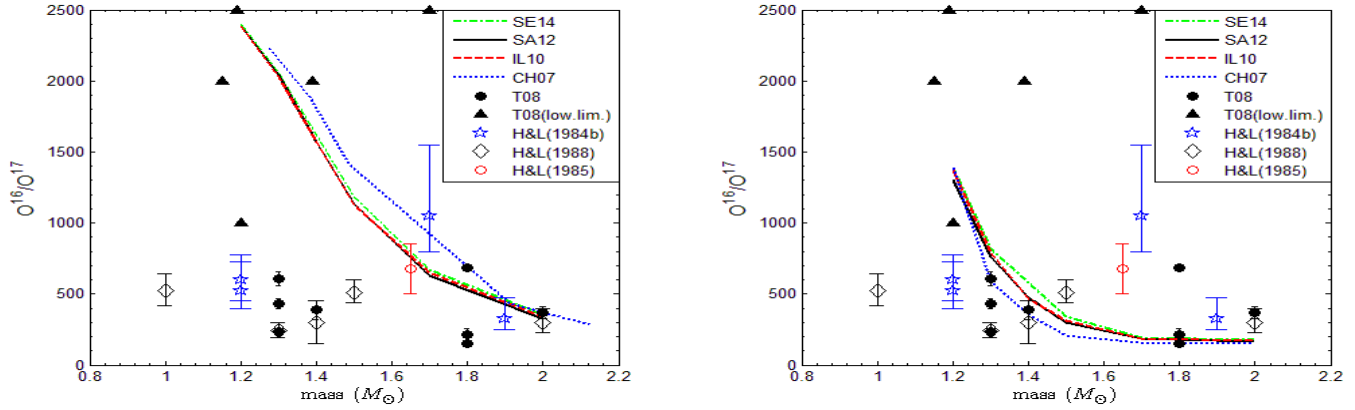


Figure 4-6: The $^{16}\text{O}/^{17}\text{O}$ ratio calculated with 4 different sets of compilations of reaction rates. Left panel shows the case with standard mixing and the right panel is that with overshooting. Several observational data are also included.

slightly higher $^{16}\text{O}/^{17}\text{O}$ ratios for stars in the mass range $1.2 - 2.5M_{\odot}$ with overshooting, which emphasizes the fact that deeper mixing is required to explain the $^{16}\text{O}/^{17}\text{O}$ ratios in these stars to achieve a better agreement with observations.

The effect of uncertainties in the reaction rates may be illustrated by exploring the variation of the resulting $^{16}\text{O}/^{17}\text{O}$ ratios. The SA13 compilation is based on a Monte Carlo simulation, and the rates have statistically well-defined uncertainties as discussed in Section 2.2.1. We investigate the $^{16}\text{O}/^{17}\text{O}$ ratios using the recommended, high and low rates, where the rate boundaries correspond to a 95% coverage probability.

It is clear from Fig. 4-7 that without overshooting (left panel), the expected range provided by the uncertainty on the rates is not sufficient to explain the observational data for low masses. When overshooting is taken into account, the observations can be better matched as shown in the right panel of Fig. 4-7. Note that in both figures, there is a scatter in the observational data. In both cases, the data points marked by filled triangles cannot be explained, which represent stars whose $^{16}\text{O}/^{17}\text{O}$ ratios are not well determined.

We also performed a separate calculation where we tried to optimize the abundance of ^{17}O in an attempt to explain the low $^{16}\text{O}/^{17}\text{O}$ observed in low-mass stars. The most

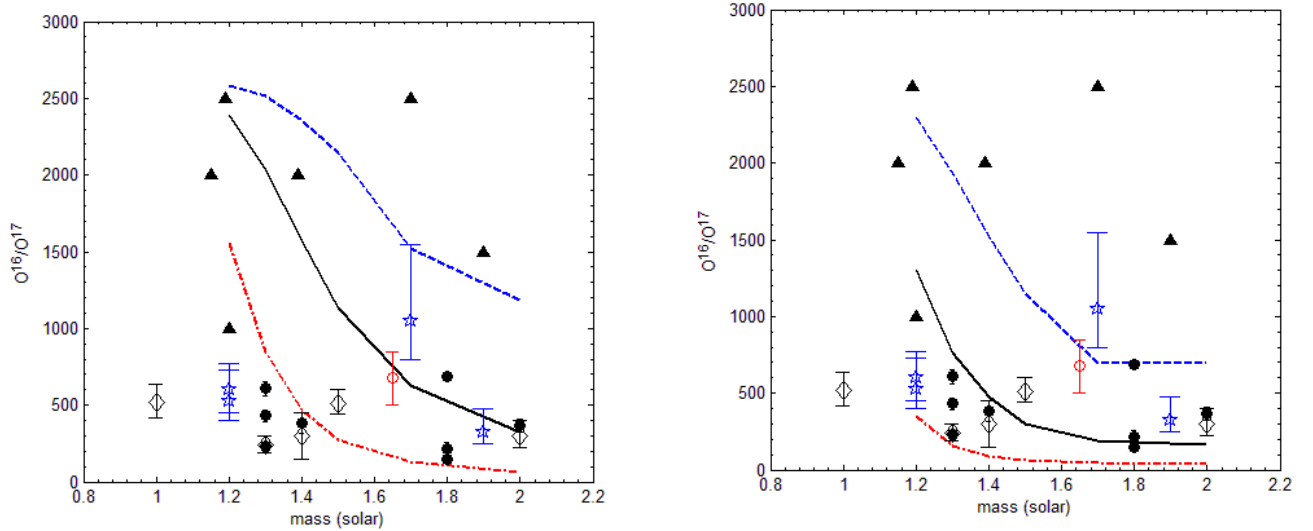


Figure 4-7: The SA13 set of rates without overshooting (left panel) and with overshooting (right panel) (see text for details). We show the median rates (solid line), their upper limits (dot-dashed) and lower limits (dashed). Observational data are the same as those in Fig. 4.6.

suitable combination to maximize ^{17}O is to use the upper rate of the ^{17}O production reaction $^{16}\text{O}(p, \gamma)^{17}\text{F}$ and the lower rates of the ^{17}O destruction reactions $^{17}\text{O}(p, \gamma)^{18}\text{F}$ and $^{17}\text{O}(p, \alpha)^{14}\text{N}$. This combination yields $^{16}\text{O}/^{17}\text{O}$ values that are very close to those obtained with the upper rates of Fig. 4-7 (left panel). We conclude that even an optimal choice of reaction rates within the suggested range of uncertainty does not fully explain the $^{16}\text{O}/^{17}\text{O}$ in low mass stars without invoking envelope overshooting.

4.5.2 Effect on the $^{14}\text{N}/^{15}\text{N}$ ratio

The $^{14}\text{N}/^{15}\text{N}$ ratio is worth considering, especially in the light of the new determination of the $^{14}\text{N}(p, \gamma)^{15}\text{O}$ rate (Adelberger et al. 2011; Halabi et al. 2012). Fig 4-8 shows the $^{14}\text{N}/^{15}\text{N}$ ratios calculated for the considered mass range after FDUP and SDUP. Our values are higher by $\sim 20\%$ than those by El Eid (1994) in stars of masses $\geq 3M_{\odot}$. This is due to the NACRE $^{14}\text{N}(p, \gamma)^{15}\text{O}$ rate used by El Eid (1994), which is almost a factor of two higher than the new rate in the relevant temperature range (see Halabi et al.

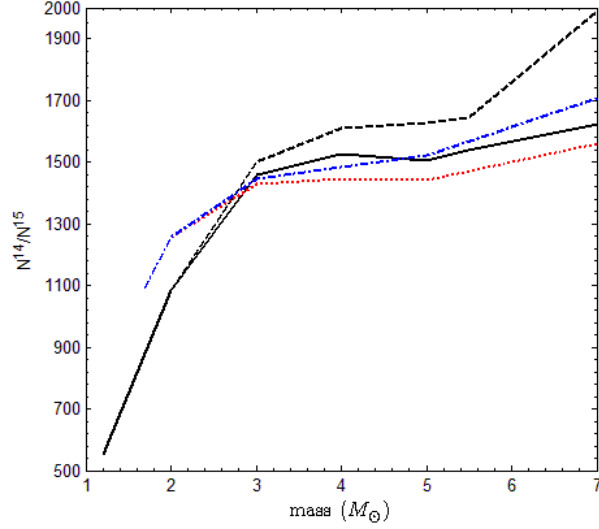


Figure 4-8: $^{14}\text{N}/^{15}\text{N}$ ratio calculated after FDUP (black solid line) and SDUP (black dashed line). The values by El Eid (1994) after FDUP (red dotted line) and SDUP (blue dot-dashed line) are included for comparison.

(2012) for the expression of the new rate and explicit discussion). This difference becomes more pronounced in higher mass stars, in the SDUP values, in particular. However, our $^{14}\text{N}/^{15}\text{N}$ is about 12% lower in the low-mass stars.

To explain this, and as discussed in Section 3.2.1, two effects of the revised rate are identified: reduced H-shell efficiency and less deep mixing on the RGB (FDUP). Therefore, we argue that in higher mass stars, the destruction of ^{14}N is less efficient with the revised rate, yielding higher $^{14}\text{N}/^{15}\text{N}$ ratios. In lower mass stars, the dominant effect of the rate is less deep mixing on the RGB, and thus the ratio is lower. For a $2M_{\odot}$ star for example, the depth of FDUP is $0.2847M_{\odot}$ and $0.2899M_{\odot}$ with NACRE and new revised rate, respectively. This explains our lower $^{14}\text{N}/^{15}\text{N}$ ratios in the lower masses.

Summing up these investigations, we conclude that studying the CNO surface abundances in red giants and comparing them with the observational values allows in principle to understand the effect of overshooting. Taking into account the experimentally suggested uncertainties on recent determinations of the reaction rates on the production

and destruction of ^{17}O , additional mixing beyond the convective envelope is found to be necessary to better explain the $^{16}\text{O}/^{17}\text{O}$ ratio observed in low mass stars. Moreover, the $^{14}\text{N}(p, \gamma)^{15}\text{O}$ rate also affects the $^{14}\text{N}/^{15}\text{N}$ ratios, particularly in IMS.

Chapter 5

Evolution & Nucleosynthesis in the AGB phase

The Asymptotic Giant Branch is an important evolutionary phase for several reasons. AGB stars are very luminous red giants, and thus can be observed in external galaxies. This makes them useful for the study of photometric properties of relatively young galaxies and the morphology of globular clusters. AGB stars are observed to have a different surface composition from their less evolved counterparts, since they constitute the site of production of about half of the heavy elements beyond iron in the Galaxy by the s-process nucleosynthesis which is discussed in some detail in Section 2.2.3, as well as light elements like carbon and fluorine.

Moreover, the pre-solar mainstream grains or Silicon-Carbide (SiC) grains, seem to originate from the carbon-rich envelopes of AGB stars, where material produced in the stellar interiors is brought to the stellar envelopes by several mixing episodes (Zinner 2005). The existing accurate measurements of the isotopic ratios in these grains provide a very informative tool to explain the evolution of AGB stars and their chemical yields. We describe the evolution along the AGB in the following section and then discuss the nucleosynthesis taking place.

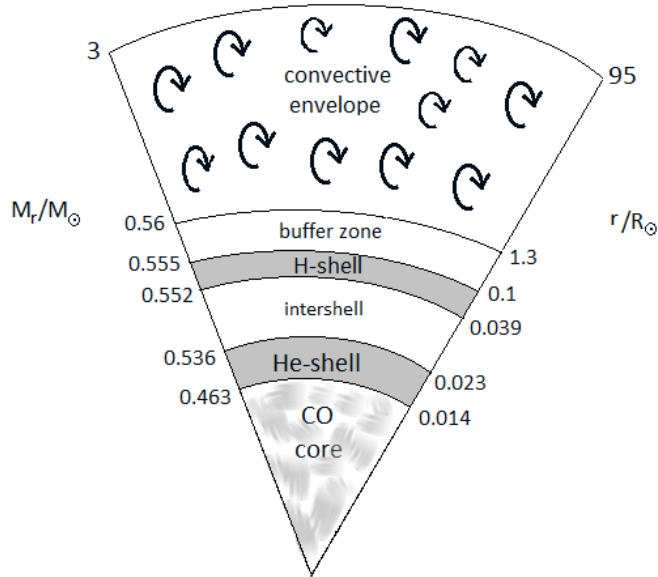


Figure 5-1: A schematic (not to scale), showing the structure of a $3M_{\odot}$ star in the E-AGB phase in the standard calculation. The coordinates of important zones are given in mass (left) and radius (right) in solar units.

5.1 Evolutionary Scenario

5.1.1 The Thermally Pulsating AGB Phase

As described in Section 1.1.3, an AGB star is characterized by its peculiar structure, namely a degenerate CO-core, a surrounding He-shell, an intershell region zone, a H-shell and a convective envelope. The structure of a $3M_{\odot}$ star in the E-AGB phase is depicted in the schematic in Fig. 5-1. The He- and H-shells are thin in mass, not comprising more than about $0.073M_{\odot}$ and $0.003M_{\odot}$, respectively. The CO core forms only about 15% of the total mass, or 0.015% of the total radius. It is noted that the active regions of this star are within about one fifth of its total mass, with the convective envelope being the largest in mass and radius.

The thermal pulsations of these stars are triggered by the He-shell burning confined

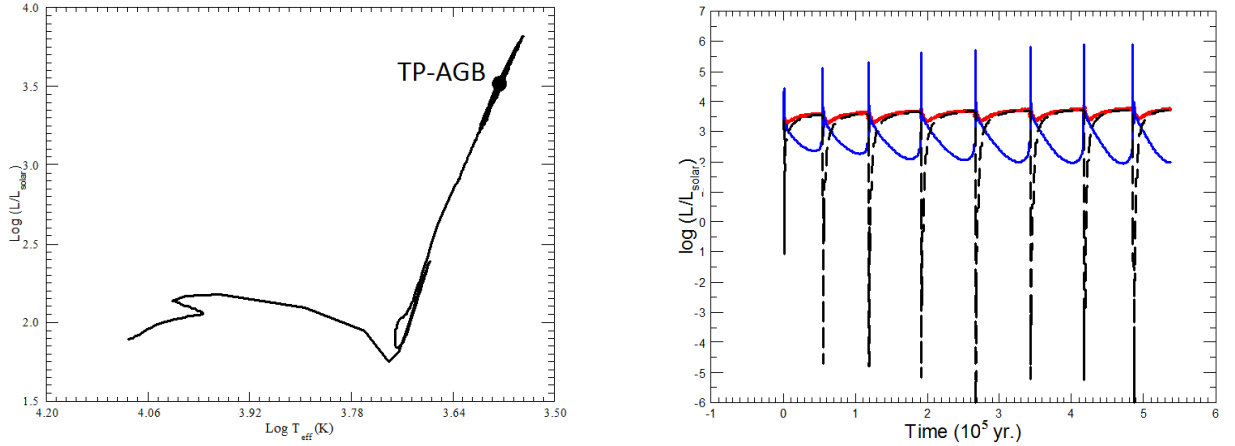


Figure 5-2: Evolutionary characteristics of a $3M_{\odot}$ star of solar-like initial composition. Left panel: Evolution in the HR diagram. Right panel: Time evolution of the stellar luminosity (thick line), helium luminosity (solid line) and hydrogen luminosity (dashed line) during the TP-AGB phase.

in a geometrically thin region. The released energy flux due to the triple- α reaction leads to recurrent thermal runaways, or pulses. It is well known that this strong energy flux during the pulse cannot be transported by radiation alone and leads to the growth of a convective instability, called *pulse driven convective zone* (PDCZ). We describe the evolution of a $3M_{\odot}$ star, of solar-like initial composition during the AGB phase and try to show the complexity involved in this type of evolution. Fig. 5-2 (left panel) shows the TP-AGB phase in the HR diagram, while in the right panel several thermal pulsations are displayed (Halabi 2012).

During these pulsations, the helium-shell and hydrogen-shell burning alternate in providing the total stellar luminosity (right panel of Fig. 5-2). To illustrate the details of this pulsation, the features characterizing one thermal pulse are shown in Fig. 5-3 and the associated convective structure is depicted in the schematic in Fig. 5-4.

In these figures, four phases of the pulse are recognized: The first is the “off phase”, during which quiescent H-burning provides the star’s luminosity and lasts for $5 - 10 \times 10^4$ years (pt. 1 in Figs. 5-3 and 5-4). The pulse (or “on phase” at pt. 2), lasts for a few 100 years, where the He-shell flash results in a luminosity peak, and a PDCZ is

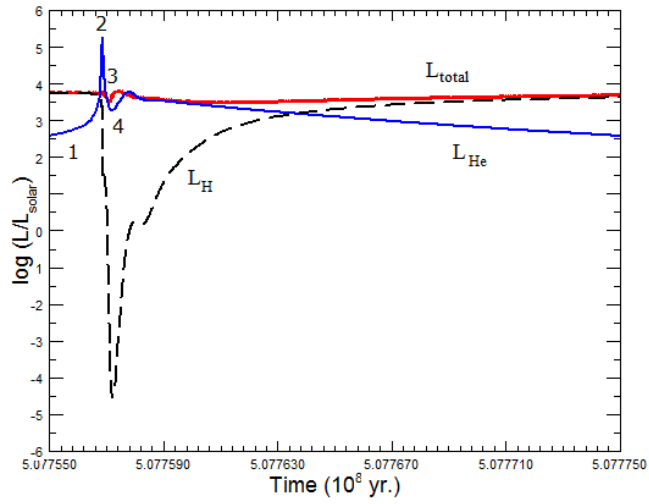


Figure 5-3: The detailed structure of a single pulse during the evolution of a $3M_{\odot}$ star. Shown are the helium shell luminosity (blue solid line), the hydrogen shell luminosity (black dashed line) and the total luminosity (red solid line). Note that the star's total luminosity remains essentially constant throughout the pulse.

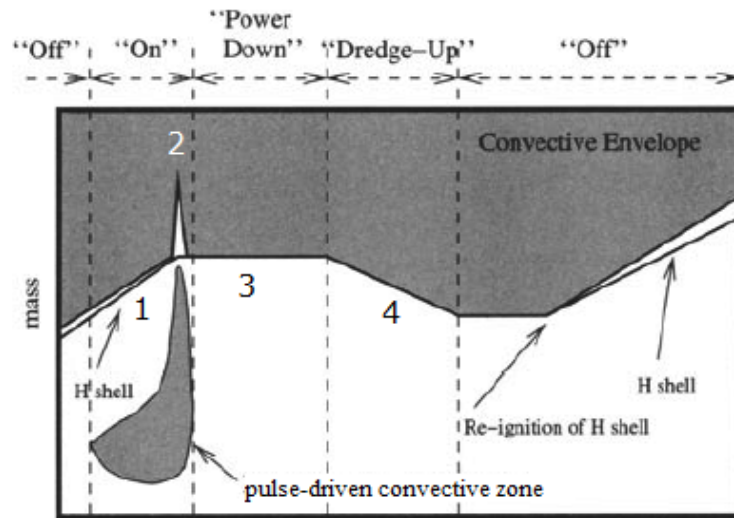


Figure 5-4: The convective structure associated with the different phases of one pulse (Lattanzio & Wood 2003).

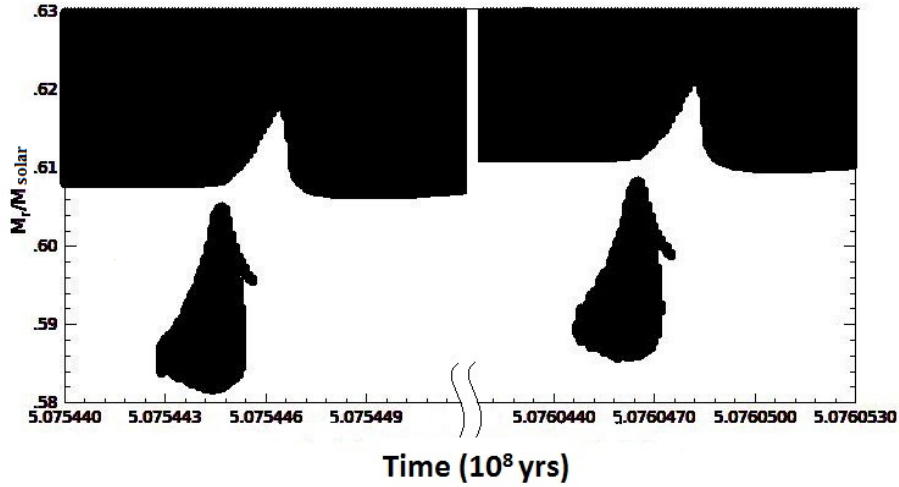


Figure 5-5: Present calculation showing the 14th and 15th thermal pulses of a $3M_{\odot}$ sequence and the associated PDCZs. Convective regions are shown in black and radiative regions in white. In order to show two pulses clearly on the same graph, the time scale between them is interrupted since the interpulse occurs at a much longer time scale compared to that of the pulse.

formed. Due to the pulse, the nuclear energy flux drives the envelope outwards, causing the temperature and density at its bottom to drop which temporarily turns off the shell hydrogen-burning (associated with the decline in L_{H} in Fig. 5-3). Owing to the expansion, the increase of opacity causes the radiative gradient to exceed the adiabatic gradient so that the convective envelope may penetrate into the carbon-rich region. This is the “power down” phase (pt. 3) leading to the third dredge up (TDUP), which corresponds to the point of minimum hydrogen and helium luminosities (pt. 4). This dredge up allows the mixing of nucleosynthesis products (carbon, fluorine and s-process elements) to the surface. At the end of the flash, contraction leads the re-ignition of hydrogen-shell burning and the convective envelope recedes.

Fig. 5-5 shows the convective structure of the 14th and 15th thermal pulses of a $3M_{\odot}$ star as obtained in our standard calculation i.e. without overshooting. It can be seen that the helium flash leads to the formation of a PDCZ. Due to the relatively

short lifetime of these pulses, high temporal and spacial resolution is required to resolve their structure. The figure shows that in this case, the envelope doesn't penetrate deep enough to the region previously occupied by the PDCZ to achieve the TDUP. Thus, extra mixing between the envelope and the He-rich zone is necessary in our calculation to obtain TDUP, and for the production of ^{13}C which is discussed below. This is in agreement with other works (Stancliffe et al. (2004) and references therein) that standard mixing alone does not produce TDUP and ^{13}C . The treatment of extra mixing varies among different works. Straniero et al. (2006) use an exponentially decaying velocity field at the bottom of the convective envelope. Gravity waves are proposed by Denissenkov & Tout (2003). Others suggest rotationally induced mixing (Langer et al. 1999) or thermohaline mixing (Charbonnel & Zahn 2007). For a recent review on extra mixing mechanisms see Karakas & Lattanzio (2014).

The extra mixing scheme outlined in Section 2.1.2 is applied, and its effect on the physical conditions of TDUP is discussed in the following section.

5.1.2 Exploring Third Dredge Up

One observational evidence that TDUP occurs in AGB stars is the existence of carbon stars in the Magellanic Clouds (Richer et al. 1979; Guandalini et al. 2004; Abia et al. 2008), where the carbon abundance exceeds that of oxygen. This shows that the envelope penetrates into the carbon-rich region and mixes carbon to the surface by recurrent TDUP episodes. Within some uncertainties, it is estimated that about one third of the Galaxy's inventory of ^{12}C is produced in AGB stars (Lattanzio & Wood 2003).

We find that a possible choice to obtain TDUP is by taking an overshooting distance of $1.2H_p$ at the bottom of the convective envelope and $0.1H_p$ at the boundaries of the PDCZ. This is shown in Fig 5-6, which depicts the 8th pulse in the $3M_\odot$ sequence calculated with this overshooting. It is clear that overshooting at the bottom of the convective envelope causes the H-rich envelope to reach the region previously processed by the PDCZ, which leads to the ingestion of protons into the C-rich zone to produce the

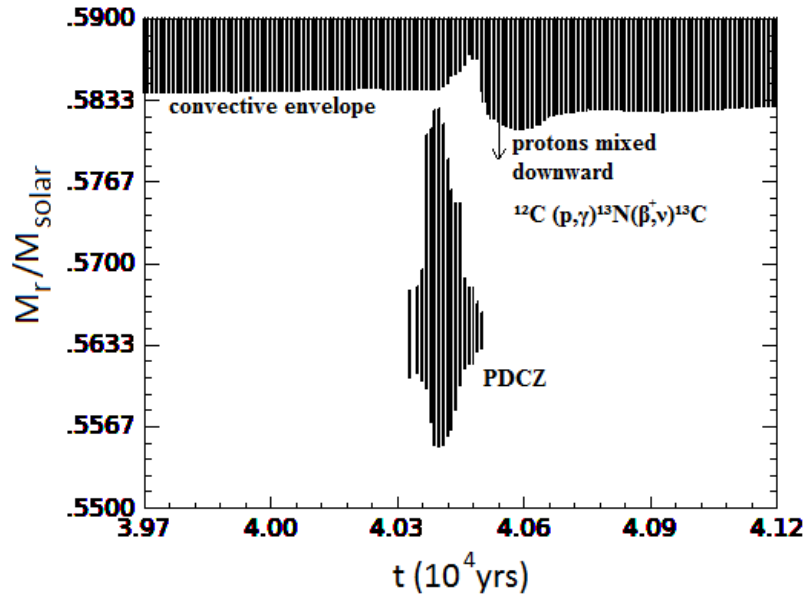


Figure 5-6: The 8th pulse of a $3M_{\odot}$ sequence calculated when overshooting is applied at all convective boundaries (see text for details). The time has been reset at the onset of the previous pulse. The H-shell burns just below the convective envelope. TDUP operates at the end of the pulse, before the H-shell gets re-activated, and produces a ^{13}C pocket which is the neutron source for the *s*-process. The protons are mixed downward a depth of a few $10^{-4}M_{\odot}$, and the PDCZ is up to a few $10^{-2} M_{\odot}$ in mass.

amount of ^{13}C necessary for s-process nucleosynthesis as discussed in Section 2.2.3. An interesting feature concerning TDUP is that it only occurs when the hydrogen shell is temporarily extinguished (pulse power-down phase) (Figs. 5-3 and 5-4). In fact, as the pulse progresses, the produced energy flux forces matter above it to expand outward and cool, leading to pulse power-down and a decline in shell entropy, which makes TDUP possible (Iben & Renzini 1984). The efficiency of this dredge-up is parametrized by $\lambda = \Delta M_{DUP}/\Delta M_H$, where ΔM_{DUP} is the mass dredged-up in one thermal pulse, and ΔM_H is the amount by which the H-free core grows in the preceding interpulse.

The thermal pulsations characterizing the AGB phase are the site of nucleosynthesis of heavy elements through the s-process. The production of ^{13}C required for this process is described in the next section.

5.2 Nucleosynthesis in the AGB phase

5.2.1 Formation of the ^{13}C pocket

The ^{13}C produced in the intershell by CNO burning is insufficient to lead to the neutron source required for the s-process. Thus, as described previously, TDUP is necessary to mix protons downwards to a C-rich region where the temperature is high enough to activate the reaction chain $^{12}\text{C}(p,\gamma)^{13}\text{N}(\beta^+,\nu)^{13}\text{C}(\alpha,n)^{16}\text{O}$ so that neutrons are released during the phase that follows TDUP. This is maintained until the H burning shell is re-ignited (see Fig. 5-4). Fig. 5-7 shows the evolution of the ^{13}C pocket after the 8th thermal pulse. The different panels display several isotopes at different times after the pulse. It is evident that after the maximum penetration of the convective envelope, the H and C profiles merge to produce a small ^{13}C pocket underneath a ^{14}N -rich layer, about 3170 years after the pulse in this specific model. The ^{13}C and ^{14}N pockets are overlapping. As the interpulse phase progresses, the ^{13}C abundance profile becomes broader with a lower peak. ^{13}C burns in radiative conditions, in agreement with Straniero et al. (1995; 1997).

Several characteristics of 9 pulses of the $3M_{\odot}$ sequence are listed in Table 5.1, including

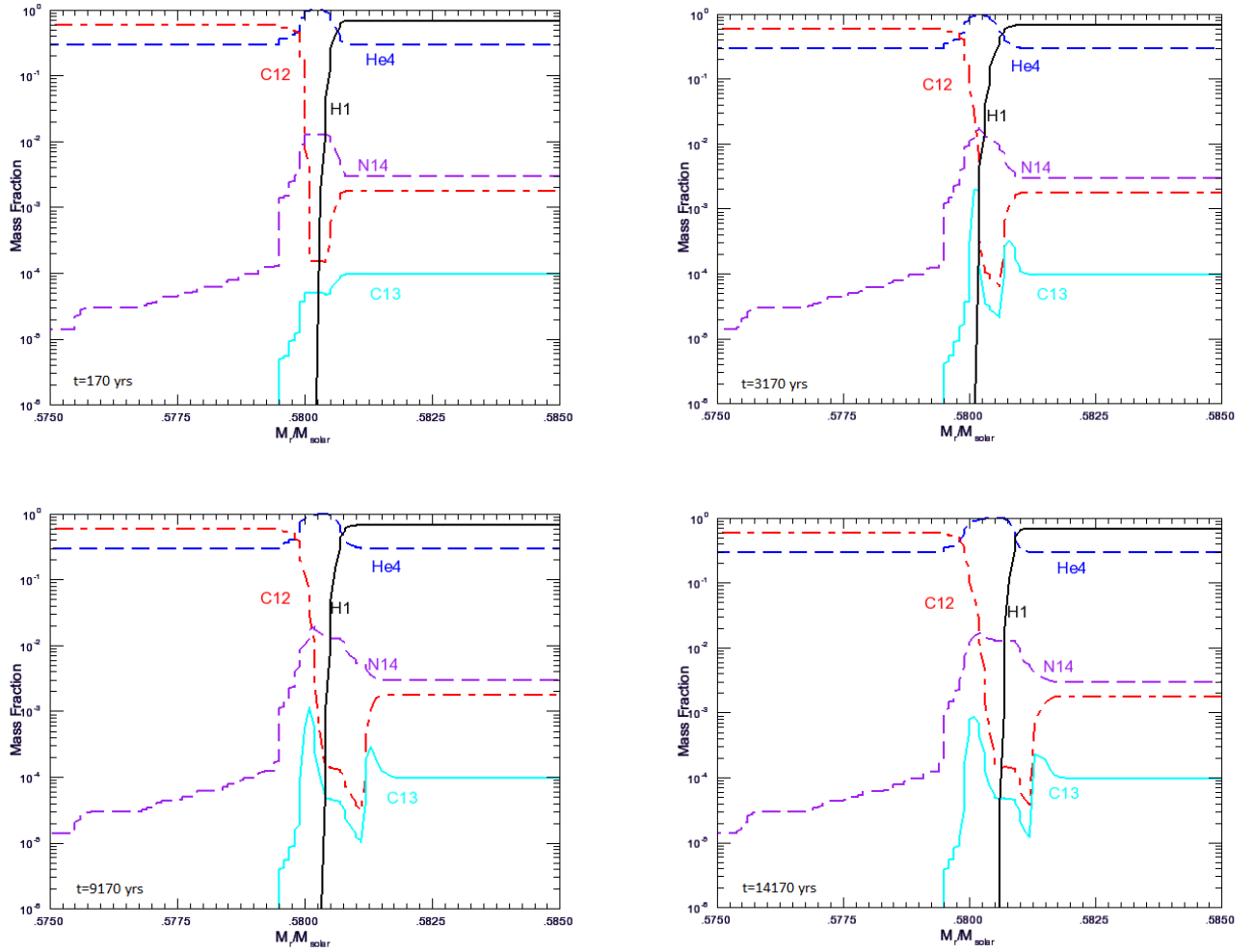


Figure 5-7: The panels show the abundance profiles of the core-envelope transition zone, particularly, the region where the ^{13}C pocket is formed in a $3M_{\odot}$ sequence at different times following the 8th thermal pulse as indicated. Time is set to zero at the onset of the pulse. Overshooting is applied at all convective boundaries (see text).

the results by Stancliffe et al. (2004) and Straniero et al. (1997) for comparison. We compare to Straniero et al. (1997) values that are calculated with mass-loss, where they use Reimers mass-loss rate with $\eta = 1$, similar to our treatment (see Section 2.1.1). By inspecting the table, several points can be made:

1. The H-free core (M_{H}) shown in the first column increases as pulsations proceed. This is expected due to the activity of the H-shell, where hydrogen burns into helium and causes the underlying core to increase in mass.
2. A close agreement can be seen in M_{H} and C/O ratios with Stancliffe et al. (2004) and Straniero et al. (1997).
3. The values of maximum luminosity by He-shell burning ($L_{\text{He}}^{\text{max}}/L_{\odot}$) are rather comparable during the first few pulses but the difference becomes pronounced in the later pulses, where our values of $L_{\text{He}}^{\text{max}}/L_{\odot}$ are lower and the interpulse periods are shorter and become constant during the last pulses. A lacking of general agreement is noticed among all three calculations related to these two quantities. This is due to the complex behavior during this phase and its dependence on the efficiency of burning and the treatment of mass-loss, and thus is more sensitive to model calculation than the other quantities. Their higher He-luminosities may explain their longer interpulse periods compared to our values. In fact, a higher He-luminosity means a more violent He-flash, which pushes the hydrogen shell further out in mass and thus it takes longer to establish H-shell burning.
4. The slightly higher M_{H} of Stancliffe et al. (2004) at the 7th pulse explains the earlier occurrence of TDUP in their case (at the 7th pulse, as compared to the 8th pulse in our case). This is consistent with their finding that TDUP occurs when M_{H} exceeds $0.584M_{\odot}$, which is almost attained at our 8th pulse when TDUP occurs.
5. Straniero et al. (1997) find that TDUP occurs at the 8th pulse, like our case, but at a higher core mass (of $0.611M_{\odot}$).

Table 5.1: Selected details of the pulsations of the $3M_{\odot}$ compared to the values by Stancliffe et al. (2004) and Straniero et al. (1997) as shown in parathensis, respectively, in a seperate row. The quantities shown in the columns are respectively: thermal pulse number, mass of the hydrogen-free core, interpulse period (time between two consecutive pulses), the peak of helium luminosity (scaled to L_{\odot}), dredge-up paramter and the surface carbon-to-oxygen ratio.

TP	$M_{\text{H}} (M_{\odot})$	$\tau_{\text{IP}} (10^4 \text{ yrs})$	$\log(L_{\text{He}}^{\text{max}}/L_{\odot})$	λ	C/O
1	0.565 (0.565, 0.572)	– –	4.48 (4.36, 6.08)	– –	0.32 (0.319, 0.317)
2	0.566 (0.566, 0.573)	4.2 (4.29, 7.24)	5.20 (4.83, 4.39)	– –	0.32 (0.319, 0.317)
3	0.567 (0.567, 0.579)	4.6 (5.80, 9.30)	5.25 (5.41, 6.55)	– –	0.32 (0.319, 0.317)
4	0.569 (0.570, 0.584)	4.9 (7.77, 11.0)	5.64 (6.09, 6.36)	– –	0.32 (0.319, 0.316)
5	0.571 (0.574, 0.591)	5.6 (8.87, 10.4)	5.94 (6.43, 6.69)	– –	0.32 (0.319, 0.316)
6	0.574 (0.579, 0.597)	5.8 (9.17, 10.1)	5.96 (6.72, 6.81)	– –	0.32 (0.319, 0.316)
7	0.577 (0.584, 0.604)	5.8 (9.02, 9.44)	5.98 (6.88, 6.91)	– (0.154, –)	0.32 (0.329, 0.316)
8	0.580 (0.589, 0.611)	5.8 (8.80, 8.87)	5.99 (7.09, 7.01)	0.44 (0.350, 0.014)	0.328 (0.369, 0.316)
9	0.583 (0.593, 0.618)	5.5 (8.78, 8.33)	6.13 (7.33, 7.11)	0.45 (0.514, 0.071)	0.33 (0.439, 0.322)

Table 5.2: Selected properties of the 8th thermal pulse and the ¹³C pocket as compared to those by Lugaro et al. (2003). The shown quantities are: the duration of the PDCZ, interpulse period and TDUP, the duration of the formation of ¹³C pocket from the onset of the pulse and the mass of the pocket.

	τ_{PDCZ} (yrs)	τ_{IP} (10 ³ yrs)	τ_{TDUP} (yrs)	$\tau_{^{13}\text{C}}$ (10 ³ yrs)	$M(^{13}\text{C})$ (M_{\odot})
This work	240	58	180	2.76	10^{-5}
Lugaro et al. (2003)	40	52	160	2.5	3.7×10^{-5}

After a sufficient number of TDUP episodes C/O increases and eventually exceeds unity, which indicates the formation of a carbon star as mentioned earlier.

In Table 5.2 we present several properties of the thermal pulses and the resulting ¹³C pocket, and compare the values to those by Lugaro et al. (2003). The values are in general agreement except for the duration of the PDCZ. Our calculation shows a duration of 240 yrs, while their PDCZ lasts for about 40 yrs. To investigate this discrepancy, we note that according to Lattanzio & Wood (2003), the PDCZ lasts for a few hundred years and is highly dependent on the core mass. At the onset of TDUP, our core mass is about 0.58 M_{\odot} , while Lugaro et al. (2003) report a core mass of about 0.6 M_{\odot} . This may explain this discrepancy. Stancliffe et al. (2004) who find that the PDCZ typically lasts for about 20 yrs also report a bigger core at the beginning of TDUP ($M_{\text{H}} = 0.584M_{\odot}$, see Table 5.1). On the other hand, Straniero et al. (2005) find that the PDCZ in a 2 M_{\odot} star lasts about 400 yrs (see their Fig. 3). This indicates that this duration is highly dependant on the stellar mass and on the details of modeling this phase.

This discussion shows that the amount of ¹³C produced by proton ingestion into the C-rich region is still difficult to determine in AGB nucleosynthesis calculations. During the interpulse period, ¹³C must be available in order to produce a neutron density of about 10⁸ cm⁻³ for an effective s-process, which is discussed next.

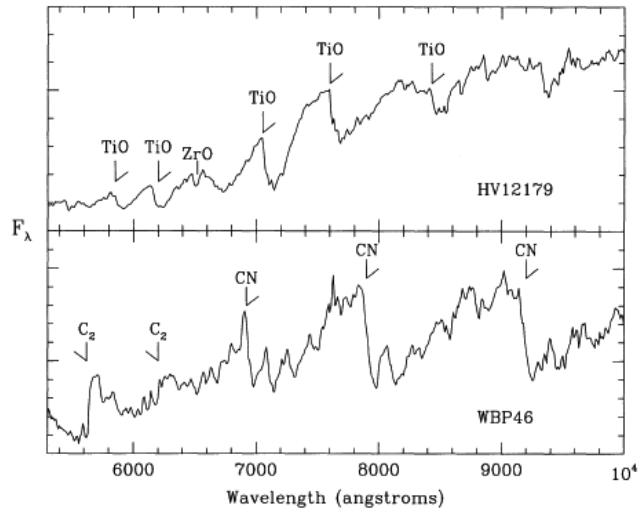


Figure 5-8: Spectra of stars in the Large Magellanic Cloud with some of the strongest molecular bands identified (Lattanzio & Wood 2003).

5.2.2 *s*-process nucleosynthesis

A peculiarity of the spectra of AGB stars is the observation of enhanced bands of molecules involving *s*-process elements like Sr, Y, Zr, Ba, La, Ce and Nd (Smith & Lambert 1990). A prominent example is the observation of the molecular bands TiO and ZrO in their stellar spectra as shown in Fig. 5-8, which clearly indicates an *s*-process signature.

Since *s*-process elements are produced in regions of the star where $T \approx 10^8 \text{K}$ (which is required to activate the neutron source), the existence of these enhancements indicates that *s*-processed material from deep in the star has been brought to the stellar surface by TDUP. Another interesting example is the observation of ^{99}Tc (technetium) absorption lines in AGB stars (see for example Lambert 1989). This observation was first announced by P. W. Merrill in 1952 (Merrill 1952a,b). ^{99}Tc has no stable isotopes and a half-life of $\approx 2 \times 10^5$ years which is clearly shorter than the lifetime of a thermally pulsating AGB star. Thus, the detected ^{99}Tc must have been produced in situ and brought to the stellar surface of these stars in the last few 10^5 years. The presence of stellar ^{99}Tc was a direct

evidence that heavy-element formation indeed occurs inside stars, which prompted new theories of nucleosynthesis to explain this formation since Merrill's work. Since ^{99}Tc is an element that can only be formed through the s-process, this is a direct observational evidence that the s-process happens in AGB stars. During the subsequent planetary nebulae phase of evolution, s-process elements are ejected into the interstellar medium.

Early considerations adopted the view that the neutron source of the s-process is $^{22}\text{Ne}(\alpha, n)^{25}\text{Mg}$, where the ^{22}Ne is synthesized in the ^{14}N -rich intershell region, by the CNO cycle via the reaction chain $^{14}\text{N}(\alpha, \gamma)^{18}\text{F}(\beta^+, \nu)^{18}\text{O}(\alpha, \gamma)^{22}\text{Ne}$. But this assumes relatively high temperature $T \geq 3 \times 10^8 \text{K}$ to enable the $^{22}\text{Ne}(\alpha, n)^{25}\text{Mg}$ reaction. However, observations revealed that most s-process enhanced stars were low-mass stars, and the search for enhancement of ^{25}Mg indicating the operation of $^{22}\text{Ne}(\alpha, n)^{25}\text{Mg}$ was negative (Smith & Lambert 1986).

An alternative source that was suggested is $^{13}\text{C}(\alpha, n)^{16}\text{O}$ which requires small temperatures close to 10^8K . The right amount of ^{13}C should be produced to achieve neutron densities of the order of 10^7 - 10^8cm^{-3} , as required for the effective operation of the s-process nucleosynthesis.

It is important to note that not too many protons are mixed by TDUP, otherwise, the CN cycle continues by proton captures on ^{13}C producing ^{14}N , which known as the ^{13}C poison. If, on the other hand, few protons are mixed, the ^{13}C source is not enough to produce a sufficient amount of neutrons to operate the s-process. Given the right neutron density, the s-process occurs between pulses and the produced s-elements are then engulfed by the subsequent pulse and brought to the surface during the next TDUP event, where they are observed.

In order to perform s-process calculations, a full network of nuclear reactions including all relevant isotopes up to the termination point of the s-process (Pb–Bi) is needed. Such a network is available (Meyer (2012), <http://sourceforge.net/projects/nucnet-tools>) and major work has been done to integrate it into the stellar code. This network may include up to 750 nuclei, and needs fast computer facilities. We are working intensively with B.

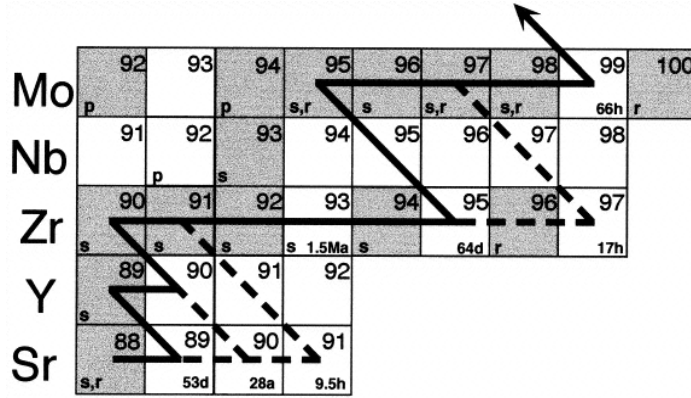


Figure 5-9: The s-process path through the Zr, Nb and Mo isotopes. Notice that there are two unstable Zr isotopes: long-lived ^{93}Zr and short-lived ^{95}Zr . Thick lines show the main path of the s-process, while the thinner lines show the less important branchings (Nicolussi et al. 1998).

Meyer (Clemson Univ., SC, USA) to make this involved calculation possible. This is an ongoing work which will be continued in a project approved by the Lebanese National Council of Scientific Research (CNRSL) as discussed in the last section of Chapter 7.

To appreciate the physical significance of the s-process, we describe an interesting aspect concerning the branching along the s-process path. These occur when the β -decay lifetime becomes comparable to that of the neutron-capture. An example is the branching along the chain of Zr isotopes shown in Fig. 5-9. Following the neutron-capture path along the Zr-isotopes, two unstable isotopes are encountered: ^{93}Zr with half-life of 1.5 Myr and ^{95}Zr with half-life of 64 days only. In order to reach ^{96}Zr , a high neutron density is required (in excess of 10^8 neutrons/cm³) to enable this branching through the unstable short-lived isotope ^{95}Zr to ^{96}Zr (Lugaro et al. 2014). However, this cannot be supplied by the $^{13}\text{C}(\alpha,n)^{16}\text{O}$ reaction, but through the activation of $^{22}\text{Ne}(\alpha,n)^{25}\text{Mg}$. The latter reaction needs higher temperature, in excess of $3 \times 10^8 \text{K}$.

It is indeed a complex process given that the accurate analysis of the pre-solar silicon carbide grains, which are believed to originate from the C-rich envelopes of relatively low-mass AGB stars ($\leq 3M_{\odot}$), indicates subsolar ratios of $^{96}\text{Zr}/^{94}\text{Zr}$ (Lugaro et al. 2014).

In this case, extra-mixing at the bottom of the PDCZ seems necessary to activate the $^{22}\text{Ne}(\alpha, n)^{25}\text{Mg}$ neutron source (Herwig 2005), leading to high neutron densities in excess of 10^8 neutron/cm³ to enable this kind of branching.

To conclude, comparing the theoretical predictions of s-process nucleosynthesis with abundances inferred from AGB stars observed in the galactic disk for example can set constraints on the amount of ^{13}C and the degree of extra mixing. The chemical analysis of isotopic compositions of presolar SiC grains found in meteorites (Zinner 2005, Lugaro et al. 2014) can provide further confirmations on the nucleosynthesis yields of the s-process. However, observations show a significant scatter of s-process abundances at all metallicities (Busso et al. 2001). Moreover, recent studies show that AGB models predict large overabundance of lead (Pb) compared to other s-process elements in metal-poor low-mass AGB stars when compared to spectral abundance analysis of the post-AGB stars in the SMC and LMC (De Smedt et al. 2014). With the standard ^{13}C pocket, models predict a Pb abundance about 20 times higher than the upper limit of its observationally inferred value, which suggests that the ^{13}C source has to be smaller in mass than what current models predict (not more than $10^{-4}M_{\odot}$). This introduces the possibility that the size of the ^{13}C pocket may be different depending on stellar parameters such as the initial mass, metallicity, or mass-loss rate, or simply due to the still unclear nature of the proton-ingestion process into the He intershell region. This remains an open question up to this date.

Chapter 6

Evolution & Nucleosynthesis in the SAGB Phase

Stars in the mass range $8 \lesssim M/M_{\odot} \lesssim 12$ are among the most numerous massive stars in the Galaxy (Jones et al. 2013). They ignite carbon in their cores and evolve to the Super-AGB phase. After carbon burning, these stars develop oxygen-neon (ONe) cores. Two evolutionary scenarios are possible at this point: either the cores evolve into ONe white dwarfs (WDs) or they explode as electron capture supernovae (EC-SNe) if they have high enough central densities.

The minimum initial stellar mass that is able to ignite carbon in hydrostatic conditions is commonly referred to as M_{up} , whose value differs among different works. For stars of solar initial metallicity, $M_{\text{up}} \sim (6-9)M_{\odot}$ (Becker & Iben 1979, 1980; Bertelli et al. 1985; Maeder & Meynet 1989; Bressan et al. 1993; Garcia-Berro et al. 1997; Umeda & Nomoto 1999; Bono et al. 2000). Stars less massive than M_{up} develop electron degenerate cores consisting of the ashes of He-burning, essentially carbon and oxygen, and eventually become CO WDs. Stars of $M \geq M_{\text{up}}$ ignite carbon in a partially degenerate CO core and form electron degenerate ONe cores.

This critical mass is crucially dependent on the efficiency of the $^{12}\text{C}+^{12}\text{C}$ fusion reaction rate with its two possible α and p-channels as outlined in Section 2.2.2. A new

determination of M_{up} is important for the theory of novae outbursts, as well as for the evolution towards SN type Ia.

We will focus in the following on studying the effect of the $^{12}\text{C}+^{12}\text{C}$ reaction as well as overshooting and mass-loss on M_{up} . It is noted that M_{up} is also affected by other factors like metallicity, rotation and binarity. Multi-dimensional simulations can also possibly yield different values. In what follows, we describe the evolution of a $9M_{\odot}$ star as a representative of this mass range and compare with the calculation available by other works.

6.1 Evolution of a $9M_{\odot}$ star

The evolution of a $9M_{\odot}$ star of solar-like initial composition is calculated from the main sequence till the thermally pulsating SAGB phase. Fig. 6-1 shows the characteristics of this evolution in the HR diagram and displays the time evolution of the internal structure. The following phases can be identified:

- a. Core H-burning (A-B) in a convective core.
- b. Shell H-burning (starting at position C) and subsequent evolution to the RGB, where a convective envelope is formed (see right panel).
- c. Core He ignition (position E) in a convective core.
- d. Formation of an extended blue loop (F-G) described in Chapter 3.
- e. End of core He-burning (position H) but no SDUP due to the effective H-shell burning (dashed line in right panel).
- f. Carbon ignition (position I) when the temperature is high enough and the region becomes convective. We elaborate on this burning phase in the next section.

Table 6.1 shows several physical properties for this sequence and the results by other works for comparison. We find a significant discrepancy with GB97 in the He burning

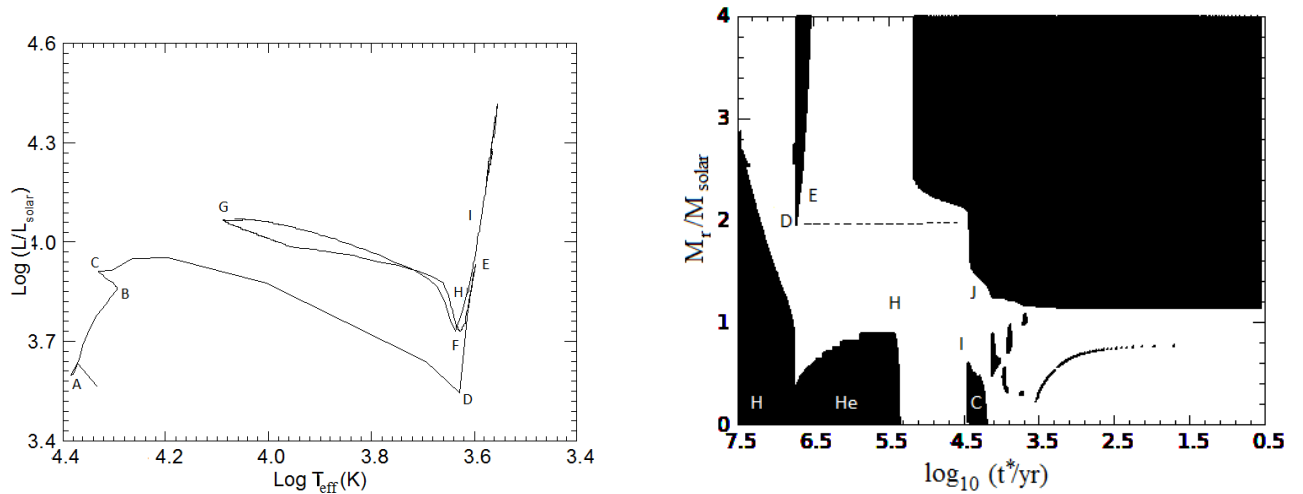


Figure 6-1: Left panel: Evolutionary track in the HR diagram of the $9M_{\odot}$ sequence. Labeled phases are described in text. Right panel: Evolution of the convective structure during the H-, He- and C-burning phases. The thin dashed line marks the position of the H-burning shell. Labels are the same as those in left panel. t^* is the time left until the end of calculation in years, i.e. $t^*=t_f-t$.

Table 6.1: Characteristics of this sequence at the end of He-burning. L and R are in solar units. Results by Garcia-Berro et al. (1997) (GB97) and Siess (2006) (S2006) are provided for comparison.

Model	$t(10^7\text{yrs})$	$\Delta t_H(10^7\text{yrs})$	$\Delta t_{He}(10^7\text{yrs})$	$\log L$	$\log T_{eff}$	$\log R$
This work	2.83	2.32	0.51	4.18	3.57	2.46
GB97	2.39	2.26	0.13	4.28	3.57	2.53
S2006	2.84	2.36	0.48	—	—	—

lifetime. We attribute this to the difference in the input physics. In particular, during core H- and He-burning, they use nuclear reaction rates which date back to Caughlan & Fowler (1964) and Fowler & Hoyle (1964). It is thus conceivable that the main reason for the discrepancy found in the He burning lifetime originates from their adopted nuclear rates.

Fig. 6-2 shows the abundance profiles of the important nuclear species and the temperature profile at the end of the core He-burning. It is seen that the CO core has a mass $M=0.94M_{\odot}$ and the H-free core is $2M_{\odot}$. Note that the temperature gradient is much

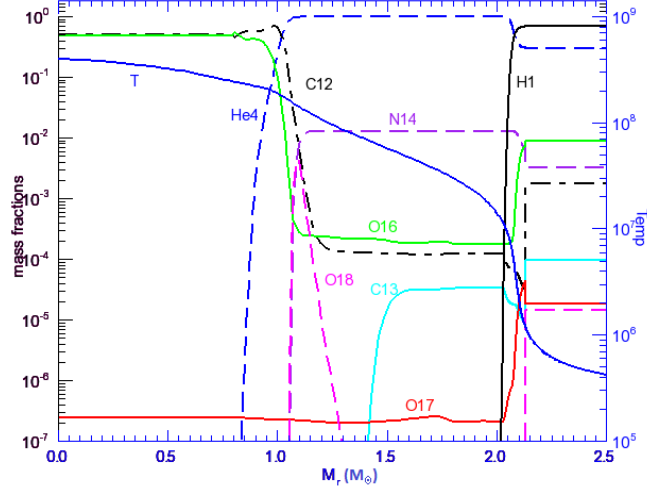


Figure 6-2: Mass fractions of the major isotopes and the temperature profile at the end of He-burning. The mass is in solar units (M_{\odot}).

Table 6.2: Characteristics of the core and the central mass fractions of the major isotopes at the end of He-burning.

Model	$\log \rho_c$	$\log T_c$	$M_{CO}(M_{\odot})$	$X_c(^{12}C)$	$X_c(^{16}O)$	C/O
This work	5.9	8.8	0.994	0.384	0.513	0.75
GB97	6.5	8.62	1.068	0.32	0.65	0.49
S2006	—	—	1.053	0.337	0.637	0.52

steeper near the edge of the H-free core than near the edge of the CO-core.

Several physical properties are shown in Table 6.2 at the end of the core He-burning. Close agreement is obtained with other works in the central temperature and density and in the mass of CO core. However, we find different values for the mass fractions of central ^{12}C and ^{16}O , or the ratio of C/O. This is due to the different $^{12}C(\alpha, \gamma)^{16}O$ reaction rate used, which becomes the dominant nuclear energy production source near central helium exhaustion and determines the C/O ratio at the end of He-burning. The rate is obviously higher in the other works.

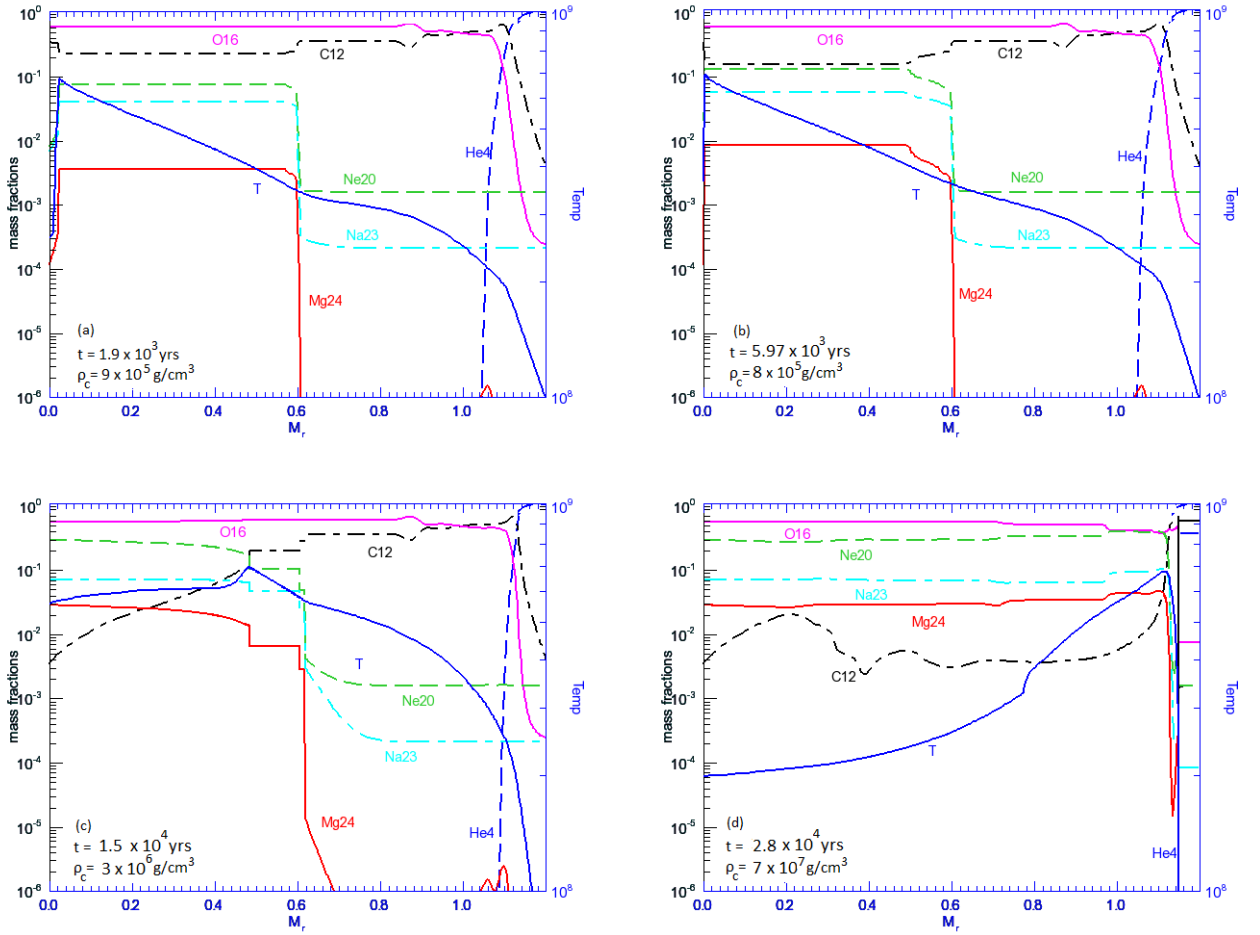


Figure 6-3: The abundance profiles of major isotopes at different times after the ignition of carbon-burning as indicated. The value of the central density is also shown in each panel.

6.1.1 The carbon-burning phase

In the following, we describe the evolution of the $9M_{\odot}$ model through the carbon-burning phase. Our aim is to investigate the effect of the new $^{12}\text{C}+^{12}\text{C}$ reaction rate being subject to experimental uncertainties. First, we use the CR rate described in Section 2.2.2. The results obtained are displayed in Fig. 6-3. Several conclusions can be drawn on the basis of this rate.

- a. Carbon ignites very close to the center, at mass shell $\sim 0.07M_{\odot}$. This is due to

neutrino losses (mainly plasma neutrinos) in the central region where the density is high, leading to the temperature inversion as seen in Fig. 6-3a.

- b. Carbon ignition proceeds at $T \sim 7 \times 10^8 \text{K}$ in a convective core of $M = 0.6M_{\odot}$ (see convective structure in Fig. 6-1). The main products of C-burning are ^{20}Ne , ^{23}Na and ^{24}Mg , while the abundant ^{16}O is the product of the previous He-burning phase.
- c. Towards the end of C-burning, the convective core decreases in mass. The high central density (Fig. 6-3c) leads to higher neutrino energy loss, which overcomes the nuclear energy generation rate. This prohibits convection in the core and causes a temperature inversion. As a consequence, carbon is not completely exhausted and central C-burning ends radiatively, which explains the resulting nonhomogeneous carbon profile (see Fig. 6-3d). After central C-burning, shell C-burning proceeds in convective zones surrounding the core. This can be seen in the homogenized profiles in Fig. 6-3c at $M_r = 0.5\text{-}0.6M_{\odot}$ in connection with the convective structure in Fig. 6-1.

At the end of the C-burning phase, the electron-degenerate helium-exhausted core consists of an inner part of mass $M_{\text{ONe}} \sim 1.122M_{\odot}$, in which the dominant isotopes are ^{16}O , ^{20}Ne and ^{23}Na , surrounded by a carbon-oxygen rich layer of mass $\Delta M_{\text{CO}} \sim 0.025M_{\odot}$, in which ^{20}Ne is far less abundant than ^{12}C . The mass of the He-exhausted core, or CO core is $M_{\text{CO}} = 1.147M_{\odot}$. In the ONe core, there is residual carbon whose maximum mass fraction is ~ 0.021 , at mass shell $M_r = 0.215M_{\odot}$. This remaining C-profile may be important for the study of novae eruptions. Another possibility is if the star is in a binary system and accretes enough mass to reach the Chandrasekhar limit, this remaining carbon would ignite, which in turn ignites oxygen, causing a thermonuclear disruption (GB97). Gutiérrez et al. (2005) show that this disruption can be induced by traces of carbon as low as 0.015. Core properties and mass fractions of the major central abundances at the end of C-burning (Figure 6-3d) are summarized in Table 6.3.

Table 6.3: Core properties and central mass fractions of the major isotopes at the end of carbon-burning. The quantities shown are respectively: the mass of the ONe core, the mass of the CO shell and the He-free core, the maximum mass fraction of ^{12}C (residual carbon) and its position, central mass fractions of important isotopes and ^1H and ^4He mass fractions in the buffer zone on top of the H-exhausted core. Masses are in solar units.

M_{ONe}	ΔM_{CO}	M_{CO}	X_{12}^{max}	$M_r(X_{12}^{\text{max}})$	$^{12}\text{C}_c$
1.122	0.025	1.147	0.021	0.215	0.0035
^{24}Mg	$^{16}\text{O}_c$	$^{20}\text{Ne}_c$	$^{23}\text{Na}_c$	$^4\text{He}_{\text{top}}$	$^1\text{H}_{\text{top}}$
0.029	0.57	0.299	0.0725	0.383	0.6

We also investigated the C-burning phase of the $9M_{\odot}$ star using the CF88 rate (Caughlan & Fowler 1988) described in Section 2.2.2. In this case, the convective structure is shown in Fig. 6-4, while the abundance profiles of major isotopes and the temperature profile at different times during carbon-burning are shown in Fig. 6-5. The results are summarized as follows.

- a. Carbon ignites remarkably off-center at a convective mass shell $\sim 0.23M_{\odot}$ (Figure 6-4). This is again due to neutrino energy losses in the central region leading to a temperature inversion near the center (Fig. 6-5a).
- b. Carbon ignition occurs at $T \sim 7 \times 10^8 \text{K}$ mainly producing ^{20}Ne , ^{23}Na and ^{24}Mg .
- c. The large energy production due to the sensitivity of the carbon fusion rate to temperature, coupled to the degeneracy of the core causes a heat accumulation at the ignition point. Thus, the temperature gradient becomes very steep leading to a convective instability (shown in Fig. 6-4). The temperature gradient drives the energy flux to propagate inwards, fueled by convection. This propagation requires high spacial and temporal resolution, and the burning flame reaches the center ~ 6500 years after carbon ignition. This can be seen in Figure 6-4, where convection propagates inwards. Towards the end of C-burning, the temperature peak moves outwards and the resulting abundance profiles are shown in Fig. 6-5d.

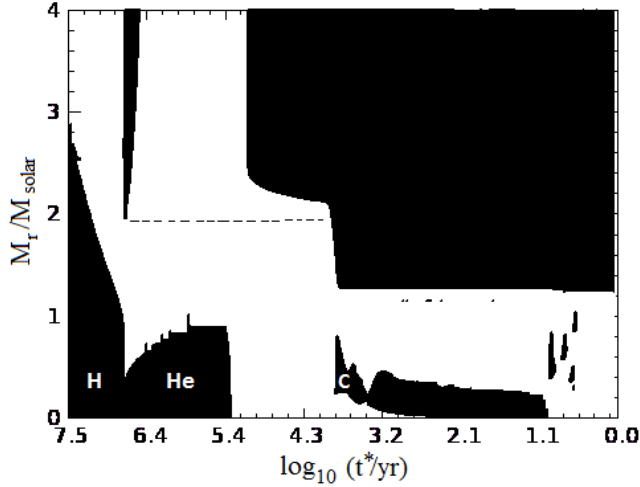


Figure 6-4: Evolution of the convective structure during the H-, He- and C-burning phases of the $9M_{\odot}$ sequence calculated with the CF88 rate. t^* is the time left until the end of calculation in years, i.e. $t^* = t_f - t$.

Table 6.4: Similar to Table 6.3 at the end of carbon-burning with the CF88 rate for the $9M_{\odot}$ sequence. Results by GB97 are provided for comparison. Masses are in solar units.

Model	M_{ONe}	ΔM_{CO}	M_{CO}	X_{12}^{\max}	$M_r(X_{12}^{\max})$	$^{12}C_c$	$^{16}O_c$	$^{20}Ne_c$
This work	1.070	0.045	1.115	0.025	0.30	0.003	0.55	0.31
GB97	1.066	0.05	1.110	0.048	0.40	0.001	0.62	0.25

Table 6.4 shows several characteristics of the He-exhausted core of the $9M_{\odot}$ model at the end of carbon-burning with the CF88 rate. As the case with the CR rate, the third most abundant nucleus in the ONe core is ^{23}Na not ^{24}Mg . Our values are comparable to those by GB97, with a difference in the amount of central and residual carbon. We attribute this discrepancy to the used reaction rates.

Comparing the results obtained with the CR and the CF88 rates, we find the following differences:

- a. Carbon ignites very close to the center with the CR rate since it is higher compared to the CF88 rate (see Fig. 2-3). Therefore, the nuclear energy generation rate overcomes the neutrino losses at a mass shell closer to the center than that with

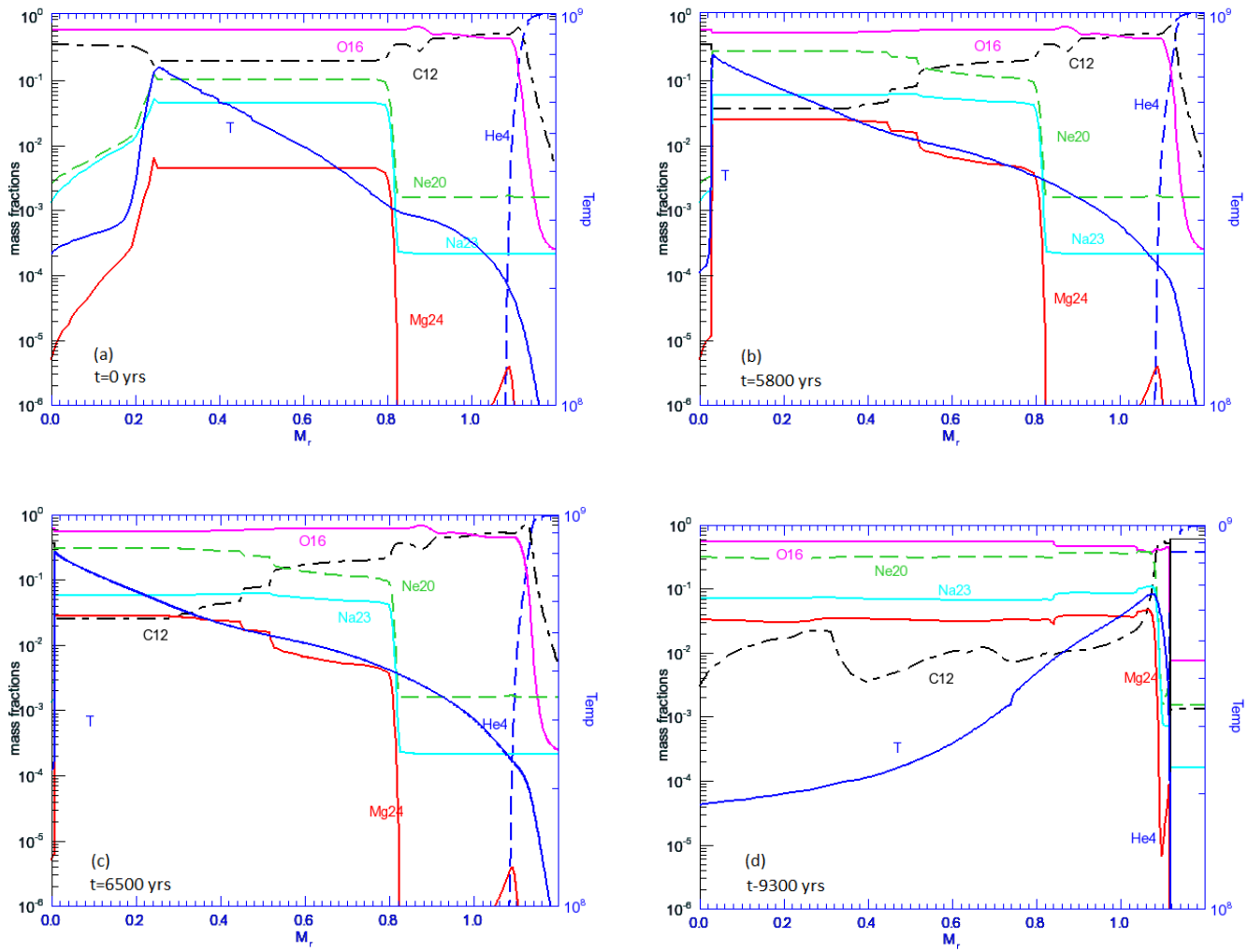


Figure 6-5: Mass fractions of the major isotopes and the temperature profiles in the helium-exhausted core at different times during carbon burning with CF88 rate ($t=0$ marks the onset of carbon burning).

the CF88 rate.

- b. The CR rate leads to larger cores as can be seen by comparing Tables 6.4 and 6.3 due to the more effective energy generation rate.
- c. The central and residual mass fractions of carbon are not very different in the two cases. However, the location of the maximum carbon residual is deeper in mass with the CR rate. The consequences this may have on the later phases of evolution, like novae eruptions for example, will be investigated in the future as we discuss in the last Chapter.

6.2 Effect of the $^{12}\text{C}+^{12}\text{C}$ fusion rate on M_{up}

Given the uncertainty on this rate, it is useful to explore its effect on the value of the critical mass M_{up} defined previously. We explore the whole range of uncertainties taking into account besides the CR and CF88 rates the upper and lower limits of the CR rate, denoted by CU and CL, respectively (see Section 2.2.2 for details).

Using the CF88 rate leads to $M_{\text{up}}=8.5M_{\odot}$, while in the case of the CR rate $M_{\text{up}}=8.3M_{\odot}$. This is not a significant difference, albeit expected since the CR rate is higher than CF88. However, the CU rate leads to $M_{\text{up}}=7M_{\odot}$, while the CL rate yields $M_{\text{up}}=9M_{\odot}$.

This range of M_{up} is quite large, which suggests the need to constrain this rate experimentally, especially that the uncertainty is not limited to the discrepancies in the derived astrophysical S-factor and in the possibility of having resonant structures, but also in the relative strength of its different channels at stellar energies, where no direct measurements are available. Unknown subthreshold resonances may have potential contributions that possibly feed one channel and not the other.

For the sake of illustration, instead of a 50-50% probability distribution we take a 55-45% probability for the α - & p-channels, respectively, and inspect the resulting abundance profiles in the ONe core of the $9M_{\odot}$ sequence. The differences in abundances are not very pronounced with this variation. However, the resulting carbon profile is different,

showing two carbon residual maxima instead of one, of mass fractions $X_{12}^{\max(1,2)} = 0.017$ and 0.00437 at the positions $0.17M_{\odot}$ and $0.53M_{\odot}$, respectively. Therefore, this probability distribution affects the shape of the carbon profile and the amount of residual carbon. The value $X_{12}^{\max(1)} = 0.017$ is very close to 0.015 which is the critical residual carbon that can induce a thermonuclear runaway (Gutiérrez et al. 2005). It is worth investigating whether this model is able to undergo a thermonuclear runaway, given the necessary conditions.

6.3 Effect of core overshooting

As argued previously, overshooting is to be considered in many situations, so we study the impact of core overshooting on M_{up} since the latter depends directly on the masses of the He and CO cores. Based on our investigations in connection with the blue loops (see section 3.2.2), we found that $0.1H_p$ is a suitable value for the overshoot distance. Clearly, this leads to the growth of the convective core. For example, the CO core of the $8M_{\odot}$ sequence is $0.468M_{\odot}$ in the standard calculation and $0.654M_{\odot}$ with overshooting.

Applying overshooting with the CF88 rate, we find that M_{up} is $8M_{\odot}$ instead of $8.5M_{\odot}$. In case of the CR rate, M_{up} is $7.5M_{\odot}$ instead of $8.3M_{\odot}$. Thus, overshooting lowers the value of M_{up} due to the increased core mass.

According to the work by Doherty et al. (2014), $M_{\text{up}} = 8.1M_{\odot}$ for solar metallicity stars, which is consistent with the value we find. They emphasize the role of overshooting in determining M_{up} as well.

6.4 Comments on the effect of mass-loss

We also studied the effect of mass-loss on M_{up} and the core composition at the end of C-burning by considering mass-loss rates of different efficiencies (see Section 2.1.1). We find that the mass-loss treatment has no direct effect on M_{up} . However, the mass-loss rate

is an important parameter during the TP-AGB phase. There is a critical envelope mass below which He-shell burning that is responsible for pulsation is not sustained and thus, pulsation does not occur. Therefore, the treatment of mass-loss used for intermediate mass stars is not suitable for SAGB stars, i.e. stars of mass $\geq 7M_{\odot}$. In fact, in SAGB stars the mass-loss rate becomes more significant than that in the case of less massive stars, resulting in a severe loss of envelope mass before pulsation sets in. Therefore, for stars in this mass range Reimers (1975) rates are used with $\eta = 0.5$.

With this mass-loss rate, we notice that the central abundances vary slightly compared to the case with no mass-loss. For example, for the $8.3M_{\odot}$, the central carbon and oxygen mass fractions at the end of He-burning are 0.5072 and 0.4682 respectively, as compared to 0.4869 and 0.4886 in the case of no mass-loss. This affects the subsequent core composition and is worth investigating in the future.

In the astrophysical scenario leading to the formation of white dwarfs, after the TP-AGB a pulse-driven superwind would reduce the envelope mass to small values ($< 10^{-3}M_{\odot}$), that the star is no longer able to maintain its large size, and it begins to shrink. The star evolves to the post-AGB phase. Eventually, the envelope mass is insufficient to maintain the temperature required for burning so the star's luminosity declines rapidly and the core spends the remainder of its life cooling off as a white dwarf, with a buffer zone that is rich in traces of hydrogen and helium on its surface.

Chapter 7

Conclusion & Future Work

7.1 Summary

In the present work, important physical processes underlying the evolution of stars in the mass range $(1-12)M_{\odot}$ have been investigated. The stars were evolved from the ZAMS till the thermal pulsations during the AGB phase. We aimed to link the internal structure to the nucleosynthesis processes which have their signature in the observed surface abundances.

Comparing theoretical predictions with available observations constitutes a powerful tool to get more insight in modeling the internal structure of stars and improve our understanding of stellar evolution in general. We summarize the main conclusions of the present work in the following.

1. **Blue loops of IMS (Ch. 3)**

As described in Chapter 3, the blue loops exhibited by IMS are especially affected by the key nuclear reaction $^{14}\text{N}(p, \gamma)^{15}\text{O}$ which controls H-burning by the CNO cycle. The formation of the loops is mainly determined by the efficacy of shell H-burning. Our results indicate that a reduction of this rate by about a factor of two, as suggested experimentally, leads to almost complete suppression of the blue loop

in the mass range $(5-7)M_{\odot}$, which is challenged by observations of Cepheids in this part of the HR diagram. One way to restore the loops is by invoking overshooting which is described in Chapter 2. Overshooting was found to affect the physical conditions that create the loop and promote its formation. In particular, moderate core overshooting was found to be very efficient in restoring the loops in the models that otherwise lacked them (see Chapter 3 for details).

Spectroscopic observations are found to be useful to constrain the physical processes in our models not only in the blue loop part of the HR diagram, but also in the region populated by RGB and early-AGB stars. A sample of observed red giant stars was considered. The masses of these stars were determined based on complete evolutionary tracks and taking into account the effect of mass-loss (see Chapter 3). Knowing their masses, their observationally inferred surface compositions were used as we describe next.

2. Mixing on the RGB (Ch. 4)

The envelope mixing processes FDUP and SDUP change the surface abundances of red giant stars and are linked to the mixing processes inside them. By comparing these abundances with the observational values, one gets insight about their internal structure. In particular, we showed in Chapter 4 that the CNO isotopic ratios ($^{16}\text{O}/^{17}\text{O}$, $^{12}\text{C}/^{13}\text{C}$ and $^{14}\text{N}/^{15}\text{N}$) are powerful diagnostic tools for the physical assumptions concerning mixing as well as for the involved reaction rates. In this respect, we studied the role of overshooting in reconciling the observationally inferred isotopic ratios with model predictions, particularly in low mass stars.

The sensitivity of surface abundances to key nuclear reaction rates was also investigated in the light of new experimental determinations. The effect of the experimental uncertainty of these rates on the oxygen isotopic ratio was also studied. A conclusion was reached that the suggested range of uncertainty in the involved reaction rates cannot explain the $^{16}\text{O}/^{17}\text{O}$ ratios in low mass stars without invoking

envelope overshooting. The newly proposed $^{14}\text{N}(p, \gamma)^{15}\text{O}$ rate is also found to affect the surface values of $^{14}\text{N}/^{15}\text{N}$ in red giants (see Chapter 4 for details).

3. Investigations of the AGB phase (Ch. 5)

This phase provides the physical conditions necessary for the operation of the s-process nucleosynthesis and other neutron-capture processes like the ^{19}F production. A challenging issue is to have sufficient production of the neutron source that leads to the formation of the main component of the s-process during the thermal pulsations of AGB stars that can match the observational data. The production of neutrons by $^{13}\text{C}(\alpha, n)^{16}\text{O}$, requires the ingestion of protons into the carbon rich layers. In Chapter 5, a diffusive model is used to describe this ingestion of protons in order to investigate the physical conditions related to the formation of ^{13}C by TDUP. We followed the evolution of the ^{13}C production leading to a ^{13}C distribution (pocket) during a thermal pulse in a $3M_{\odot}$ star. It is found that the amount of ^{13}C depends on several factors, including the H-free core mass and efficiency of overshooting during TDUP. This investigation is not yet completed and will be addressed in the future as described below.

4. Investigations of the SAGB phase (Ch. 6)

As outlined in Chapter 6, the astrophysical importance of the $^{12}\text{C}+^{12}\text{C}$ fusion reaction is well known and plays a crucial role in many stellar environments, both quiescent and explosive. However, current data show discrepancies in the derived $^{12}\text{C}+^{12}\text{C}$ cross section, as well as the presence of numerous resonance-like structures which make the extrapolation to lower energies very uncertain. The critical uncertainties in this rate affect several astrophysical models, including SAGB stars and type Ia supernovae. In fact, this reaction is one of the key factors that decide between the evolutionary paths leading to either white dwarfs or heavy element burning stages.

We have explored the effect of the uncertainty in the rate, as well as overshoot-

ing, on the progenitor mass of CO and ONe cores. The masses of these cores and the abundance profiles of important nuclear species were calculated with a newly proposed carbon-burning rate. We found that this new rate affects the burning conditions and the carbon profile in the ONe cores, which is critical for novae outbursts and SN explosions. The uncertainty in the relative strength of the different channels of the rate was also specifically addressed, where unknown resonances may introduce contributions that possibly favor one channel over the other. This is found to affect the profile of carbon in the ONe core, which motivates further experimental work in this respect for a better understanding of this important rate.

During the past years, stellar evolutionary models have been constantly improved in order to explain photometric and spectroscopic observations with higher accuracy. Such improvements were possible by accounting for the physical effects of macroscopic phenomena like rotation and magnetic fields and their associated instabilities. Our code does not yet include the effects of rotation and magnetic fields but it is worthwhile to mention that including these effects could modify the physical conditions of the mixing process in the stellar models. Moreover, attempts have been made to perform 3D calculations mainly for the aim of improving 1D calculations.

Low-mass AGB models including the effects of rotation have been developed in several works (Dominguez et al. 1996; Langer et al. 1999; Herwig et al. 2003; Siess et al. 2004; Piersanti et al. 2013). It is found that mixing induced by rotation may have important consequences on the nucleosynthesis yields. In particular, in works like Cristallo et al. (2013) for example, rotation is found to have consequences on the distribution of s-process elements in low-mass AGB stars at different metallicities, and consequently, on the chemical evolution on Galactic globular clusters. Piersanti et al. (2013) found that the effects of meridional circulation on the nucleosynthesis of s-process elements are important at low metallicities even at rather low rotational velocities. Since rotational velocities up to 10 km/s, with an average value of about 1 km/s, have been observed (Piersanti et al. 2013), including rotation in stellar models may be able to provide an

explanation for the observational discrepancies posed by standard non-rotating models.

Models including magnetic fields and magnetic instabilities, on the other hand, were also considered (Parker, 1974; Spruit, 2001; Eggenberger et al., 2005; Busso et al. 2007). These works propose that a magnetic dynamo maintains matter transport by mixing in red giants which has implications on the nucleosynthesis yields. More recently, Trippella et al. (2014) suggest that magnetic buoyancy can result in a neutron source reservoir (^{13}C) which is substantially larger (about a factor of four) than that obtained in standard models so far. The implementation of MHD effects into a stellar evolution code is quite involved and may have important implications on s-process nucleosynthesis.

Another improvement introduced to 1D hydrodynamic stellar modeling is by coupling 1D stellar evolution to 3D hydrodynamic simulations of convection in stellar atmospheres (Magic et al. 2013; 2014). Since convection is inherently a non-local 3D turbulent phenomenon, 3D model atmospheres present a more realistic framework to study this phenomenon, especially in the envelopes of giants and variable stars. 3D hydrodynamical models look very promising as they led to major revisions of the solar abundances (Asplund et al. 2005).

7.2 Future Work

This work opened the scope for further calculations in several directions. Nucleosynthesis in the TP-AGB phase is an involved topic that requires careful analysis of its physical conditions. Further work is in progress to follow the details of the s-process, for which we have a full network available. This will be carried out in a project supported by the Lebanese National Council of Scientific Research (CNRSL) in intensive collaboration with Dr. Bradley Meyer (Clemson Univ., SC, USA).

Preliminary results have been obtained on the production of ^{13}C . Work is in progress to study the factors affecting the amount of ^{13}C that can provide the necessary neutron density and initiate the s-process nucleosynthesis. These factors include the effect of the

core mass and the efficiency of the diffusion process responsible for proton ingestion into the C-rich layers. Another interesting aspect is to investigate the effects of determining the change in composition by a simultaneous calculation of the convective mixing and nuclear burning (eq. A1.10) which has feedback on the energy generation and the convective structure.

On the hand, the results obtained with the new C-burning rate will be further investigated in novae simulations (Halabi, El-Eid, José (2014), in preparation). These new models are expected to have consequences on the novae models which will be interesting to compare to recent works. Chen et al. (2014) recently investigated the dependence of the evolution of SN type Ia progenitors on the C-burning rate uncertainty and convective boundary mixing. Denissenkov et al. (2014a) also studied the effect of mixing on white dwarfs as progenitors of type Ia supernovae. It is also interesting to compare the recent simulations of classical novae by Denissenkov et al. (2014b). The effects of mass-loss are also worth exploring in more details.

This thesis has addressed several aspects of stellar evolution in the mass range under consideration and highlighted some of the present uncertainties as well as the shortcomings of the simplifications currently employed in stellar models. It has also raised several questions and leaves the door open to further investigations on different levels as outlined above.

Appendix 1

Basic Equations of Stellar Structure & Evolution

In the case of a spherically symmetric star, we have the following five equations of stellar structure written in the Lagrangian coordinates (see Kippenhahn and Weigert 1990; El Eid 1996; Kippenhahn, Weigert & Weiss 2012). The physical parameters of the star are radius r , velocity u , density ρ , pressure P , luminosity L , and temperature T which are dependent on the interior mass M_r and time.

1. Mass conservation (continuity equation):

$$\frac{\partial r}{\partial M_r} = \frac{1}{4\pi r^2 \rho} \quad (\text{A1.1})$$

2. Definition of velocity:

$$\frac{\partial r}{\partial t} = u \quad (\text{A1.2})$$

3. Momentum conservation equation:

$$\frac{\partial^2 r}{\partial t^2} = -4\pi r^2 \frac{\partial P}{\partial M_r} - \frac{GM_r}{r^2} \quad (\text{A1.3})$$

which reduces to:

$$\frac{\partial P}{\partial M_r} = -\frac{GM_r}{4\pi r^4} \quad (\text{A1.4})$$

in case of hydrostatic equilibrium i.e. $\frac{\partial^2 r}{\partial t^2} = 0$.

4. Energy conservation equation:

$$\frac{\partial L}{\partial M_r} = \epsilon_{nucl} - \epsilon_v - \frac{\partial E}{\partial t} + \frac{P}{\rho^2} \frac{\partial \rho}{\partial t} = \epsilon_{nucl} - \epsilon_v + \epsilon_{grav} \quad (\text{A1.5})$$

where $\epsilon_{grav} < 0$: energy due to gravitational attraction

$\epsilon_v < 0$: energy due to neutrino losses

$\epsilon_{nucl} > 0$: energy generation rate due to nuclear reactions

E is the internal energy

5. Equation for energy transport:

$$\frac{\partial T}{\partial M_r} = -\frac{GM_r T}{4\pi r^4 P} \nabla \quad (\text{A1.6})$$

where $\nabla = \nabla_{ad}$ in the deep convective interiors as given by the *Mixing Length Theory* (MLT) (Kippenhahn and Weigert 1990 and references therein)

$$\nabla_{ad} = \frac{\partial \ln T}{\partial \ln P} \Big|_S = \frac{P}{T} \frac{\delta}{\rho C_p}. \quad \text{and} \quad \delta = -\frac{\partial \ln \rho}{\partial \ln T} \Big|_P \quad (\text{A1.7})$$

and $\nabla = \nabla_{rad}$ for radiative regions

$$\nabla_{rad} = \frac{\partial \ln T}{\partial \ln P} \Big|_{rad} = \frac{3}{16\pi acG} \frac{\kappa L P}{M_r T^4} \quad (\text{A1.8})$$

where κ is the Rosseland mean opacity.

6. Change in composition:

One can write a general set of N differential equations for the time rate of change of individual nuclear abundances as:

$$\frac{dY(Z, A)}{dt} = \sum_{Z', A'} \lambda_{Z', A'} Y_{Z', A'} + \sum_{Z', A'} \rho N_A \langle \sigma v \rangle_{Z', A'} Y_{Z', A'} Y_n \quad (\text{A1.9})$$

where the first term on the right-hand-side includes β -decays and photodisintegrations. The second term includes all involved nuclear reactions.

Therefore, the abundance change of any isotope is given by

$$\frac{dX_i}{dt} = \frac{\partial X_i}{\partial t} \Big|_{nuclear} + \frac{\partial}{\partial M_r} \left[(4\pi r^2 \rho)^2 D \frac{\partial X_i}{\partial M_r} \right] \quad (\text{A1.10})$$

where X_i is the mass fraction of the respective isotope. The first term on the right-hand-side represents the abundance change in isotope X due to nuclear burning, as determined by the nucleosynthesis network. The second term is the diffusion equation that describes the mixing of the elements inside the convective zones as explained in Chapter 2.

In addition to the equations for the other thermodynamic properties:

$$C_p = C_p(P, T, X_i)$$

$$\delta = \delta(P, T, X_i)$$

$$\nabla_{ad} = \nabla_{ad}(P, T, X_i)$$

$$\kappa = \kappa(P, T, X_i) \quad (\text{Rosseland mean of the opacity}).$$

Equation of State

To close the system of equations with the 5 unknowns: r, u, T, L and ρ , we consider the equation of state of stellar matter: $P = P_{gas} + P_{rad}$ where P_{rad} is the radiation pressure obtained from the physics of blackbody radiation:

$$P_{rad} = \frac{1}{3}aT^4 \tag{A1.11}$$

where a is a radiation constant.

For the dilute envelope, the ideal gas law applies:

$$P_{gas} = \frac{R}{\mu}\rho T \tag{A1.12}$$

where R is the gas constant and μ is the mean molecular weight.

For a neutral gas: $\mu = \mu_o$, given by:

$$\frac{1}{\mu_o} = \sum_j \frac{X_j}{A_j} \tag{A1.13}$$

where X_j is the mass fraction of component j .

For a fully ionized gas, each nucleus j contributes Z_j free electrons. In a mixture of electrons and nuclei:

$$P_e = \frac{R}{\mu_e} \rho T \quad (\text{A1.14})$$

and

$$\frac{1}{\mu_e} = \sum_j \frac{X_j Z_j}{A_j} \quad (\text{A1.15})$$

μ_e is the mean molecular weight per electron.

In case of partial ionization, μ_e will be influenced by the occupation of the excited states in one atom. Thus, Saha equation is implemented, including all relevant excited states to calculate μ_e everywhere in the model.

Degeneracy effects become more pronounced when the contraction of the core leads to high densities. In this case, Fermi-Dirac statistics are used for the treatment of the electron gas. Fermi-Dirac integrals with suitable approximations are widely used to determine P_e , depending on the range of density and temperature (details of including the equation of state of degenerate electron gas is given by El Eid 1996).

Boundary Conditions

An obvious condition is that at the center of the star, the luminosity, mass and velocity have to vanish. i.e.

$$r \longrightarrow 0 : u = 0, L = 0, M \rightarrow 0.$$

Another set of conditions determines the dynamic properties of the photospheric surface of the star, in terms of pressure and luminosity.

$$r \longrightarrow R : L = 4\pi R^2 \sigma T_{eff}^4 \quad \text{Boltzmann Law (Black Body approximation)}$$

An expression for the effective density is given by:

$$\rho_{eff} = \frac{\mu}{RT_{eff}} (P_{eff} - \frac{1}{3} a T_{eff}^4)$$

where $P_{eff} \simeq \int_R^\infty g \rho dr \simeq \int_R^\infty g_o \rho dr$.

but $\tau = \bar{k} \int_R^\infty \rho dr$, and at the photosphere, $\tau = \frac{2}{3}$ (grey atmosphere)

$\implies \rho dr = \frac{2}{3} \frac{1}{\bar{k}}$ giving:

$$P_{eff} = \frac{GM}{R^2} \frac{2}{3} \frac{1}{\bar{k}} \quad (\text{A.16})$$

A final expression for ρ_{eff} is given by:

$$\rho_{eff} = \frac{\mu}{RT_{eff}} \left[\frac{GM}{R^2} \frac{2}{3} \frac{1}{\bar{k}} - 1.4247 \times 10^{-11} T_{eff}^4 \right] \quad (\text{A.17})$$

Thus, the non-linear differential equations are solved for with the boundaries specified at $r = 0$ and $r = R$. The star is discretized into a 1D grid, differential equations are transformed to difference equations and the system is solved using multidimensional Newton-Raphson method. This is called an “*evolutionary code*”. Our code has been tested for low, intermediate and high mass stars (El Eid 1994,1995; El Eid et al 2009; Halabi et al. 2012). For a given time t, in the interval $[0, M]$, a solution, i.e. $[r, p...x;](m)$ is called a “*stellar model*”.

Appendix 2

THE EFFECT OF THE $^{14}\text{N}(p, \gamma)^{15}\text{O}$ REACTION ON THE BLUE LOOPS IN INTERMEDIATE-MASS STARS

GHINA M. HALABI¹, MOUNIB F. EL EID¹, AND ARTHUR CHAMPAGNE²

¹ Department of Physics, American University of Beirut, Beirut, Lebanon

² Department of Physics and Astronomy, The University of North Carolina, Chapel Hill, NC, USA

Received 2012 September 1; accepted 2012 October 17; published 2012 November 19

ABSTRACT

We present stellar evolutionary sequences of stars in the mass range 5–12 M_{\odot} , having solar-like initial composition. The stellar models are obtained using updated input physics, including recent rates of thermonuclear reactions. We investigate the effects of a modification of the $^{14}\text{N}(p, \gamma)^{15}\text{O}$ reaction rate, as suggested by recent evaluations, on the formation and extension of the blue loops encountered during the evolution of the stars in the above mass range. We find that a reduced $^{14}\text{N}(p, \gamma)^{15}\text{O}$ rate, as described in the text, has a striking impact on the physical conditions of burning and mixing during shell hydrogen burning when the blue loops are formed. In particular, we find that the efficiency of shell hydrogen burning is crucial for the formation of an extended blue loop. We show that a significantly reduced $^{14}\text{N}(p, \gamma)^{15}\text{O}$ rate affects severely the extension of the blue loops and the time spent by the star in the blue part of the Hertzsprung-Russell diagram in the mass range 5–7 M_{\odot} if the treatment of convection is based on the Schwarzschild criterion only. In this case, envelope overshooting helps to restore well-extended blue loops as supported by the observations of the Cepheid stars. If core overshooting is included during the core hydrogen and core helium burning phases, the loop formation and its properties depend on how this overshooting is treated for a given stellar mass range, as well as on its efficiency.

Key words: Nuclear reactions, nucleosynthesis, abundances – stars: evolution – stars: interiors – stars: variables: Cepheids

Online-only material: color figures

1. INTRODUCTION

A remarkable and intriguing feature of the evolution of stars in the mass range 5–12 M_{\odot} is that they develop blue loops after the onset of core helium burning, when the star reaches the red giant branch (RGB). This crossing of the Hertzsprung-Russell diagram (HRD) toward higher effective temperatures and back to the RGB is commonly called a “blue loop” in the literature. It is well established that the blue loops are necessary for explaining the observed non-variable yellow giants, supergiants, and the δ -Cepheids in open galactic clusters (Mermilliod 1981; Schmidt 1984; Evans 1993; Fernie et al. 1995).

The study of the formation and evolution of the blue loops during core helium burning in intermediate-mass stars (hereafter IMS) involves various aspects of stellar evolution. The association of these loops with the Cepheid stars in principle allows a quantitative test of the theory of stellar evolution. Another point of importance is that the blue loop occurs during a relatively long lasting evolutionary phase during which the star has a high probability to be observed. A comprehensive discussion of the physical parameters influencing the properties of the loops is beyond the scope of the present paper. Our aim in this work is to focus on one important issue, namely, the effect of the $^{14}\text{N}(p, \gamma)^{15}\text{O}$ reaction on the properties of the blue loops in IMS. The rate of this reaction is still not settled on experimental ground (see Section 2.2). As we shall see in the present work, the recent suggested modifications of this rate have a strong impact on the efficiency of shell hydrogen burning (hereafter briefly shell H-burning) which, in turn, significantly influences the behavior of the loops in a certain mass range (see Section 3). It is not our aim to review the relatively large body of the literature on the blue loops in IMS. A basic discussion concerning their formation is given in the text by Kippenhahn & Weigert (1990) and references therein. In particular, it is emphasized that the extension of the loops (the distance between their bluest tips

and the Hayashi line in the HRD) depends on the stellar mass. We show in Section 3 that this dependence is also sensitive to the rate of the $^{14}\text{N}(p, \gamma)^{15}\text{O}$ reaction (referred to as N14 rate in the following). Another point emphasized by Kippenhahn & Weigert (1990) is the efficiency of shell H-burning as determined by the shape of the hydrogen profile (or, more briefly, the H-profile). Their discussion indicates that the properties of the loop depend on how shell H-burning consumes the lower tail of the H-profile. The efficiency of shell H-burning and its dependence on the shape of the H-profile were also discussed by Stothers & Chin (1991).

A general agreement in all calculations dealing with the loop formation is that the loop is triggered when the shell H-burning is reinforced during core He-burning (see, for example, El Eid 1995; Cassisi et al. 2002; Lai & Li 2011). This reinforcement depends crucially on the shape of the H-profile created after the first dredge up (FDUP) on the RGB. As shall be presented in Section 3, the shape of the profile is also influenced by the N14 rate in a certain mass range.

The blue loops are also sensitive to mixing processes like overshooting, which denotes extra mixing beyond a convective boundary determined by the Schwarzschild criterion for convection. Envelope overshooting at the base of the convective envelope on the RGB has been invoked in several works (Alongi et al. 1991; Stothers & Chin 1991; Lai & Li 2011). This type of overshooting is found to promote the formation and extension of blue loops in IMS because it results in a deeper penetration of the convective envelope, so that an H-discontinuity is created deep enough to reinforce shell H-burning. We discuss this issue in Section 3.6. Core overshooting also affects the loop properties as discussed in several works (Matraka et al. 1982; Valle et al. 2009; Stothers 1991; Neilson et al. 2011). However, this effect needs to be elaborately discussed in light of the updated N14 rate. This issue will be addressed in full details in a forthcoming paper as this work emphasizes mainly on the effect of the N14 rate.

The effect of the N14 rate on the properties of the loop has been investigated in works like Xu & Li (2004) and Weiss et al. (2005) where the importance of this rate is emphasized. In the present work, we describe in details the change of the internal structure of the stars under consideration due to the modification of the N14 rate based on an up-dated evaluation (see Section 2.2). We show that the N14 rate has a significant effect on the loop formation and extension especially in the mass range 5–7 M_{\odot} .

The present work is organized as follows. In Section 2, a brief description of the stellar code is given and the present situation concerning the rate of $^{14}\text{N}(p, \gamma)^{15}\text{O}$ is outlined. In Section 3, the present results based on different $^{14}\text{N}(p, \gamma)^{15}\text{O}$ rates are described and discussed including the effects of envelope overshooting. Comparison with observations are given in Section 4 and concluding remarks are presented in Section 5. For time-pressed readers, we recommend the conclusion which sufficiently highlights the main findings of this work.

2. STELLAR MODEL CALCULATIONS

2.1. Stellar Evolution Code

The evolutionary sequences presented in this work are obtained using the stellar evolution code described by El Eid et al. (2004, 2009) and references therein. This code is a one-dimensional implicit hydrodynamic Lagrangian code based on solving the discretized stellar structure equations using Newton–Raphson iteration in five dimensions. We shall use a short description of this code as “HYADES.” The version we have used in the present calculation includes the following modifications.

1. The models presented in this work are evolved from the main sequence until the end of core helium burning with the mass-loss rates calculated according to Reimers (1975). We note that mass loss does not affect our present results.
2. The reaction rates we have used are those recommended by the “JINA REACLIB” database (Cyburt et al. 2010). For the $^{14}\text{N}(p, \gamma)^{15}\text{O}$ rate, we use three compilations: (1) the rate provided by NACRE (Angulo et al. 1999), which we refer to as the *N-rate*, (2) a new evaluation of this rate as described in Section 2.2 which we call *C-rate* in the following, and (3) the rate given by the LUNA collaboration (Imbriani et al. 2005), hereafter briefly referred to as the *L-rate*.

2.2. The Status of the $^{14}\text{N}(p, \gamma)^{15}\text{O}$ Rate

As mentioned above, the $^{14}\text{N}(p, \gamma)^{15}\text{O}$ reaction has been re-examined, both experimentally and theoretically and the principle finding is that the reaction rate is reduced by about 40%–45% with respect to the rate previously tabulated by the NACRE collaboration (Angulo et al. 1999) for $T_9 \leq 0.1$. A summary and re-evaluation of experimental and theoretical investigations through 2009 is given by Adelberger et al. (2011).

The $^{14}\text{N}(p, \gamma)^{15}\text{O}$ reaction mechanism displays a complicated interplay of direct and resonant capture. The latter component involves a sub-threshold resonance at $E_{\text{cm}} = -504$ keV (corresponding to an excited state in ^{15}O at an excitation energy $E_x = 6.79$ MeV), a low-energy resonance at $E_{\text{cm}} = 259$ keV, and interference between the sub-threshold resonance and higher-lying states. All of these features are manifested at the energies of interest here, $E_{\text{cm}} \lesssim 110$ keV. The three strongest transitions in the $^{14}\text{N}(p, \gamma)^{15}\text{O}$ reaction at the temperatures of interest populate the 6.79 MeV, ground, and 6.17 MeV states in ^{15}O , respectively, via a combination of direct capture into these states

(followed by γ -decay to the ground state) or through decay into these states from the low-energy tail of the 259 keV resonance. Thus the cross sections for these (and the other, less significant) transitions have a pronounced energy dependence. The chief difference between the present rate and the earlier NACRE rate is that the strength of the ground-state transition is significantly reduced. This transition is dominated by the sub-threshold resonance at low energies, the effect of which is seen indirectly at the energies accessible to measurement through a pronounced interference feature that appears on both the low-energy and high-energy sides of the 259 keV resonance.

The individual transitions that contribute to the total cross section have been measured by the LUNA collaboration (Formicola et al. 2004 and Imbriani et al. 2005) and by Runkle et al. (2005). As is customary, these results are reported in terms of an astrophysical *S*-factor, which is related to the cross section via

$$S(E) = E\sigma(E)\exp(2\pi\eta), \quad (1)$$

where E is the energy in the center of mass, $\sigma(E)$ is the reaction cross section, and η is the Sommerfeld parameter. Although these measurements extend the *S*-factors to lower energies than previous measurements, they are still well above the *stellar* energies of interest. Consequently, the *S*-factors have been extrapolated to stellar energies using *R*-matrix theory. Since the *R*-matrix is a fit to the data, the reliability of the extrapolation is determined by the quality of the data and the degree to which the data adequately sample the various components of the reaction process. Although the total *S*-factors at zero energy from these three studies are in agreement ($S(0)_{\text{tot}} = 1.7 \pm 0.2$, 1.61 ± 0.08 , and 1.68 ± 0.09 keV b, respectively), there are systematic differences in the energy dependence of the *S*-factor. These differences stem largely from the different approaches employed in the *R*-matrix fits to the capture data and center primarily on the ground-state transition where the LUNA result is $S(0)_{\text{gs}} = 0.25 \pm 0.06$ keV b versus 0.49 ± 0.08 keV b in Runkle et al. (2005). The reason for this large discrepancy is that the focus of these measurements was on extending the cross sections to lower energies and none went sufficiently high in energy to constrain the tails of the higher-lying resonances that turn out to significantly influence the behavior of the cross section at low energies. Thus, although the actual data are largely in agreement, different procedures were adopted for including the higher-lying states into the *R*-matrix analysis. An *R*-matrix re-analysis by Angulo et al. (2005) of all of the (then) available capture data (Schröder et al. 1987; Formicola et al. 2004; Runkle et al. 2005) resulted in $S(0)_{\text{tot}} = 1.70 \pm 0.12$ keV b and $S(0)_{\text{gs}} = 0.25 \pm 0.08$ keV b and an overall energy dependence that was consistent with the LUNA result. Later LUNA measurements of S_{tot} (Bemmerer et al. 2006; Lemut et al. 2006) also clearly favored the LUNA *R*-matrix analysis. The more recent *R*-matrix re-analysis by Adelberger et al. (2011) yields $S(0)_{\text{tot}} = 1.66 \pm 0.12$ keV b, $S(0)_{\text{gs}} = 0.27 \pm 0.05$ keV b and again an overall energy dependence that is in agreement with the LUNA $S(E)_{\text{tot}}$.

Several relevant results have appeared since the publication of Adelberger et al. (2011). High-precision measurements of the energy and width of the 259 keV resonance have been reported by Borowski et al. (2009), which could provide constraints on future *R*-matrix fits. In addition, the LUNA collaboration have carried out new cross-section measurements at three energies just above the 259 keV resonance using Ge clover detectors to reduce coincidence summing (Marta et al. 2011; earlier results for the ground-state transition were included in the

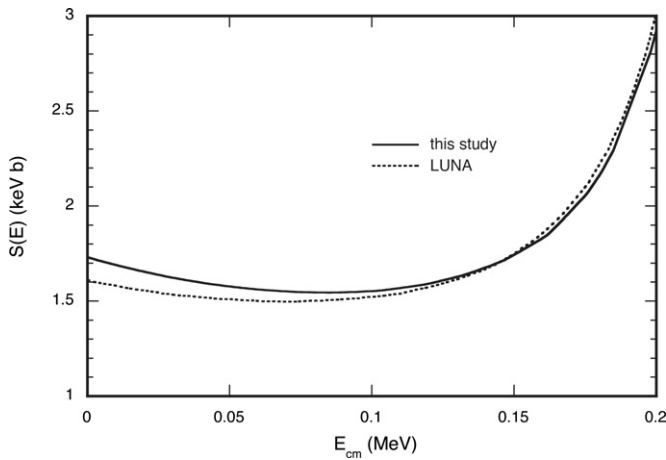


Figure 1. Total S -factors for the $^{14}\text{N}(p, \gamma)^{15}\text{O}$ reaction. That from the present study is denoted by the solid line while the LUNA S -factor (Imbriani et al. 2005) is given by the dotted curve.

analysis of Adelberger et al. 2011). The main advantage of these new data is their higher precision for the ground-state transition in the interference region, which better constrains the strength of the sub-threshold resonance. They also tabulate new branching ratios for the decay of the 259 keV resonance. New measurements of asymptotic normalization coefficients (ANCs) are described in Artemov et al. (2012) and were used to fix the contributions from direct capture in new R -matrix fits to the existing (p, γ) data. This approach differs from most previous R -matrix fits in which the ANCs are treated as derived quantities and allowed to vary in the calculations. Overall, the calculated S -factors are consistent with the LUNA S -factors (Imbriani et al. 2005), but with somewhat higher uncertainties. Finally, the $^{14}\text{N}(p, p)^{14}\text{N}$ reaction has been measured (Bertone 2010), which permits simultaneous R -matrix fits of the (p, γ) and (p, p) data. Thus far, multichannel fits have been performed for the 6.79 MeV and ground-state transitions, and interestingly, the recommended zero-energy S -factor for the ground-state transition is $S(0)_{\text{gs}} = 37$ keV b, which is midway between the LUNA result and that of Runkle et al. (2005).

The thermonuclear reaction rate is the thermal average of the cross section and relative velocity of the reacting particles and is related to the total S -factor through (Iliadis 2007)

$$N_A \langle \sigma v \rangle = N_A \left(\frac{8}{\pi \mu} \right)^{1/2} (kT)^{-3/2} \int_0^\infty S(E)_{\text{tot}} e^{-2\pi\eta} e^{-E/kT} dE, \quad (2)$$

where N_A is Avogadro's number, μ is the reduced mass, k is Boltzmann's constant, and T is the temperature. This expression was integrated numerically using a revised total S -factor, $S(E)_{\text{tot}}$. This S -factor is derived from the multichannel R -matrix fits for the 6.79 MeV and ground-state transitions (Bertone 2010), the recommended S -factor for the 6.17 MeV transition (Adelberger et al. 2011) and the LUNA fits for the weaker transitions to the 5.18 MeV and 5.24 MeV states (Imbriani et al. 2005). The tails of the 259 keV resonance were calculated using a resonance energy $E_{\text{cm}} = 259.0 \pm 0.3$ keV and total width $\Gamma_{\text{cm}} = 1040 \pm 31$ eV (Formicola et al. 2004) and the recommended resonance strength $\omega\gamma = 13.1 \pm 0.6$ meV (Adelberger et al. 2011). The branching ratios for decay of the resonance into lower-lying states (and thus its contribution to the individual transitions) was calculated from a weighted average of the values appearing in Table 4 of Marta et al. (2011). A comparison of

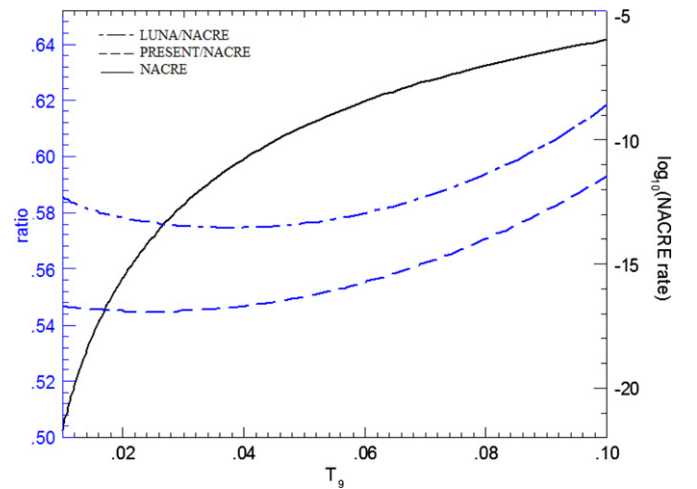


Figure 2. Used $^{14}\text{N}(p, \gamma)^{15}\text{O}$ reaction rates relative to the tabulated NACRE analytic rate (JINA ReacLib database). The solid line is the value of the reference NACRE rate (scale on the right axis).

(A color version of this figure is available in the online journal.)

our revised S -factor and the LUNA S -factor (Imbriani et al. 2005) is shown in Figure 1. The maximum difference is 7.5% at $E_{\text{cm}} = 0$, which is comparable to the uncertainty in the R -matrix extrapolations. The reaction rate derived from our S -factor is higher than the LUNA rate, but by only 2%–6% for $T_9 = 0.01$ –0.1. Note, however, that the analytic expression for the LUNA rate given in Imbriani et al. (2005) is higher (by 7%–15%) than what is obtained by integrating the S -factor using Equation (2).

In Figure 2, we compare the three different thermonuclear reaction rates according to the mentioned compilations. In case of the NACRE and LUNA rates (N -rate and L -rate, respectively), we have used the rates as described in Section 2. As for the new rate presented in this paper (C -rate), the following polynomial fit has been used:

$$C\text{-rate}/N\text{-rate} = 8.53T_9^2 - 0.423T_9 + 0.550.$$

Figure 2 also shows that both the C -rate and the L -rate are significantly lower compared to NACRE compilation for the relevant temperature range by approximately a factor of two.

3. EVOLUTIONARY RESULTS

3.1. General Overview

We present a set of evolutionary sequences for stars in the mass range 5–12 M_\odot with the initial composition $(X, Y, Z) = (0.7, 0.28, 0.02)$. In all calculations we have used for the mixing length parameter a value of 2.0 pressure scale heights.

The stellar models are calculated from the zero-age main sequence until the end of core helium burning. The evolutionary tracks in the HRD are shown in Figures 3–5 as they are obtained with the same input physics except the N14 rate, for which the three different rate compilations introduced in Section 2.1 are adopted. The evolutionary tracks show interesting effects of the N14 rate on the blue loops, which are summarized as follows.

1. Figure 3 shows the evolutionary tracks as obtained using the N -rate. It is clear that well-extended blue loops are formed for the indicated mass range. This feature is in agreement with observations indicating the location of Cepheids and yellow giants as shall be shown later. However, according

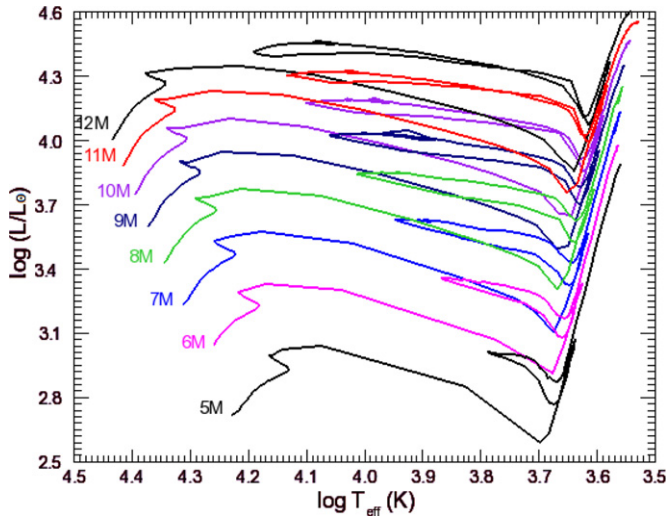


Figure 3. Evolutionary tracks in the HRD for the indicated stellar masses evolved from the zero-age main sequence until the end of core helium burning. The N -rate is used for the $^{14}\text{N}(p, \gamma)^{15}\text{O}$ reaction; see the text. (A color version of this figure is available in the online journal.)

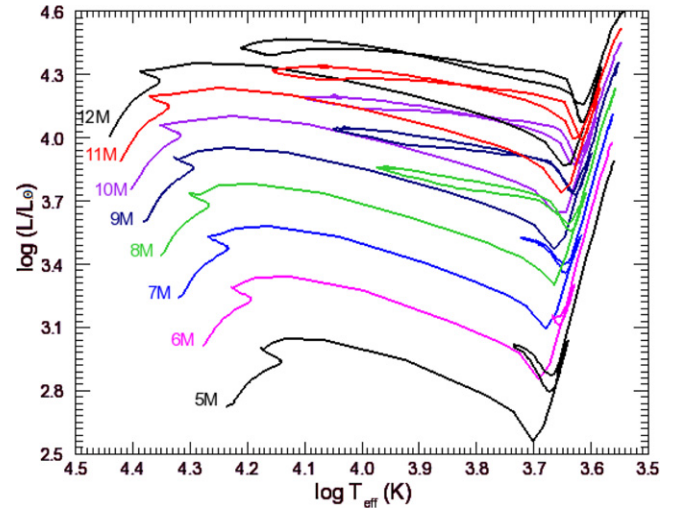


Figure 5. Same as Figure 3, but the C -rate is used for the $^{14}\text{N}(p, \gamma)^{15}\text{O}$ reaction. Note the impressive reduction in the extension of the blue loops in the mass range $5\text{--}7 M_{\odot}$ with this rate. This undesirable feature leaves a considerable number of observed stars unexplained as we shall show later. (A color version of this figure is available in the online journal.)

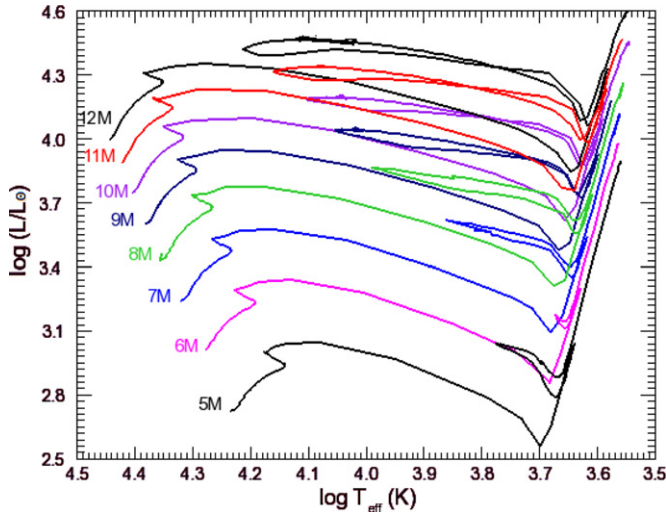


Figure 4. Same as Figure 3, but the L -rate is used for the $^{14}\text{N}(p, \gamma)^{15}\text{O}$ reaction. Note that the blue loop of the $6 M_{\odot}$ model is almost suppressed. (A color version of this figure is available in the online journal.)

to recent evaluations, the N -rate should be reduced in its efficiency. Therefore, we have redone the calculations with the modified N14 rates for comparison.

2. Figures 4 and 5 show the tracks calculated with the L -rate and C -rate, respectively. Stars of masses $8 M_{\odot}$ and above show similar loops as those obtained with the N -rate. However, there is an obvious systematic reduction in the extension of the loops in stars of masses below $8 M_{\odot}$. In particular, the blue loop in the $6 M_{\odot}$ is nearly suppressed when either rate is used. This shows that the effect of N14 rate on the loops depends on the stellar mass, specifically, it is most pronounced in the mass range $5\text{--}7 M_{\odot}$ according to our results. We are not aware of any previous elaborate discussion of this effect of the N14 rate in the literature, and it is worthwhile to present a physical explanation.

This explanation should address the question of why the N14 rate significantly affects the blue loops in the above mass range but has essentially no noticeable effect on the upper border of

this mass range. This will allow us to figure out how the N14 rate affects the internal structure and leads to a modification of the blue loops as described. This is the subject of the following sections.

3.2. Evolutionary Sequence with the N -rate

We recall that the N -rate labels the N14 rate according to the evaluation by NACRE. The evolutionary sequences presented in Section 3.1, which are calculated with this rate, develop well-extended blue loops. However, we note an impressive reduction in the extension of these loops in the mass range $5\text{--}7 M_{\odot}$, especially for the $6 M_{\odot}$ and $7 M_{\odot}$ stars calculated with the C -rate which is less efficient than the N -rate (see Figure 5). Therefore, we present the details of the physical conditions leading to the blue loop formation and extension in the case of the $6 M_{\odot}$ star, and then compare the results with those obtained with the other rates.

In Figure 6(a), we show the evolutionary track of the $6 M_{\odot}$ star during core helium burning, with relevant evolutionary stages indicated on the track and labeled 1–3. This loop is explained with the help of Figure 6(b), where several relevant quantities are displayed as a function of the central helium mass fraction ($X_c(\text{He})$). These are the star's luminosity (L_{star}), the luminosity due to core helium burning (L_{He}), the luminosity due to shell hydrogen burning (L_{H}), the central temperature T_c , and the effective temperature T_{eff} . Note that L_{He} and L_{H} are the integrated energy generation rates over the mass range where these burning modes are efficient.

The luminosity L_{H} supplies the major fraction of the star's luminosity (L_{star}), except during the very late phase of core helium burning (after point 3 in Figure 6(b)). However, L_{H} decreases steadily between points 1 and 2, and this leads L_{star} to decrease as well. The decrease in L_{H} is due to the fact that shell H-burning becomes weaker because it has consumed the lower tail of the H-profile, so that the hydrogen shell source narrows and migrates outward in mass. This feature is evident in the change of the shape of the H-profile between points 1 and 2 depicted in Figures 7(a) and (b), respectively.

As core He-burning proceeds, and starting at point 2 in Figure 6(b), L_{H} starts to increase, indicating the strengthening

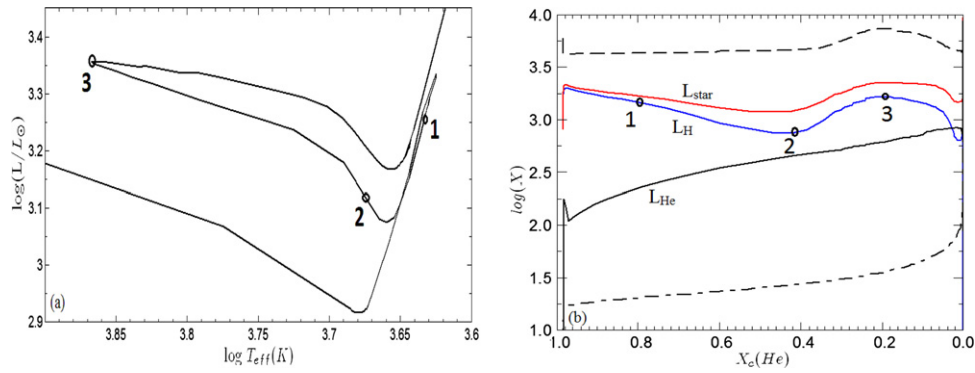


Figure 6. (a) HRD showing the blue loop of a $6 M_{\odot}$ model evolving through core helium burning when the N -rate is used for the $^{14}\text{N}(p, \gamma)^{15}\text{O}$ reaction. The marked points are crucial evolutionary stages discussed in the text. (b) Several quantities are displayed as a function of the central helium mass fraction ($X_c(\text{He})$) (see the text). The central temperature (dot-dashed) is shown in units of 10^8K and the effective temperature (dashed) is shown as $\log(T_{\text{eff}})$. The points labeled 1–3 represent the same evolutionary stages in both panels. See the text for details.

(A color version of this figure is available in the online journal.)

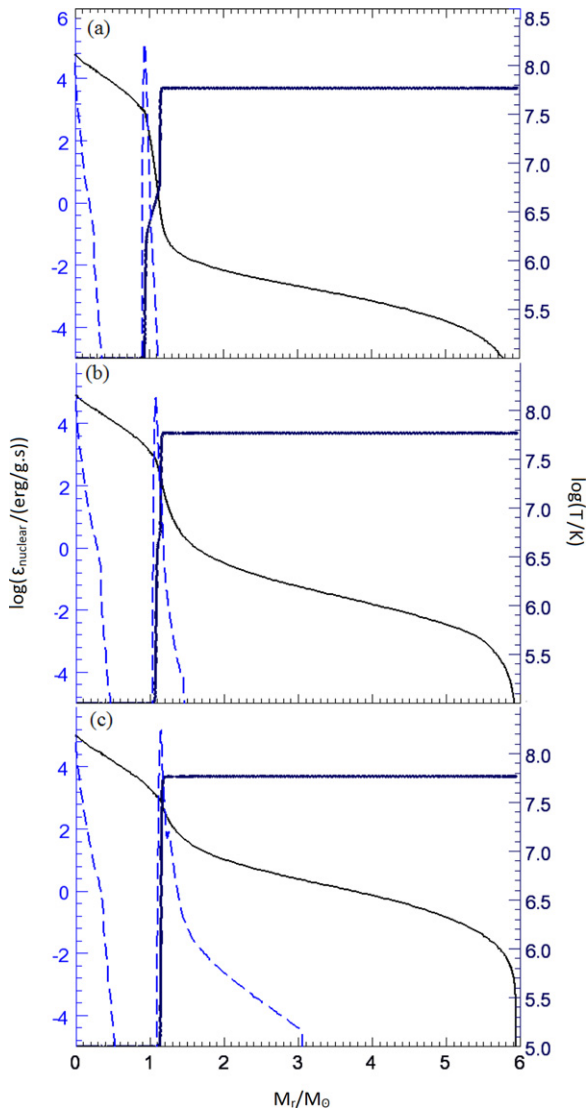


Figure 7. Energy generation rate by hydrogen and helium burning (dashed lines), temperature profile (solid line), and the hydrogen profile (thick line) as a function of interior mass for the considered $6 M_{\odot}$ star. Panels (a), (b), and (c) are taken at the points labeled 1, 2, and 3 in Figure 6, respectively. Note that the hydrogen abundance has been shifted upward in order to match the scale of the right side axis, that is $4X_{\text{H}} + 5$.

(A color version of this figure is available in the online journal.)

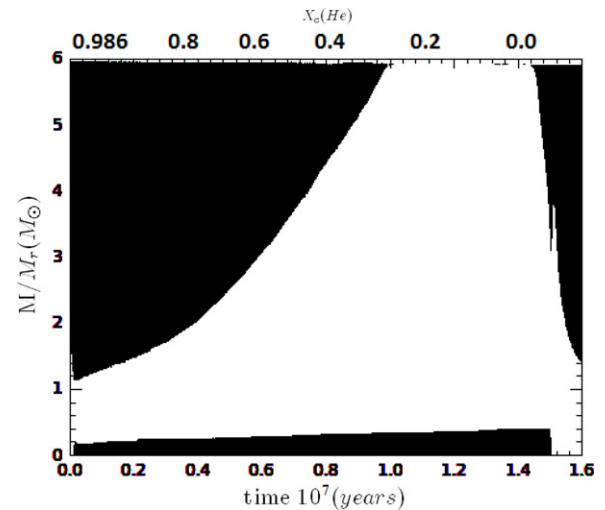


Figure 8. Evolution of the internal convective structure as a function of time of the $6 M_{\odot}$ sequence during core He-burning. Black regions are convective and white regions are radiative. Time is set to zero at the end of core hydrogen burning.

of shell H-burning. This increase lasts until point 3 and is concurrent with the formation of the blue loop as seen in Figure 6(a). The burning is strengthened due to the merging between the H-shell source and H-profile. The shell source becomes stronger and the loop achieves its bluest point (highest T_{eff}) when the shell H-burning has created a step-like shape of the H-profile. These features are shown successively in Figures 7(a)–(c), taken at the positions 1–3, respectively. Toward the end of core helium burning, L_{H} decreases again steadily and the star evolves back to the RGB, where it terminates its core He-burning.

These results show that the formation and extension of the blue loop is strongly influenced by the efficiency of shell H-burning, but in a rather subtle way. On the RGB, the relatively strong N -rate leads to efficient shell H-burning which causes the layers above the shell source to expand vigorously (we will discuss this later in connection with Figure 10), causing the envelope convection to penetrate deeper in mass so that the resulting H-discontinuity will be located at a closer proximity to the shell source, favoring the formation of an extended loop.

For completeness, Figure 8 shows the evolution of the convective structure of the $6 M_{\odot}$ star during core helium

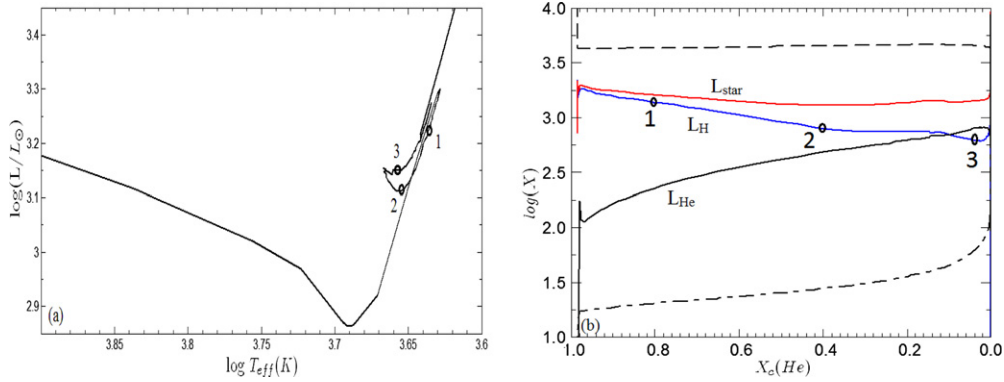


Figure 9. Same as Figure 5, obtained with the *C*-rate. The points 1–3 represent the same evolutionary stages in both panels. (A color version of this figure is available in the online journal.)

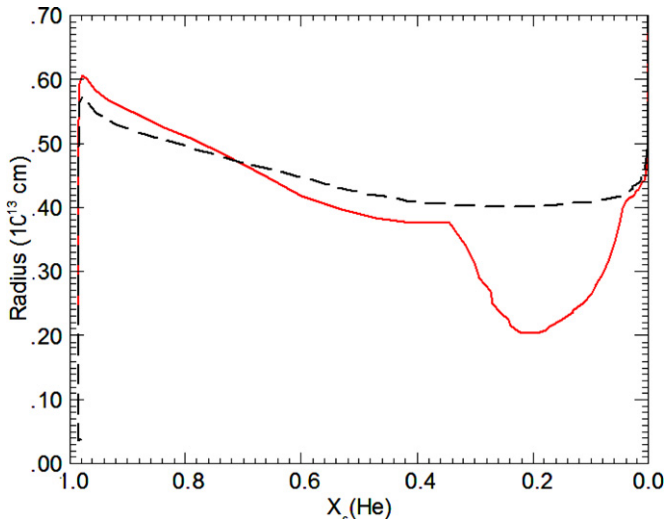


Figure 10. Radius of the $6 M_{\odot}$ star as a function of central helium during core He-burning with the *N*-rate (solid line) and the *C*-rate (dashed line). Note that with the *N*-rate, the radius decreases beyond $X_c(\text{He}) = 0.36$, which corresponds to the blue loop phase. With the *C*-rate, there is no envelope contraction where the loop is nearly suppressed.

(A color version of this figure is available in the online journal.)

burning. It is clear that the recession of convection in the envelope coincides with the blue loop phase during which the envelope contracts and the temperature above the shell source increases. This leads to a decrease in the opacity and the envelope becomes radiative. When the star evolves back to the RGB at the end of core helium burning, convection in the envelope develops again.

3.3. Evolutionary Sequence with the *C*-rate

As described in Section 3.1, adopting the *C*-rate for the $^{14}\text{N}(p, \gamma)^{15}\text{O}$ reaction leads to an almost complete suppression of the blue loop for the sequence of the $6 M_{\odot}$ star. This is illustrated in Figure 9(a) showing its evolution during core helium burning, with points marked 1–3 relevant to our discussion.

We emphasize that the following results are obtained with the same input physics except for using the *C*-rate. Figure 9(b) shows that L_{H} steadily decreases until position 3 which marks the end of core helium burning. Thus, the shell H-burning is not reinforced and the loop is barely formed. This remarkably different behavior of the loop is clearly related to the reduced efficiency of the hydrogen shell source as a consequence of

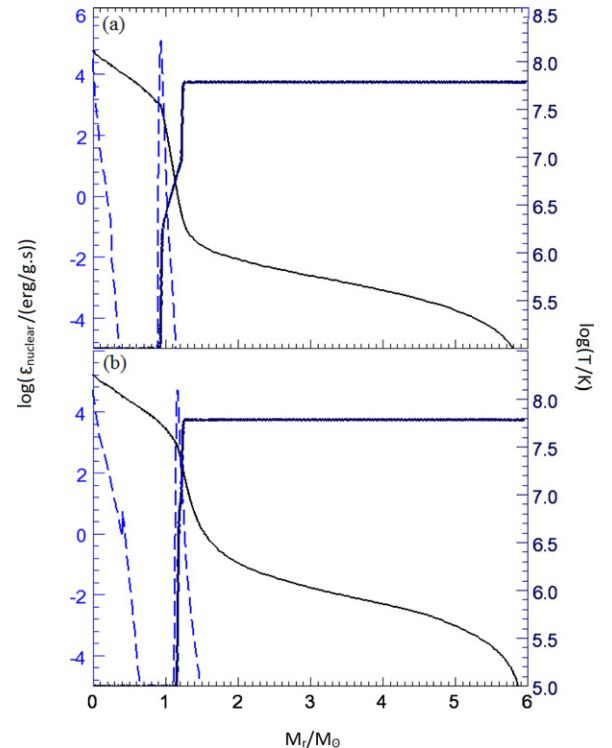


Figure 11. Same as Figure 7, obtained with the *C*-rate. Panels (a) and (b) are taken at points 1 and 3 shown in Figure 9, respectively.

(A color version of this figure is available in the online journal.)

the lower *C*-rate. What happens is that a less efficient shell H-burning causes a less vigorous expansion of the layers above the shell source which leads to a larger radius on the RGB compared to the case with the *N*-rate as shown in Figure 10 for the $6 M_{\odot}$ star. As a consequence, envelope convection does not penetrate as deep in mass as in the case with the *N*-rate.

This is seen by comparing Figure 11 with Figure 7. At point 1 marked in Figures 6(a) and 9(a), the H-discontinuity is located at $M_r = 1.15 M_{\odot}$ with the *N*-rate and at $M_r = 1.23 M_{\odot}$ with the *C*-rate as shown in Figures 7(a) and 11(a), respectively. Consequently, shell H-burning in the latter case cannot reach the H-profile in order to strengthen the shell H-burning until toward the end of core He-burning (cf. Figure 9(b)). Thus, despite the similar temperature profiles encountered in the H-shell region prior to the loop formation (cf. Figures 7(a) and 11(a)), the shallower H-profile obtained with the *C*-rate

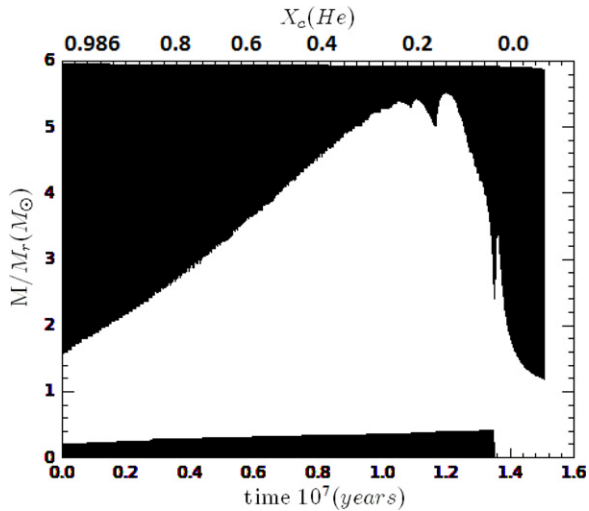


Figure 12. Convective structure during core helium burning calculated with the *C-rate*. The envelope remains partially convective for this sequence. Time is set to zero at the end of core hydrogen burning, and the models are plotted until $t = 1.5 \times 10^7$ yr.

prohibits the strengthening of shell H-burning, and the blue loop is suppressed. Consequently, the envelope does not contract, which entails the steeply declining temperature profile achieved in the shell region shown in Figure 11, and therefore, the envelope remains partially convective as shown in Figure 12.

Summarizing these results, we find that with the higher N14 rate, strong shell H-burning causes the envelope to expand to a larger radius on the RGB. As a consequence, convection in the envelope penetrates deeper in mass during the FDUP as compared with a relatively weaker H-shell source. The resulting position of the H-profile, as mainly determined by the N14 rate, influences the behavior of the shell source during the ensuing evolution, and consequently, the extension of the blue loop.

3.4. Evolutionary Sequence with the *L-rate*

Using the N14 rate of the LUNA collaboration, which we call the *L-rate*, we analyze the behavior of the sequence of the $6 M_{\odot}$ star and compare it to the cases discussed earlier. The left panel of Figure 13 displays the evolutionary track in the HRD during core helium burning, with a severely reduced blue loop in contrast to the one obtained with the *N-rate* (cf. Figure 6(a)), but similar to that obtained with the *C-rate*. As Figure 13 indicates,

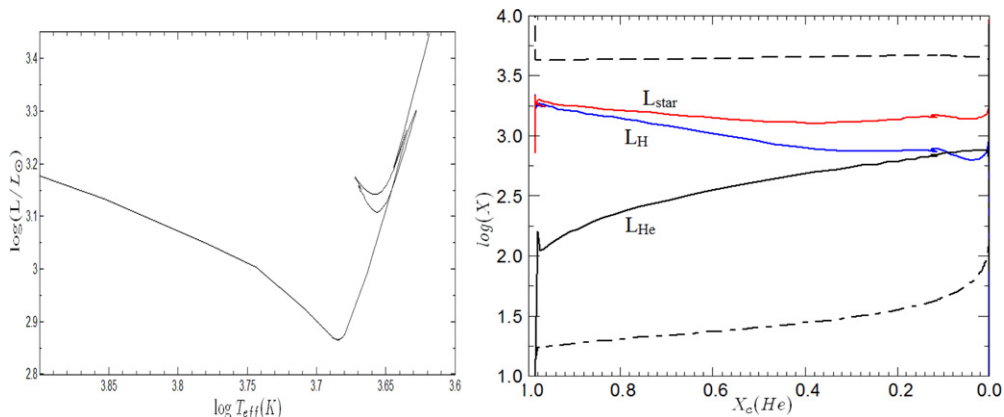


Figure 13. Same as Figure 5, obtained with the *L-rate*.

(A color version of this figure is available in the online journal.)

this case is similar to that with the *C-rate*: the shell H-burning is not reinforced, and thus, no extended or nearly inhibited loop.

The H-discontinuity in this case is located at $M_r = 1.225 M_{\odot}$ after the FDUP, which consistently lies between the values we have obtained for the *N-rate* ($M_r = 1.15 M_{\odot}$) and the *C-rate* ($M_r = 1.23 M_{\odot}$). Being very close to the value obtained with the *C-rate* explains the similarity with the results of Section 3.3.

3.5. Dependence of the Blue Loop on the Stellar Mass

As evident in Figures 3–5, the blue loops of stars of masses $8 M_{\odot}$ and above are barely affected by changing the N14 rate. In contrast, the blue loops of stars in the mass range $5–7 M_{\odot}$ are significantly affected by this modification. To explain this difference, we point out two important features: (1) the location in mass of the H-discontinuity and (2) the temperature profile achieved in the proximity of the H-discontinuity where shell H-burning proceeds.

To see how these two factors are related in determining the loop properties as a function of stellar mass, we analyze the results presented in Figure 14. These snapshots, which are obtained using the *C-rate*, are taken at the bottom of the RGB for stars of masses $5 M_{\odot}$, $6 M_{\odot}$, and $10 M_{\odot}$, i.e., prior to the loop formation (see position 2 in Figure 6(a) for example). The figures show, as a function of the interior mass, the H-profile, the temperature profile, and the profile of the energy generation rate in the H-shell region.

In the case of the $5 M_{\odot}$ star (the lower boundary of our considered mass range), the H-discontinuity is located deep in mass, where the region above the discontinuity comprises about 81% of the total stellar mass. Therefore, the H-shell source encounters a relatively high hydrogen abundance in the region where the temperature is in excess of 2×10^7 K, which makes the CNO burning efficient enough to trigger the blue loop in this case.

In the case of the $6 M_{\odot}$ star, the situation is different. We found that the region above the discontinuity comprises about 79% of the total stellar mass. Therefore, the discontinuity is located further out in mass as compared to the $5 M_{\odot}$ star, and consequently, the temperature drops below 2×10^7 K at the discontinuity. The net effect is that shell H-burning is not strong enough with the relatively weaker *C-rate* to trigger an extended loop (see Figures 5 and 9(a)).

In the case of the $10 M_{\odot}$ star (Figure 14(c)), the temperature profile in the H-shell exceeds 2×10^7 K in the whole mass range comprising the hydrogen gradient up to the H-discontinuity.

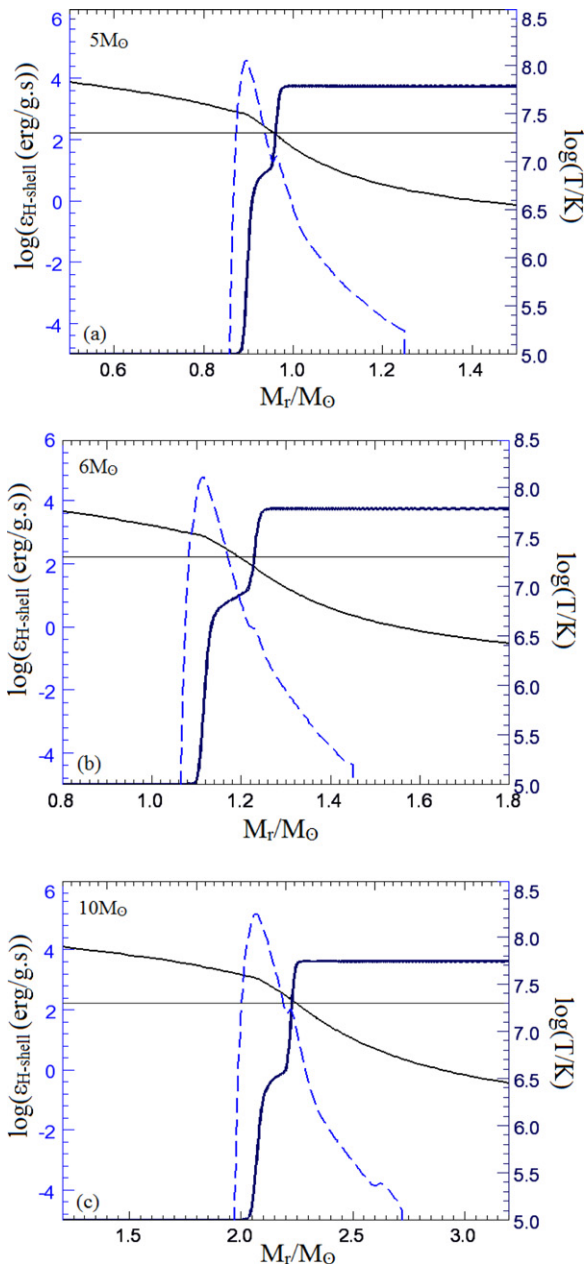


Figure 14. Snapshots of the temperature profile, hydrogen profile, and the energy generation rate in the hydrogen burning shell at the bottom of the RGB are shown for the three stellar masses calculated with the *C-rate*: (a) $5 M_{\odot}$, (b) $6 M_{\odot}$, and (c) $10 M_{\odot}$. The horizontal line marks $T = 2 \times 10^7$ K at which the H-burning becomes efficient. Note that the hydrogen abundance has been shifted upward ($4X_c(\text{H}) + 5$) in order to match the scale of the right side axis. (A color version of this figure is available in the online journal.)

Consequently, shell H-burning is strong enough to trigger an extended blue loop, as is the case for all the stars in the upper mass range ($9 M_{\odot}$ and above).

3.6. Evolutionary Sequence with Envelope Overshooting

If the *C-rate* is taken at face value, then an undesirable situation arises, namely, the shortened blue loops fail to explain the δ -Cepheids and yellow giants observed in the considered mass range.

One possibility to restore the extension of blue loops is to invoke envelope overshooting, which places the H-discontinuity deeper in the star, i.e., closer to the H-shell source. This is

demonstrated in the following in the case of a $6 M_{\odot}$ star. We have recalculated the evolution of this star with the *C-rate*, but with including exponential overshooting beyond the convective boundary as obtained with the Schwarzschild criterion. Convective mixing is treated by solving the diffusion equation; see El Eid (1995):

$$\frac{dX_i}{dt} = \frac{\partial}{\partial M_r} \left[(4\pi r^2 \rho)^2 D \frac{\partial X_i}{\partial M_r} \right].$$

In the layers immediately below the convective envelope, the diffusion coefficient D appearing in the above equation is calculated according to the work by Freytag et al. (1996)

$$D(z) = D_o e^{-\frac{2z}{fH_p}} \quad z = |r_{\text{boundary}} - r|,$$

where D_o is the diffusion coefficient at the bottom of the convective envelope. Within this framework, $D(z)$ is exponentially decreasing as a function of geometric distance. The quantity f is a free parameter, chosen to be 0.25 as suggested by Freytag et al. (1996), and H_p is the pressure scale height. We find that an overshooting distance of $0.2H_p$ is sufficient to restore the loop as demonstrated in Figure 15. This is in accordance with works like Stothers & Chin (1991), who find that for stars of masses between $5 M_{\odot}$ and $15 M_{\odot}$, an overshooting of about $0.3H_p$ is sufficient to promote blue loops in models that would otherwise lack them.

The issue of blue loops is more complicated when core overshooting is considered. Preliminary results indicate that the loop properties are influenced not only by the efficiency of core overshooting but also on how this overshooting modifies the temperature distribution in the shell region, which cannot be discussed independently of the stellar mass. Indeed, this issue is not overlooked, but it rather deserves a separate investigation which extends beyond the scope of this work. The detailed results will be presented in a forthcoming paper.

4. COMPARISON WITH OBSERVATIONS

A useful parameter that enables a comparison of the loop properties with observations is the ratio τ_b/τ_r , which characterizes the core helium-burning evolutionary time spent during the loop on the blue side to that on the red side of the HRD. This ratio is obtained by taking the dividing temperature at $\log T_{\text{eff}} = 3.7$ which corresponds to the classification of the giants between G and K spectral classes (Lai & Li 2011). This ratio is useful because it can be associated with the observed number ratio of blue to red giants in clusters N_b/N_r . Such a link has been used in previous works (Stothers 1991; El Eid 1995; Langer et al. 1995; Lai & Li 2011).

Our present results for the ratio τ_b/τ_r are given in Table 1 for the stars in the mass range (5–12) M_{\odot} , for the *N-rate* and the *C-rate*. The results obtained with envelope overshooting are also included. Table 1 shows the following features.

1. The ratio τ_b/τ_r is found to be a steadily increasing function of the stellar mass in the considered mass range, except for the $6 M_{\odot}$ with the *C-rate* where the loop is suppressed.
2. The effect of using the *C-rate* is a systematic reduction in the τ_b/τ_r ratio mostly in the mass range (5–10) M_{\odot} , while this ratio is only slightly affected by the *C-rate* in masses above $10 M_{\odot}$ due to the high temperatures achieved in these stars in the proximity of the H-discontinuity as we have described earlier in Section 3.5.

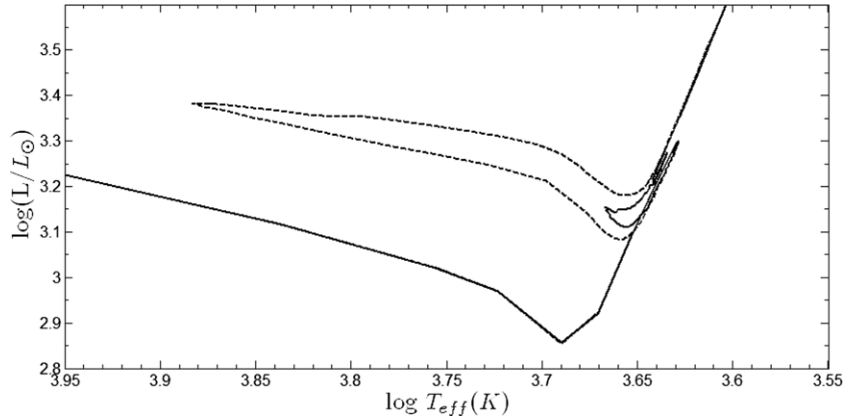


Figure 15. Illustration of the effect of moderate envelope overshooting on the blue loop formation and extension. Solid line: the evolutionary track of a $6 M_{\odot}$ calculated with the *C-rate* without any overshooting at the bottom of the convective envelope, the loop is almost completely suppressed. Dotted line: the same evolutionary sequence, when envelope overshooting is applied (see the text). Note how the extension of the loop is restored.

Table 1

Model Properties of the Evolutionary Sequences Investigated in this Work

M_i (M_{\odot})	<i>N-rate</i>			<i>C-rate</i> (without OV)			<i>C-rate</i> (with OV)		
	τ_b/τ_r	M_{α}^1	M_{α}^2	τ_b/τ_r	M_{α}^1	M_{α}^2	τ_b/τ_r	M_{α}^1	M_{α}^2
5	0.39	0.586	0.967	0.19	0.587	0.966	0.41	0.587	0.971
6	0.40	0.714	1.197	0.00	0.710	1.171	0.44	0.709	1.214
7	0.59	0.860	1.474	0.07	0.858	1.425	0.50	0.860	1.461
8	0.79	1.017	1.747	0.41	1.012	1.732	0.72	1.012	1.753
9	0.89	1.193	2.025	0.54	1.187	2.021	0.81	1.187	2.033
10	1.06	1.391	2.329	0.66	1.385	2.304	0.98	1.385	2.331
11	1.20	1.599	2.631	1.36	1.593	2.642	1.64	1.593	2.637
12	3.39	1.820	2.954	3.41	1.798	2.945	3.88	1.790	2.992

Notes. The masses M_{α}^1 and M_{α}^2 denote the helium core masses at core helium ignition and exhaustion, respectively. OV denotes envelope overshooting.

3. Our experiment with envelope overshooting (see Table 1) was successful in achieving values of τ_b/τ_r close to those with the *N-rate*. This comparison deserves more extended observational studies and detailed theoretical analysis for a better assessment. However, we can ascertain that even a moderate amount of envelope overshooting can restore the extension of the blue loop in the mass range where it is mostly inhibited, and also affects τ_b/τ_r ratios.

The direct comparison between the τ_b/τ_r ratio and the observed number ratio N_b/N_r is not easy because such observations are subject to large uncertainties that are mainly due to the lack of observations of obscured faint red giants. Therefore, we shall not expect a very precise agreement between the observed N_b/N_r and the theoretical τ_b/τ_r . The observed ratio by Stothers (1991) is $N_b/N_r = 1.7 \pm 0.4$ for young clusters. Carson & Stothers (1976) found values of 0.33 and 1.0 for middle-aged clusters and young clusters for the two age groups of masses roughly $5 M_{\odot}$ and $7 M_{\odot}$, respectively. Harris (1976) found a value of 0.55 for source-correlated initial masses close to $5 M_{\odot}$. This agrees with the models calculated with the *C-rate* with an envelope overshooting distance of $0.2 H_p$.

Another way to verify the predictions of our theoretical models is the observed location of the Cepheid instability strip in the HRD. Figure 16 shows the evolutionary tracks of our considered models as well as observations of 17 yellow giants and supergiants and 9 Cepheids in the open Galactic clusters by Schmidt (1984). We also

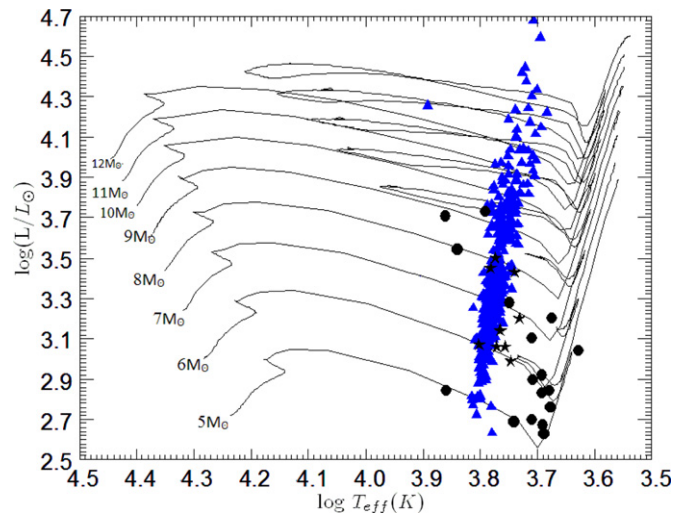


Figure 16. H-R diagrams for stellar models of mass 5–12 M_{\odot} obtained with the *C-rate*. The triangles denote the observed Galactic Classical Cepheids by Fernie et al. (1995). Observations by Schmidt (1984) are indicated by asterisks and closed circles which represent Cepheid stars and yellow giants in open clusters, respectively.

(A color version of this figure is available in the online journal.)

show observed Cepheids by Fernie et al. (1995) as listed in the David Dunlap Observatory’s online Galactic classical Cepheids database. In order to obtain the effective temperatures and luminosities, we perform the transformations as suggested by Lai & Li (2011), according to the following formulae: for the luminosity, we use the period–luminosity relation $\log(L/L_{\odot}) = 2.43 + 1.179(\log P)$ (Gieren et al. 1989) and the effective temperatures are calculated by $\log T_{\text{eff}} = 3.886 - 0.175(B - V)_o$ where $(B - V)_o$ is the intrinsic color index. Figure 16 shows that the severely shortened loops of the $5 M_{\odot}$, $6 M_{\odot}$, and $7 M_{\odot}$ with the *C-rate* cannot explain the observed data. However, when envelope overshooting is taken into account as described in Section 3.6, the models $5 M_{\odot}$, $6 M_{\odot}$, and $7 M_{\odot}$ restore their loops as required to explain the observations as shown in Figure 17.

5. CONCLUDING REMARKS

The evolution of stars in the mass range 5–12 M_{\odot} has been presented. These stars are known to develop blue loops after

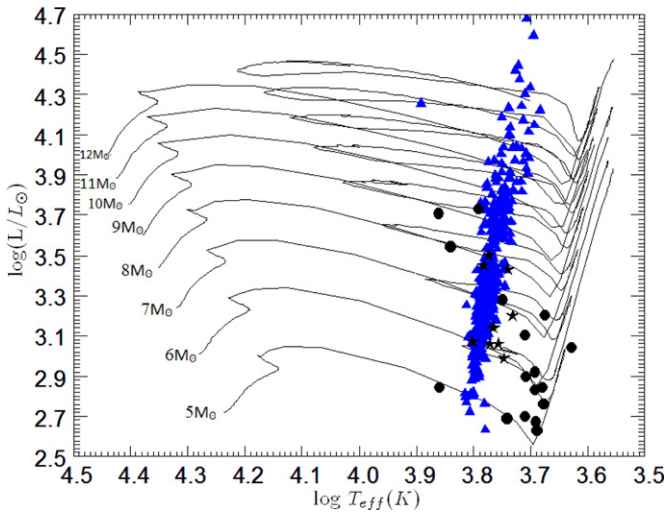


Figure 17. Same as Figure 16, but with envelope overshooting applied over a distance of $0.2H_p$. Note how the predicted temperature range of the tracks of the $5 M_{\odot}$, $6 M_{\odot}$, and $7 M_{\odot}$ models now agrees with those of the observed Cepheids and yellow giants.

(A color version of this figure is available in the online journal.)

the onset of core helium burning on the RGB. Such loops are required to explain the observed Cepheid stars and the yellow giants. Several works note the sensitivity of the blue loops to the N14 rate; however, its pronounced effect on a wide mass range is presented for the first time, which provides an insight into the behavior of the blue loop as a function of the stellar mass.

In this work, we found that the $^{14}\text{N}(p, \gamma)^{15}\text{O}$ rate has a strong impact on the blue loops in the mass range $5\text{--}8 M_{\odot}$. An appreciably reduced NACRE rate proposed on experimental ground can lead to a severe suppression of the blue loop. We have identified two effects of the $^{14}\text{N}(p, \gamma)^{15}\text{O}$ rate: one is the influence of this rate on the depth of the H-discontinuity during the FDUP on the RGB *prior* to the loop phase, and the other effect is its impact on the efficiency of shell H-burning *during* this phase. These two effects are acting differently depending on the stellar mass range.

1. In the case of stellar masses below $5 M_{\odot}$, convection in the envelope creates an H-profile that is deep enough in mass, but the temperatures in the layers of shell H-burning are not high enough to reinforce the shell. The evolutionary track thus remains close to the RGB and no extended loop is formed. Thus, a modified N14 rate will not change this conclusion.
2. In the case of stellar masses between $5 M_{\odot}$ and $8 M_{\odot}$, the situation is entirely different. The location of the H-discontinuity created by the envelope convection and the temperatures achieved in the region of the H-discontinuity are both crucial in determining the formation and extension of the loop. The effect of the N14 rate is most pronounced in this mass range and its efficiency plays a decisive role here because the temperatures in the proximity of the H-discontinuity are not as high as those in stars of masses above $8 M_{\odot}$. Moreover, the less efficient shell H-burning with the weak *C-rate* causes an insufficient expansion of the envelope on the RGB, which results in a less deep H-profile. The combined effect of these factors causes a severely reduced loop.
3. In the case of stellar masses above $8 M_{\odot}$, the N14 rate has a marginal influence because the shell source is strong

enough owing to the high temperature encountered in the neighborhood of the H-discontinuity in these stars to initiate a well-extended loop.

A final remark is that in our calculation, we have tested both the *C-rate* and the *L-rate*. Both rates independently suggest a reduction in the *N-rate*, particularly the *C-rate*, which represents an updated evaluation (described in Section 2.2). We emphasize that the N14 rate is a key reaction in this context and needs to be better constrained experimentally, which leaves this issue open for further investigation. In addition, if this rate would be less efficient by about a factor of two compared to the evaluation by NACRE (see Section 2.2), then one way to recover the blue loops is by introducing moderate envelope overshooting during the RGB. We could show that the efficiency of this rate cannot be decoupled from the physical conditions in the shell region which are also influenced by convection. Therefore, obtaining an experimentally established N14 rate helps to determine the efficiency of hydrogen burning and to constrain the role and efficiency of convective overshooting. Moreover, core overshooting should be investigated in this context due to its remarkable effects on the loop properties. Indeed, stellar evolution conceals surprises which call for a careful treatment of all its conditions, and renders its astrophysical context rather challenging.

G.H. and M.E. thank the American University of Beirut (AUB) for supporting their research work. G.H. is thankful for the support she has received from the Dean's office of the Faculty of Arts & Sciences at AUB that allowed her to present the current results in international conferences. She also thanks the IT Unit at the Faculty of Engineering & Architecture for the technical support and generous allocation of computer time, as well as the Center of Advanced Mathematical Physics (CAMPS) at AUB, for using their computation facilities. G.H. also wishes to thank the anonymous referee for the insightful comments and B. Eberhardt for the valuable technical support in preparing the manuscript. This work was also supported in part by the CNRSL under the grant number 111150-522276.

REFERENCES

- Adelberger, E. G., García, A., Robertson, R. G. H., et al. 2011, *Rev. Mod. Phys.*, **83**, 195A
- Alongi, M., Bertelli, G., Bressan, A., & Chiosi, C. 1991, *A&A*, **244**, 95
- Angulo, C., Arnould, M., Rayet, M., et al. 1999, *Nucl. Phys. A*, **656**, 3A
- Angulo, C., Champagne, A. E., & Trautvetter, H.-P. 2005, *Nucl. Phys. A*, **758**, 391c
- Artemov, S. V., Igamov, S. B., Tursunmakhatov, Q. I., et al. 2012, *Phys. At. Nucl.*, **75**, 291
- Bemmerer, D., Confortola, F., Lemut, A., et al. 2006, *Nucl. Phys. A*, **779**, 297
- Bertone, P. F. 2010, PhD thesis, Univ. North Carolina–Chapel Hill
- Borowski, M., Lieb, K. P., Uhrmacher, M., & Bolse, W. 2009, in AIP Conf. Proc. 1090, Capture Gamma-ray Spectroscopy and Related Topics, ed. J. Jolie, A. Blazhev, & N. Warr (Melville, NY: AIP), 450
- Carson, T. R., & Stothers, R. 1976, *ApJ*, **204**, 461
- Cassisi, S., Salaris, M., & Bono, G. 2002, *ApJ*, **565**, 1231
- Cyburt, R. H., Amthor, A. M., Ferguson, R., et al. 2010, *ApJS*, **189**, 240
- El Eid, M. F. 1995, *MNRAS*, **275**, 983
- El Eid, M. F., The, L.-S., & Meyer, B. 2004, *ApJ*, **611**, 452
- El Eid, M. F., The, L.-S., & Meyer, B. 2009, *Space Sci. Rev.*, **147**, 1
- Evans, N. R. 1993, *AJ*, **105**, 1956
- Fernie, J. D., Evans, N. R., Beattie, B., & Seager, S. 1995, *IBVS*, **4148**, 1
- Formicola, A., Imbriani, G., Costantini, H., et al. 2004, *Phys. Lett. B*, **591**, 61
- Freytag, R., Ludwig, H., & Steffen, M. 1996, *A&A*, **313**, 497
- Gieren, W. P., Barnes, T. G., III, & Moffett, T. J. 1989, *ApJ*, **342**, 467
- Harris, G. L. H. 1976, *ApJS*, **30**, 451
- Iliadis, C. 2007, *Nuclear Physics of Stars* (Weinheim: Wiley)
- Imbriani, G., Costantini, H., Formicola, A., et al. 2005, *Eur. Phys. J. A*, **25**, 455

- Kippenhahn, R., & Weigert, A. 1990, *Stellar Structure and Evolution* (Berlin: Springer)
- Lai, X. J., & Li, Y. 2011, *Res. Astron. Astrophys.*, **11**, 1351
- Langer, N., & Maeder, A. 1995, *A&A*, **295**, 685
- Lemut, A., Bemmeer, D., Confortola, F., et al. 2006, *Phys. Lett. B*, **634**, 483
- Marta, M., Formicola, A., Bemmeer, D., et al. 2011, *Phys. Rev. C*, **83**, 045804
- Matraka, B., Wassermann, C., & Weigert, A. 1982, *A&A*, **107**, 283
- Mermilliod, J. C. 1981, *A&AS*, **44**, 467
- Neilson, H. R., Cantiello, M., & Langer, N. 2011, in *ASP Conf. Ser. 448*, 16th Cambridge Workshop on Cool Stars, Stellar Systems, and the Sun, ed. C. M. Johns-Krull, M. K. Browning, & A. A. West (San Francisco, CA: USA), 155
- Reimers, D. 1975, *Mem. Soc. R. Sci. Liege*, **8**, 369
- Runkle, R. C., Champagne, A. E., Angulo, C., et al. 2005, *Phys. Rev. Lett.*, **94**, 082503
- Schmidt, E. G. 1984, *ApJ*, **287**, 261
- Schröder, U., Becker, H. W., Bogaert, G., et al. 1987, *Nucl. Phys. A*, **467**, 240
- Stothers, R. B. 1991, *ApJ*, **383**, 820
- Stothers, R. B., & Chin, C. W. 1991, *ApJ*, **374**, 288
- Valle, G., Marconi, M., Degl'Innocenti, S., & Prada Moroni, P. G. 2009, *A&A*, **507**, 1541
- Weiss, A., Serenelli, A., Kitsikis, A., Schlattl, H., & Christensen-Dalsgaard, J. 2005, *A&A*, **441**, 1129
- Xu, H. Y., & Li, Y. 2004, *A&A*, **418**, 213

Appendix 3



Exploring Masses and CNO Surface Abundances of Red Giant Stars

Journal:	<i>Monthly Notices of the Royal Astronomical Society</i>
Manuscript ID:	Draft
Manuscript type:	Main Journal
Date Submitted by the Author:	September 29, 2014
Complete List of Authors:	Halabi, Ghina; Mounib El Eid; American University of Beirut, Physics
Keywords:	convection < Physical Data and Processes, nuclear reactions, nucleosynthesis, abundances < Physical Data and Processes, stars: abundances < Stars, stars: evolution < Stars, stars: low-mass < Stars, colours, luminosities, masses, radii, temperatures, etc.)

Exploring Masses and CNO Surface Abundances of Red Giant Stars

Ghina M. Halabi and Mounib El Eid

Department of Physics, American University of Beirut, Beirut, Lebanon

ABSTRACT

We present a grid of evolutionary sequences for stars in the mass range $1.2 - 7M_{\odot}$, having solar-like initial composition. We focus on this mass range in order to estimate the masses and obtain the CNO surface abundances of a sample of observed red giants. The stellar models are calculated from the zero-age main sequence till the early asymptotic giant branch (AGB) phase. Stars of masses $\leq 2.2M_{\odot}$ are evolved including the core helium flash. In the present work, we adopt an approach that improves the mass determination of an observed sample of 21 RGB and early AGB stars. This approach is based on matching the observationally derived effective temperatures and absolute magnitudes to the calculated values based on our evolutionary tracks in the HR diagram. In addition, we compare the calculated surface CNO abundances with the observationally inferred values in order to improve the treatment of convective mixing. The main results of this work are that a more reliable determination of the masses should be based on evolutionary tracks extended to the range of observation, and explaining the observational CNO surface abundances requires extra mixing beyond the boundary obtained by the Schwarzschild criterion. We also show the effect of recent determinations of proton capture reactions and their uncertainties on the $^{16}\text{O}/^{17}\text{O}$ and $^{14}\text{N}/^{15}\text{N}$ ratios. In particular, we find that the $^{14}\text{N}(p, \gamma)^{15}\text{O}$ reaction is not only important in the context of blue loops but also in predicting the $^{14}\text{N}/^{15}\text{N}$ ratio in red giants.

Subject headings: nuclear reactions, nucleosynthesis, abundances - stars: evolution - stars: low-mass

1. Introduction

After the main sequence phase, stars evolve towards the red giant branch (RGB) at the end of core H-burning. This evolution is initiated by the ignition of shell H-burning surrounding the He core, whose energy flux leads the envelope to expand and the star evolves to the RGB. This expansion increases the opacity and leads to the development of a deep convective envelope. This is called the first dredge up (FDUP), where envelope convection mixes up the products of the H-burning to the surface. This is the first event that alters the surface composition of the star.

In the mass range $4-7M_{\odot}$, stars exhibit blue loops at the beginning of core He burning (Halabi et al. (2012) and references therein). The main phase of core He-burning is completed before the track loops back to the RGB. This leads again to the deepening of envelope convection. For solar metallicity stars of masses above $\gtrsim 4M_{\odot}$, a second dredge up (SDUP), can reach deeper regions, which introduces further changes in the surface abundances. This work focuses on the evolution of stars as they evolve to the early asymptotic giant branch (AGB) stage, including detailed analysis of these two dredge up events.

The main goal of the present work is to use the observations obtained for a sample of red giants by Tsuji (2008), hereafter Tsuji08, in order to achieve two goals: (a) to estimate the masses of these observed giants by matching their observationally derived effective temperatures and bolometric magnitudes to the values obtained from the evolutionary tracks in the HR diagram. This is possible since the stars are not pulsating Mira variables (see section 4 for details). We are able to improve the mass determination done by Tsuji08 by using more extended evolutionary tracks to avoid the extrapolation that he partially relied on to determine the mass of some giants, (b) to compare the calculated CNO abundances of these models to the abundances inferred from observations.

A large body of observational data is available for the surface CNO abundances in RGB stars (Lambert & Reis 1981; Harris & Lambert 1984a,b; Harris et al. 1988; Lambert et al. 1986; Gilroy & Brown 1991; Tsuji 1991; Charbonnel 1994; Tsuji 2008; Tautvaišienė et al. 2010; Piau et al. 2011). These data provide a powerful tool to get insight into the internal structure of evolved stars. In particular, comparing the calculated oxygen and nitrogen abundances with the observed data seems to be very useful to improve the treatment of convective mixing in the stellar interiors (see section 5). Our results suggest extra mixing below the edge of the convective envelope as determined by the Schwarzschild criterion in order to achieve a better agreement with observations. This extra mixing has been suggested in several investigations in connection with the evolution of field giants (Charbonnel & Do Nascimento 1998; Gratton et al. 2000), open clusters (Luck 1994; Tautvaišienė et al. 2000, 2005), globular clusters (Shetrone 2003; Pilachowski et al. 2003; Recio-Blanco & de Laverny 2007; Denissenkov et al. 2014) as well as to explain isotopic ratios in pre-solar grains (Palmerini et al. 2011, 2013; Busso et al. 2014). The ^{17}O abundance profile inside the star is of particular interest. This is because this isotope is produced by the ON-cycle which requires higher temperatures than the CN-cycle. Therefore, the ^{17}O profile exhibits a steep gradient within the central region of the star, at the position of maximum convective penetration (shown later in Fig. 8). This renders the surface abundance of ^{17}O sensitive to the depth of convective mixing, stellar mass and to the nuclear reaction rates involved in the CNO cycle (El Eid 1994). We show in Section 5 how $^{16}\text{O}/^{17}\text{O}$ ratio is useful to constrain the depth of extra-mixing. The $^{12}\text{C}/^{13}\text{C}$, however, remains unsettled in our models and the very low observational ratios are not explained by our extra-mixing treatment. Other non-standard mixing mechanisms may need to be invoked as we shall mention in Section 5. Ramstedt & Olofsson (2014) also discuss $^{12}\text{C}/^{13}\text{C}$ ratios in AGB stars in connection with their recent estimations of circumstellar $^{12}\text{CO}/^{13}\text{CO}$ abundance ratios based on radiative transfer analysis of radio line emission observations.

Concerning nuclear reaction rates, there has been extensive experimental work recently on updated determinations of major reaction rates, including those of the CNO cycle. Significant improvements were introduced and the evaluation of these rates included updated nuclear physics input. One set of these determinations that we use (Sergi et al. 2014) was obtained using the Trojan Horse method (La Cognata et al. 2010), which is an indirect technique that is able to provide more reliable reaction rate cross-sections at low temperatures where measurements in the astrophysical energy range are available. Other sets, obtained by Sallaska et al. (2013) and Iliadis et al. (2010) are evaluated based on Monte Carlo techniques (Longland et al. 2010). This method provides a median rate which -under certain conditions- resembles the commonly referred to "recommended" rate, as well as a low rate and a high rate which, unlike the "upper" and "lower" limits of classical rates, have well-defined statistical meaning. We also show the effect of the $^{14}\text{N}(p, \gamma)^{15}\text{O}$ rate (as used in Halabi et al. (2012)) in comparison to NACRE (Angulo et al. 1999) on the nitrogen isotopic ratios in low and intermediate mass stars. We study the effect of these recent determinations, particularly the proton capture reactions, on the isotopic ratios $^{16}\text{O}/^{17}\text{O}$ and $^{14}\text{N}/^{15}\text{N}$.

This paper is organized as follows. In Section 2, we describe our calculations. Our evolutionary results are presented in Section 3. Mass determinations, as well as a summary of the observational data that we used in this work and comparison with previous works are provided in Section 4. Section 5 describes our results concerning surface abundance profiles and the effects of extra mixing. The effect of nuclear reaction rates is discussed in Section 6. Section 7 provides our concluding remarks.

2. Model Calculations

The evolutionary sequences presented in this work are obtained using the stellar evolution code HYADES as described in El Eid et al. (2009), with recent modifications as outlined in Halabi et al. (2012). This code is a one-dimensional implicit Lagrangian code based on a hydrodynamical method which solves the stellar structure equations on an adaptive grid. In connection with the present work, we add some comments concerning the mass-loss by stellar wind and convective mixing.

2.1. Treatment of mass-loss

Mass-loss by stellar wind has an important effect on the evolution of stars, and thus, requires a suitable treatment. Mass-loss rates are included in the present calculation using semi-empirical mass loss rates adjusted to the global parameters of the stars. In particular, we adopt the mass loss rates according to a Mira pulsation period (P) suggested by Vassiliadis & Wood (1992):

$$\log(P/\text{days}) = -2.07 - 0.9 \times \log\left(\frac{M_{ZAMS}}{M_{\odot}}\right) + 1.94 \times \log\left(\frac{R}{R_{\odot}}\right) \quad (1)$$

For $P < 100$ days, we adopt the widely used mass loss rate suggested by Reimers (1975), given by

$$\dot{M}_R = \eta \times 4 \times 10^{-13} \times \frac{LR}{M} \quad (2)$$

where L , R and M are the luminosity, radius and mass, respectively, in solar units, and η is a free parameter taken to be 1, which means effective mass-loss. Reimer’s formula is used throughout the core He-burning phase. For $100 < P < 500$ days we use a more effective rate according to Bowen (1988):

$$\dot{M}_B = \dot{M}_R \times 4.83 \times 10^{-9} \left(\frac{M_{ZAMS}}{M_\odot} \right)^{-2.1} \left(\frac{L}{L_\odot} \right)^{2.7} \quad (3)$$

If $P > 500$ days, we use the superwind mass-loss rate during the AGB using the formula suggested by Vassiliadis & Wood (1992)

$$\dot{M}_V = \frac{L}{3 \times 10^8 \times v_{exp}} \frac{3.15576}{M_\odot} \quad (4)$$

where v_{exp} is the stellar wind expansion velocity given by

$$v_{exp} = -13.5 + 0.056 \times P \quad (5)$$

In order to test our treatment of the mass-loss rate, we show in Fig. 1 these rates as a function of the Mira pulsation period in case of our evolutionary sequence of the $3M_\odot$ star, together with the observed mass-loss rates obtained from several works. Despite the scatter in the data, two regions can be clearly identified, a region of moderate mass-loss rate up to $\log P = 2.5$, and a more effective mass-loss rate for $\log P > 2.5$. The mass-loss rates we have used are indicated with black dots, and appear to be reasonably consistent with observations in the two mass-loss regimes.

2.2. Convective mixing

Commonly, the extension of a convective zone is determined by the Schwarzschild criterion. However, the edge of the of a convective zone is not strictly fixed by this criterion, because of the assumed abrupt transition between the convective and radiative regions. This is a crucial and long-standing problem in stellar modelling. The hydrodynamical simulations by Freytag et al. (1996) suggest that the convective boundary can be extended in terms of an exponentially decaying diffusion coefficient:

$$D(z) = D_o e^{\frac{-2z}{fH_p}} \quad z = |r_{\text{boundary}} - r|, \quad (6)$$

where D_o is the diffusion coefficient at the edge of the convective envelope and can be obtained from the Mixing Length Theory (see Langer et al. (1985)). The quantity f is a free parameter, chosen to be 0.25 as suggested by Freytag et al. (1996), and H_p is the pressure scale height. With this

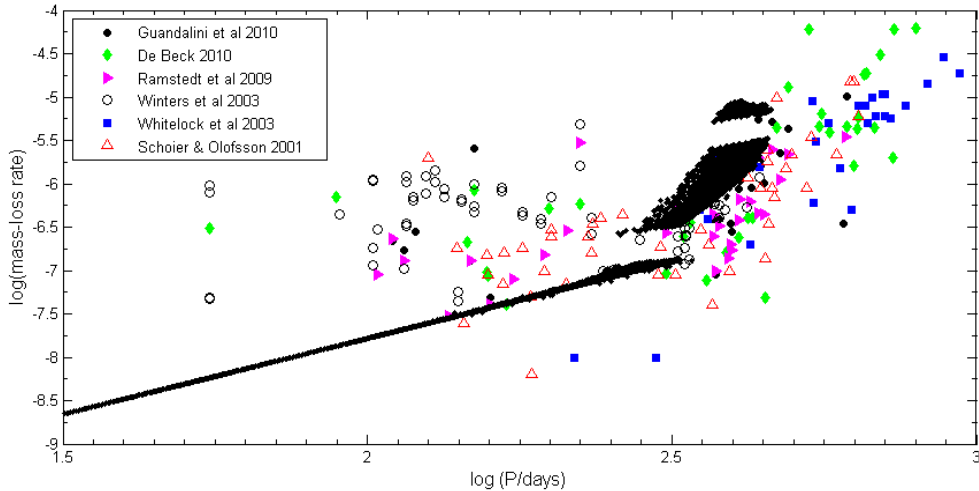


Fig. 1.— The mass-loss rates of a $3M_{\odot}$ model vs. the Mira pulsational period as compared to the observed mass-loss rates labeled in the upper left panel. The mass-loss rate expected by our calculation is consistent with the two mass-loss regimes experienced by these giants. See text for more details.

description, $D(z)$ is exponentially decreasing as a function of geometric distance z . This treatment of extra-mixing, or overshooting, is used to mix chemical elements beyond the edge of the convective zone by solving the diffusion equation:

$$\frac{dX_i}{dt} = \frac{\partial}{\partial M_r} [(4\pi r^2 \rho)^2 D \frac{\partial X_i}{\partial M_r}] \quad (7)$$

where r is the radius, ρ is the density and D is as given in Eq. 6. In Sect. 5.3, we give details of the present calculations with this extra mixing.

3. Evolutionary Results

3.1. Evolutionary tracks

Fig. 2 shows the evolutionary tracks of stars in the mass range $(1.2 - 7.3)M_{\odot}$. These sequences were calculated from the zero-age main sequence up to the early AGB phase. In this figure, stars of masses $\geq 2.5M_{\odot}$ exhibit blue loops starting at the onset of central helium burning. These loops become more extended in masses $\gtrsim 4M_{\odot}$. A detailed discussion of this evolutionary phase can be found in Halabi et al. (2012). Stars of masses $\leq 2.2M_{\odot}$ and solar-like initial composition evolve through the core He-flash (see Kippenhahn & Weigert (1990) for a basic description). We describe this phase in some detail in the following section.

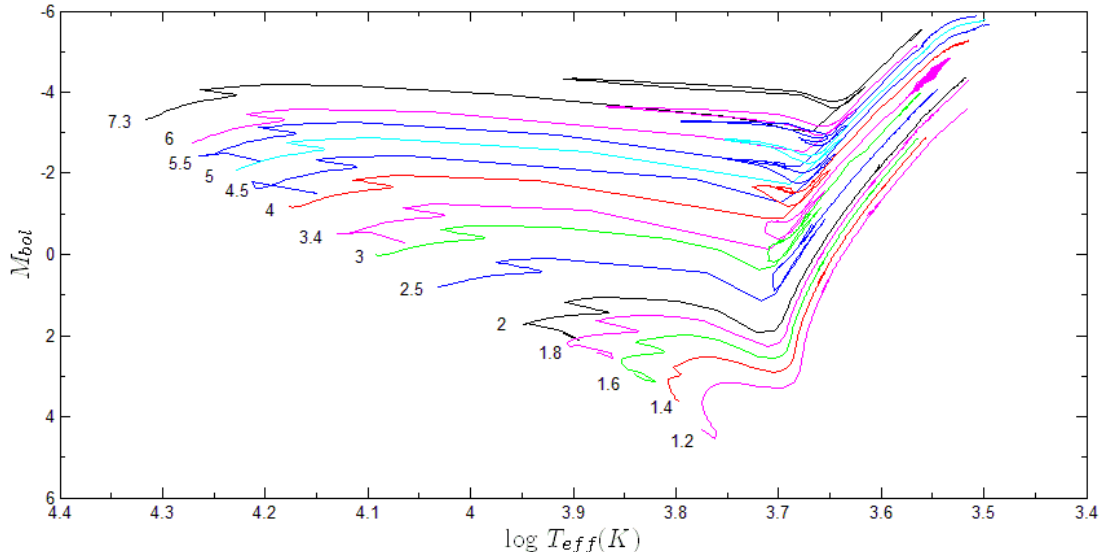


Fig. 2.— Selected evolutionary tracks of models of masses ranging between $1.2M_{\odot}$ and $7.3M_{\odot}$ (as indicated on figure), calculated from the main sequence to the AGB stage.

3.2. Helium flash

After the beginning of core He-burning, red giant stars of masses $\leq 2.2M_{\odot}$, and of solar initial composition, experience the core helium flash. This happens because the triple-alpha reaction is strongly temperature-dependent and ignites in an electron-degenerate environment (Mocák et al. 2010; Bildsten et al. 2012; Kawaler 2012). Since the pressure is not sensitive to temperature in a degenerate gas, a flash-like thermal runaway occurs. In Fig. 3 it is seen that the central density does not vary significantly during the relatively short phase of the helium flash. However, the central temperature increase is remarkable and required to lift the degeneracy so that the He-burning can then proceed under hydrostatic conditions.

The evolution depicted in Fig. 3 illustrates our computational simulation which is consistent with the analytical consideration (Kippenhahn & Weigert 1990; Kippenhahn, Weigert & Weiss 2012). In particular, we find that for stars of mass $< 2M_{\odot}$, the helium flash starts off-center owing to the neutrino cooling via the plasma and photo neutrinos when the central density increases beyond the region characterized by the degeneracy parameter $\eta = 5$ (see Fig. 3). For stars in the mass range $2 < M/M_{\odot} \leq 2.2$ the helium flash starts at the center since they evolve at relatively lower central densities.

Fig. 4 shows the variation of the luminosity of a $2M_{\odot}$ star through the core He-flash as a function of time. It is seen that the luminosity due to He-burning increases flash-like to about $10^8 L_{\odot}$. Most of this power is used to expand the outer layers of the star. At this stage, the

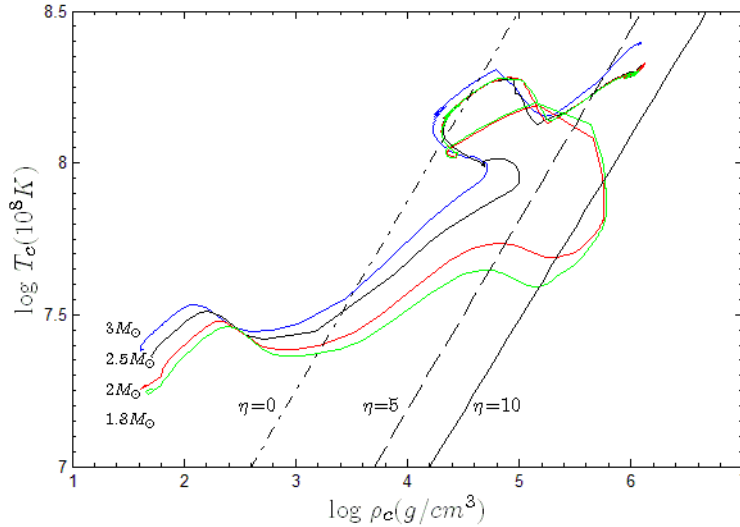


Fig. 3.— Evolutionary sequences in the $T_c - \rho_c$ plane for selected stellar masses as indicated. The lines marked by the degeneracy parameter η indicate the regions of increasing degeneracy.

temperature is $\approx 2 \times 10^8$ K, core degeneracy is almost lifted as it expands and cools. The helium flash is followed by subsequent mini-flashes until degeneracy is completely removed so that core He-burning proceeds quiescently and the star settles on the horizontal branch.

The core helium flash requires very short time steps to accommodate the rapidly changing variables. Complete calculation is performed without interpolation. In our calculation, the time step is of the order of less than a year during the core helium flash. For stars of masses in excess of $2.2M_\odot$, no significant degeneracy effects occur, so that core He-burning proceeds under hydrostatic conditions.

4. Masses of Observed Red Giants

4.1. Observational data

Extended observations have been performed by Tsuji08 for a sample of red giant stars which are given in Table 1. The effective temperatures were determined using the infrared flux method (Blackwell 1980), while the bolometric luminosities obtained by integrating the spectral energy distributions and the Hipparcos parallaxes were used to determine the absolute bolometric magnitudes. The uncertainty of the effective temperature is estimated to be 100K, and the error on the bolometric magnitude is mainly due to the errors on the parallaxes (Tsuji08). In the next section, we will use the effective temperatures and bolometric magnitudes to determine the stellar masses of

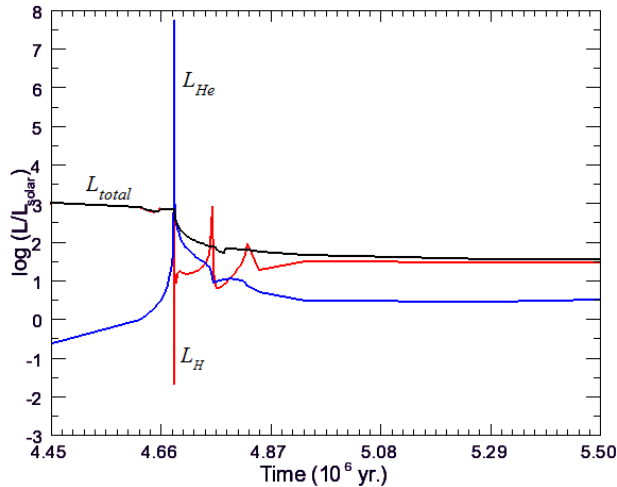


Fig. 4.— Evolution of the star’s luminosity and the luminosities due to hydrogen and helium burning during the core helium flash in a $2M_{\odot}$ model. The time starts at central He ignition.

the observed giants based on our evolutionary tracks, which cover the whole range of observations.

4.2. Mass determination

According to the work by Tsuji08, the masses of the red giant stars listed in Table 1 are derived based on the evolutionary tracks of Claret (2004). Using these tracks, extrapolations were needed at temperatures below 3200K during the RGB phase for about half of the stars in his sample. In our work, we evolved the stars until the early AGB phase without relying on extrapolation. Moreover, in the present calculation we have included mass-loss, which should improve the mass determination for the higher masses.

Adopting the values of M_{bol} and T_{eff} shown in Table 1, we use our evolutionary tracks shown in Fig. 5 to determine the masses. It is important to note here that a direct comparison of the theoretical temperature to that inferred observationally wouldn’t have been possible if our sample stars are pulsating Mira variables, in which case a radius cannot be strictly defined and any comparison wouldn’t hold. Even the term effective temperature may become questionable for the very evolved AGB stars featuring strong pulsations and mass loss (Baschek et al. 1991; Lebzelter et al. 2010). However, in this sample, the stars are on the RGB or early AGB phase, and thus, haven’t yet experienced any thermal pulsations. This allows a reliable comparison with observationally inferred temperatures. The theoretical bolometric magnitude is obtained according to the well known relation: $M_{bol} = 4.75 - 2.5 \log(L/L_{\odot})$.

Table 1: Spectral type, effective temperatures and bolometric magnitudes from Tsuji08.

Object(BS/HD)	Spectral type	T_{eff} (K)	M_{bol} (mag)
δ Vir (4910)	M3III	3643	-2.4 ± 0.3
α Tau (1457)	K5+III	3874	-1.7 ± 0.2
RRUMi (5589)	M4.5III	3397	-3.4 ± 0.3
RZ Ari (687)	M6III	3341	-3.5 ± 0.6
δ Oph (6056)	M0.5III	3790	-2.2 ± 0.3
ν Vir (4517)	M1III	3812	-2.2 ± 0.4
τ^4 Eri (1003)	M3+IIIa	3712	-2.9 ± 0.4
10 Dra (5226)	M3.5III	3730	-2.9 ± 0.3
β Peg (8775)	M2.5II-III	3606	-3.3 ± 0.2
30g Her (6146)	M6-III	3298	-4.2 ± 0.4
σ Lib (5603)	M2.5III	3596	-3.4 ± 0.5
R Lyr (7157)	M5III	3313	-4.3 ± 0.3
μ Gem (2286)	M3III	3643	-3.3 ± 0.3
OP Her (6702)	M5II	3325	-4.4 ± 0.8
ρ Per (921)	M4II	3523	-4.1 ± 0.4
α Cet (911)	M1.5IIIa	3909	-3.2 ± 0.3
λ Aqr (8698)	M2.5III	3852	-3.4 ± 0.7
XY Lyr (7009)	M5II	3300	-5.1 ± 1.1
δ^2 Lyr (7139)	M4II	3420	-5.5 ± 0.8
α Her (6406)	M5Ib-II	3293	-5.8 ± 1.6
BS6861(6861)	M4	3600	-5.2 ± 2.0

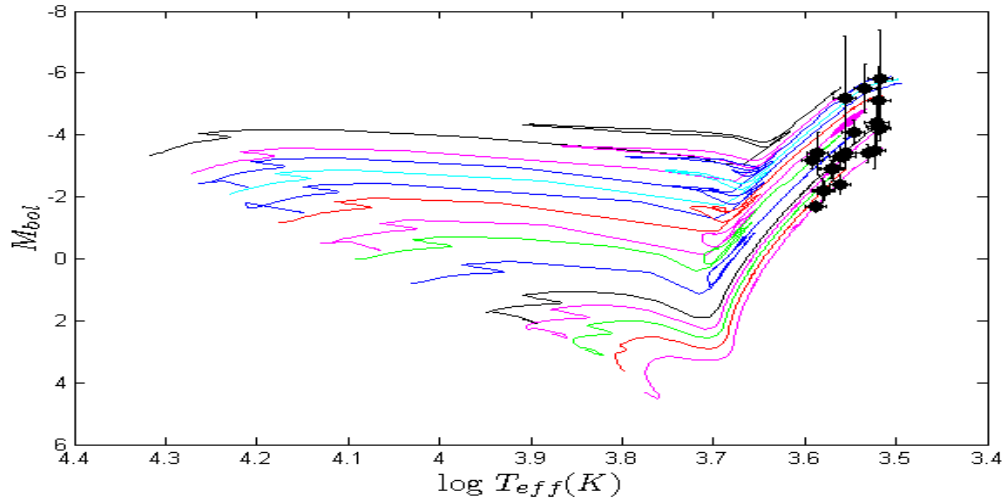


Fig. 5.— Present evolutionary tracks of stars of masses $(1.2-7)M_{\odot}$ (see text). Also shown are the observed sample listed in Table 1.

It is seen in Fig. 6 that our evolutionary tracks describe well the advanced evolutionary stage of these stars. Having obtained the mass of every star using our evolutionary tracks, we are able to identify its evolutionary stage and we can compare its CNO surface abundances with the observed ones as a consistency check. This will be described in the Sect. 5.

Our mass derivation is shown in Table 2, and in Fig 7. For completeness, we include mass determinations from other works for some stars (Maillard 1974; Smith & Lambert 1985; Harris et al. 1988; Decin et al. 1997). The error on the mass is determined from the error bars on M_{bol} and T_{eff} as obtained from Tsuji08. The inspection of this figure shows that our values are systematically lower than those obtained by Tsuji08. We attribute this mainly to two reasons:

(a) We have evolved the stars to the stage where they are observed, that is, we do not use any extrapolated tracks as done in Tsuji08 which introduces errors for $M \leq 2M_{\odot}$ in particular.

(b) We have taken into consideration mass-loss effects, which become significant for the more massive stars, as can be seen in Fig 7.

Moreover, it is clear from Table 2 that our errors on the masses are generally lower than those by Tsuji08. Calculating the tracks up to advanced stages helps to get better estimation of the masses of red giants.

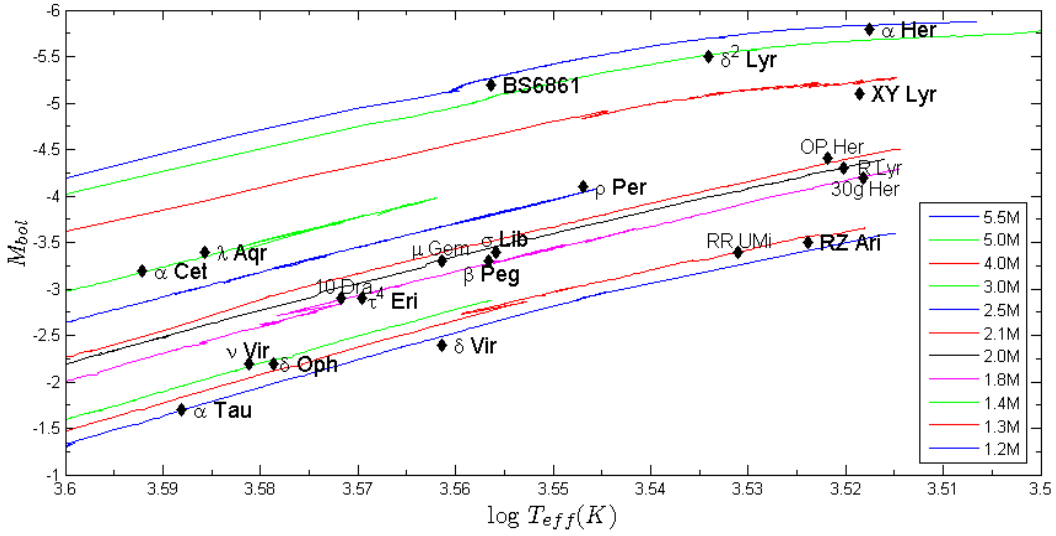


Fig. 6.— Bolometric magnitude (M_{bol}) versus effective temperature (T_{eff}) showing the present advanced evolutionary tracks together with the observed red giants listed in Table 1, see text. Note that the observed data points have errors as indicated in Table 1.

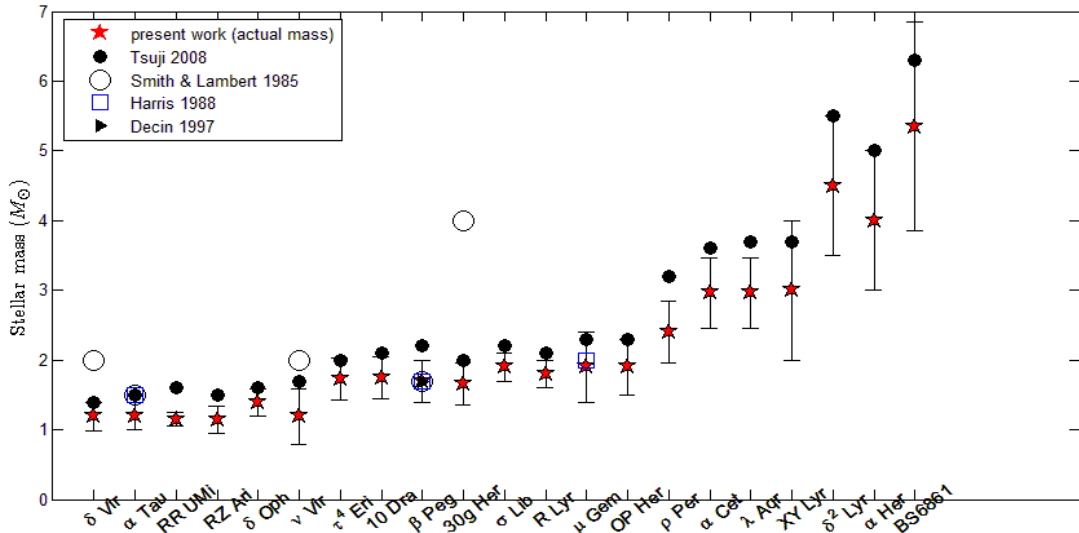


Fig. 7.— Comparison of the masses of the observed sample listed in Table 2, with other works as indicated.

Table 2: *a*: present work (M_{RGB} is the mass on the RGB, including mass-loss), *b*: Tsuji08, *c*: Smith and Lambert (1985), *d*: Harris (1988), *e*: Decin (1997), *f*: El Eid (1994). The masses are given in solar units. Note that the error on the mass by Tsuji08 increases for more massive stars, which seems to be related to the inaccuracy in the parallax measurements.

Object(BS/HD)	$M_{initial}^a$	M_{RGB}^a	M^b	M(others)
δ Vir (4910)	1.2 ± 0.2	1.19 ± 0.2	1.4 ± 0.3	2.0^c
α Tau (1457)	1.2 ± 0.2	1.20 ± 0.2	1.5 ± 0.3	$1.5^{c,d}$
RRUMi (5589)	1.3 ± 0.1	1.15 ± 0.1	1.6 ± 0.3	
RZ Ari (687)	1.3 ± 0.2	1.14 ± 0.2	1.5 ± 0.4	
δ Oph (6056)	1.4 ± 0.2	1.39 ± 0.2	1.6 ± 0.3	
ν Vir (4517)	1.4 ± 0.4	1.39 ± 0.4	1.7 ± 0.4	2.0^c
τ^4 Eri (1003)	1.8 ± 0.3	1.73 ± 0.3	2.0 ± 0.4	
10 Dra (5226)	1.8 ± 0.3	1.74 ± 0.3	2.1 ± 1.8	
β Peg (8775)	1.8 ± 0.3	1.70 ± 0.3	2.2 ± 0.3	$1.7^{c,d,e,f}$
30g Her (6146)	1.8 ± 0.3	1.65 ± 0.3	2.0 ± 0.6	4.0^c
σ Lib (5603)	2.0 ± 0.2	1.90 ± 0.2	2.2 ± 0.5	
R Lyr (7157)	2.0 ± 0.2	1.80 ± 0.2	2.1 ± 0.5	
μ Gem (2286)	2.0 ± 0.5	1.90 ± 0.5	2.3 ± 0.5	$2.0^{d,f}$
OP Her (6702)	2.1 ± 0.4	1.90 ± 0.4	2.3 ± 1.0	
ρ Per (921)	2.5 ± 0.4	2.40 ± 0.5	3.2 ± 0.5	
α Cet (911)	3.0 ± 0.5	2.96 ± 0.5	3.6 ± 0.4	
λ Aqr (8698)	3.0 ± 0.5	2.96 ± 0.5	3.7 ± 1.2	
XY Lyr (7009)	4.0 ± 1.0	3.0 ± 1.0	3.7 ± 1.5	
δ^2 Lyr (7139)	5.0 ± 1.0	4.5 ± 1.0	5.5 ± 2.0	
α Her (6406)	5.5 ± 1.5	4.0 ± 1.0	5.0 ± 2.0	7.0^f
BS 6861(6861)	5.5 ± 1.5	5.35 ± 1.5	6.3 ± 4.0	

5. CNO Surface Abundances in Red Giants

5.1. Overview of observations

A large body of observational data is available for CNO elements in evolved stars. To compare our theoretical predictions of these elements and their ratios with observations, we focus on a homogenous sample of red giants analyzed by Tsuji08. We have estimated the masses of the giants in this sample in the previous section, and we analyze the CNO abundances in the following sections.

It is not an easy task to compare the surface abundances directly with observations, because this comparison is model-dependent on both theoretical and observational grounds. On one hand, deriving the C and O ratios observationally involves several sources of uncertainty like the dispersion in the ratios obtained from different lines, and inaccuracy in the atmospheric model parameters. Systematic errors may also be present, such as the uncertainty in the continuum position and departures from local thermodynamic equilibrium (LTE) (Abia et al. 2012), in addition to the difficulties that are inherent in the spectral analysis of very cool stars. The fact that atmospheric values are model-dependent causes discrepancies between observational results among different groups, and consequently, affect the subsequent discussion (Ramstedt & Olofsson 2014). On the other hand, theoretical models are also challenged by uncertainties on convective mixing, mass loss and nuclear reaction rates, where standard FDUP models often face difficulties in explaining C and O surface abundances, particularly in LMS. It is nonetheless worth trying this comparison for the sake of a better understanding.

The $^{16}\text{O}/^{17}\text{O}$ ratios are based on a line-by-line analysis of the isolated lines of $^{12}\text{C}^{16}\text{O}$, $^{13}\text{C}^{16}\text{O}$, and $^{12}\text{C}^{17}\text{O}$ abundances. The $^{16}\text{O}/^{17}\text{O}$ ratio of the same object differs considerably among different observations. This is a general feature of observationally atmospheric values due to the aforementioned uncertainties in describing the properties of the relatively cool atmospheres of red giants, where at such low temperatures the absorption lines are strong causing severe blending by several weak lines and introducing uncertainties especially when measuring faint lines like $^{12}\text{C}^{17}\text{O}$ in such cool stars (Tsuji08). These uncertainties are introduced as error bars in Table 3. Due to such complications, in stars like α Tau, ν Vir, σ Lib, β Peg, λ Aqr, δ Vir, ρ Per, BS6861 and RR UMi, weak lines couldn't be measured at all for $^{12}\text{C}^{17}\text{O}$, in which cases the $^{16}\text{O}/^{17}\text{O}$ is not well determined, but rather, only a lower limit estimate is provided. We also include the $^{16}\text{O}/^{17}\text{O}$ ratios from field star observations of Harris & Lambert (1984b) and Maillard (1974).

5.2. Predictions of surface abundances with standard mixing

By standard mixing we mean determining the convective boundary on the basis of the Schwarzschild criterion for convective instability. In this section, we present our results for the surface CNO abundances of the sample of stars evolved to the early AGB phase. We will then compare these results with the CNO isotopic ratios inferred from observations. First, we present the abundance profiles

of the CNO isotopes and those of H and He prior to the FDUP as shown in Fig. 8. In order to study the variation of these abundance profiles as a function of the initial stellar mass, we selected the masses 1.4, 2, 3 and $5M_{\odot}$. Several features can be identified in these figures:

(a) The isotope ^{13}C is produced near the middle of the star by the CN cycle in all cases. This reflects the relatively low temperatures required for the production of this isotope in stars by the CN-cycle.

(b) A profile of ^{17}O is remarkable, showing a steep gradient in the central region of the star. This is because ^{17}O is produced by the ON cycle which requires higher temperatures to become effective.

(c) The isotope ^{18}O is effectively destroyed due to the reaction $^{18}\text{O}(p, \alpha)^{15}\text{N}$.

(d) The elements ^4He and ^{14}N are produced, being the typical products of the CNO cycle.

These results are well known in the literature, but it is important to better understand the surface abundances resulting after FDUP and SDUP for different stellar masses. The efficiency of FDUP in changing the surface abundances is related to the maximum penetration of the convective envelope on the red giant branch. In Fig 8, the maximum penetration indicated by a solid vertical line marks the range of convective mixing that results when applying the Schwarzschild criterion of convection. The dashed vertical line is that resulting when extra mixing is considered (see Section 5.3 for details).

After FDUP, the change of the surface composition depends on the profile of the isotope formed in the star. In the case of ^{13}C , the peak of its profile is located in the middle part of the star, so that envelope convection is able to smear out the profile which causes an increase of the ^{13}C surface abundance, or a decrease in the $^{12}\text{C}/^{13}\text{C}$ ratio. In the case of ^{17}O , the situation is highly dependent on the stellar mass because the main production of ^{17}O is concentrated in the inner part. Fig. 8 (upper panel) shows that in stars of $M \leq 2M_{\odot}$ envelope convection does not completely smear out the ^{17}O peak as in those of $M \geq 3M_{\odot}$. This makes the ^{17}O profile sensitive to mixing in stars of $M \leq 2M_{\odot}$, so that any additional mixing below the envelope will increase the surface abundance of ^{17}O . This effect is less pronounced for those with $M \geq 3M_{\odot}$ (Fig. 8 (lower panel)), where the ^{17}O bump is fully engulfed by the formal convective envelope, so extra mixing will not significantly alter its surface abundance in these stars.

Table 3 summarizes the values of $^{16}\text{O}/^{17}\text{O}$, $^{12}\text{C}/^{13}\text{C}$ and $^{14}\text{N}/^{15}\text{N}$ after the first and second dredge up (if any) in the case of standard convective mixing, together with those inferred from observations by Tsuji08 and others. It is important to note that the stars of the sample analyzed by Tsuji08 are advanced in evolution, but did not experience the third dredge up during the AGB phase. This is evident from the surface carbon abundances (Tsuji 2014, private communication). Thus, the comparison can be restricted to the effects of FDUP and SDUP only.

Fig. 9 shows the $^{16}\text{O}/^{17}\text{O}$ ratios as a function of stellar mass, along with the theoretical predictions by Boothroyd & Sackmann (1999), Abia et al. (2012) and Karakas & Lattanzio (2014)

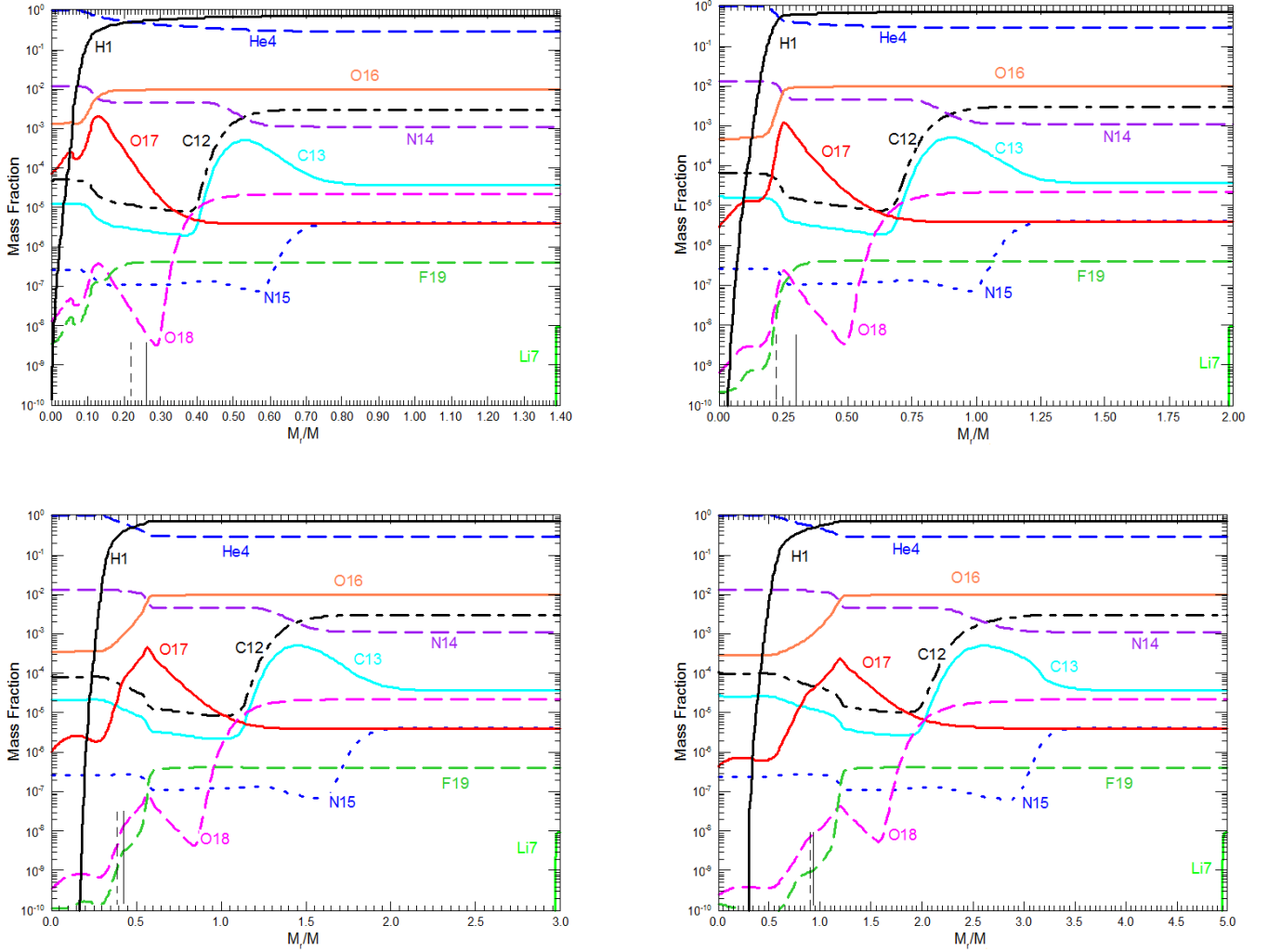


Fig. 8.— Abundance profiles after core H-burning for several products of the CNO cycle for the stellar masses $1.4M_{\odot}$ (upper left), $2M_{\odot}$ (upper right), $3M_{\odot}$ (lower left) and $5M_{\odot}$ (lower right). The solid lines mark the deepest penetration in mass of the convective envelope, while the dashed lines mark the deepest penetration with extra mixing (envelope overshooting). See text for details.

Table 3: M_{RGB} (in solar units) and the surface number abundances after FDUP and SDUP (if any, listed in parenthesis): a : surface abundances with standard mixing (present work), b : Tsuji08, g : Harris and Lambert (1984b), h : H85: Harris et al. (1985), i : Smith and Lambert (1990), j : Decin et al. (2003), k : Maillard (1974), l : Hinkle et al. (1976).

Object	M_{RGB}	$^{16}\text{O}/^{17}\text{O}^a$	$^{16}\text{O}/^{17}\text{O}^b$	$^{16}\text{O}/^{17}\text{O}$	$^{12}\text{C}/^{13}\text{C}^a$	$^{12}\text{C}/^{13}\text{C}^b$	$^{12}\text{C}/^{13}\text{C}$	$^{14}\text{N}/^{15}\text{N}^a$
δ Vir	1.19	2370	> 2500		32	12.3 ± 1.2	16 ± 4^i	551
α Tau	1.2	2370	> 1000	600_{+130}^{-150g}	30	10.6 ± 1.0	$10 \pm 2^{i,j}$	551
				525_{+250}^{-125g}			9 ± 1^g	
RRUMi	1.15	2006	> 2000		30	10.0 ± 0.8		598
RZ Ari	1.14	2006	607 ± 48		30	7.9 ± 0.8		598
δ Oph	1.39	1500	387 ± 68		29	11.1 ± 0.9		690
ν Vir	1.39	1500	> 2000		29	8.7 ± 1.3	12 ± 2^i	690
τ^4 Eri	1.73	461	687 ± 14		24	12.4 ± 0.3		963
10 Dra	1.74	461	151 ± 11		24	14.8 ± 1.6	12 ± 3^i	963
β Peg	1.7	462	> 2500	1050_{+500}^{-250g}	24	7.7 ± 0.5	8 ± 2^i	963
				$\geq 100^g$			5 ± 3^j	
30g Her	1.65	462	211 ± 42	$675_{-175}^{+175} h$	24	12.5 ± 1.1	10 ± 2^i	963
σ Lib	1.9	301	> 1500		22	7.5 ± 0.3		1126
R Lyr	1.8	301	368 ± 44		22	6.4 ± 0.3		1126
μ Gem	1.9	301	798 ± 73	$325_{+150}^{-75} g$	22	10.5 ± 1.2	13 ± 2^i	1126
				$\geq 100^g$				
OP Her	1.9	246	329 ± 31		22	11.3 ± 1.2		1103
ρ Per	2.4	234	> 1000		22	9.7 ± 1.0	15 ± 2^i	1307
α Cet	2.96	318(317)	586 ± 47		21(21)	11.1 ± 0.8	10 ± 2^j	1460(1501)
λ Aqr	2.96	318(317)	> 1000		21(21)	7.9 ± 1.4		1460(1501)
XY Lyr	3.0	424(395)	223 ± 16		21(20)	15 ± 0.4		1528(1610)
δ^2 Lyr	4.5	400(378)	465 ± 41		21(20)	16.2 ± 1.5		1503(1629)
α Her	4.0	424(402)	102 ± 8	180_{+70}^{-50g}	21(20)	11.1 ± 0.7	$17 \pm 4^{g,l}$	1538/1642
				200_{+25}^{-25g}				
				$\approx 450^g$				
				450_{+50}^{-50k}				
BS 6861	5.35	424(402)	> 1000		21(20)	48.5 ± 2.9		1538(1642)
Initial		2620			90			270

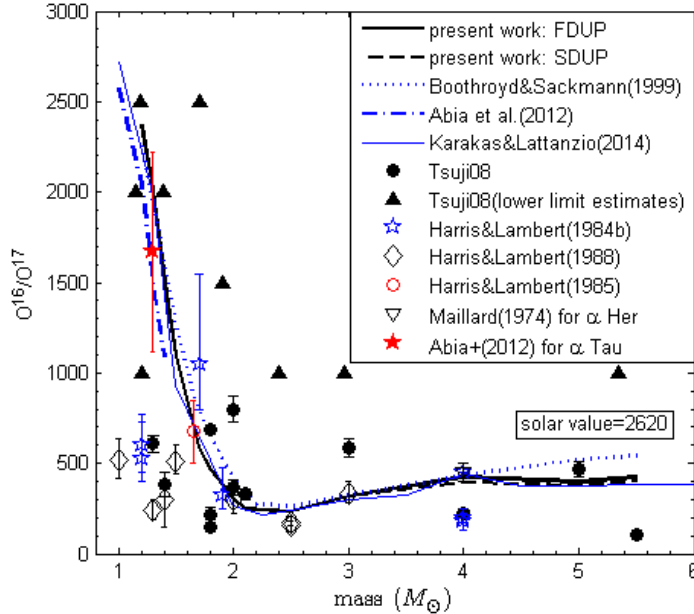


Fig. 9.— Calculated $^{16}\text{O}/^{17}\text{O}$ ratios for the 21 giants after FDUP (solid line) and SDUP (dashed line) versus stellar mass. Calculation by Boothroyd & Sackmann (1999), Abia et al. (2012) and Karakas & Lattanzio (2014) are also shown. Observations are indicated as data points. Note that our mass determinations have errors on them, as indicated in Table 2.

as well as available observations for comparison. It can be noticed that for masses below $2M_{\odot}$, the predicted $^{16}\text{O}/^{17}\text{O}$ ratios are higher than most of the data points obtained from observations. This discrepancy shows that more ^{17}O needs to be mixed to the surface in order to lower the $^{16}\text{O}/^{17}\text{O}$ ratio in the models. This may be achieved by extra mixing (or overshooting) at the bottom of the convective envelope. In order to constrain this extra mixing, a better understanding is required for the role of first and second dredge up for the whole range of masses under consideration.

It is known that after the star leaves the main sequence, FDUP alters significantly the surface abundances as it enriches the envelope with ^4He , ^{13}C , ^{17}O and ^{14}N and reduces its abundance of ^{12}C , ^{15}N and ^{18}O . All solar metallicity stars evolved to the AGB phase have experienced the FDUP episode (Straniero et al. 2006), and start their early AGB phase with a sharp composition discontinuity at the point of maximum penetration of the FDUP. The H-burning shell in low-mass stars erases this composition discontinuity, but it represents an entropy barrier that prevents any deeper penetration of the convective envelope, and thus no further change in the surface abundances of these stars takes place. However, for solar metallicity stars with masses above $3 - 4M_{\odot}$, the gravitational energy release due to the contracting core and the increased energy flux from the burning He-shell drive the H-shell to low temperatures that cause a temporary shut-down in the

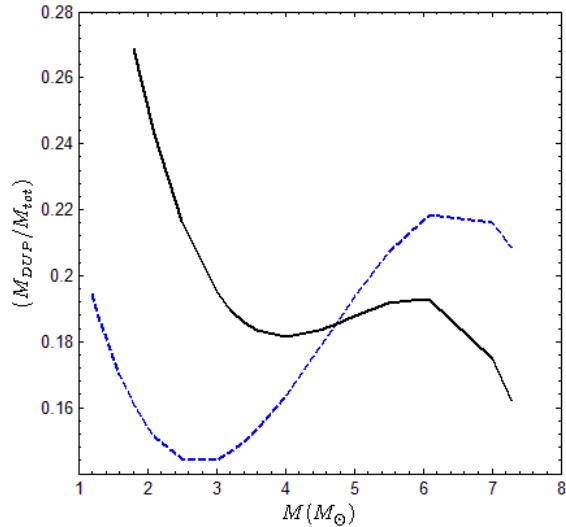


Fig. 10.— Fractional mass reached by the convective envelope at FDUP (dashed line) and SDUP (solid line). SDUP is deeper than FDUP only in models of stellar masses $\geq 5M_{\odot}$. The mass on the y-axis is given as the mass reached by the DUP over the total initial stellar mass, in solar units.

H-burning. This situation, coupled to the drop in the temperature of the expanding layers and the increase in their opacity (Iben & Renzini 1983) cause convection to deepen in a second dredge up (SDUP) event, smear out the composition discontinuity left over by the FDUP and therefore, this SDUP introduces further changes in the surface abundances of stars of masses $\gtrsim 4M_{\odot}$.

Fig. 10 shows the maximum penetration of the convective envelope at first and second dredge up as a function of the initial stellar mass. It is clear from the figure that for masses less than 4 to $5M_{\odot}$, the SDUP doesn't penetrate deeper than the FDUP, and thus, it does not introduce significant change to the surface composition. This is in agreement with Karakas & Lattanzio (2014), for example, for their solar metallicity case. Their Fig. 7 exhibits similar general features and also indicates a deepest penetration of FDUP in $\approx 2.5M_{\odot}$ stars. Therefore, since the low mass stars do not experience SDUP, this implies that their observed surface abundances on the AGB phase are actually "inherited" from the RGB phase. Therefore, one way to account for the discrepancy between calculated and observed values of $^{16}\text{O}/^{17}\text{O}$ in these stars is to invoke extra mixing below the convective envelope on the RGB phase.

5.3. Predictions of surface abundances with extra mixing

We apply overshooting as outlined in Sect. 2.2 over a depth of $0.7H_p$, $1H_p$ and $1.3H_p$, which we label as cases A, B and C, respectively. Fig. 11 shows the $^{16}\text{O}/^{17}\text{O}$ ratios for our star sample

with the three cases. We find that case C provides the best estimation for the overshooting distance for low mass stars. It is noted that overshooting has only a minor effect for stars $\geq 3M_{\odot}$. This is expected and can be explained in terms of the ^{17}O abundance profile in these stars as shown in Figs. 8. The calculated and observed values for these stars are generally in a good agreement. However, a problem arises in explaining the carbon isotopic abundances in stars of $M \leq 2M_{\odot}$, where the extra mixing we used cannot explain the low $^{12}\text{C}/^{13}\text{C}$ ratios observed in these giants as shown in Fig. 12. The calculations using standard mixing by Boothroyd & Sackmann (1999) and Karakas & Lattanzio (2014) show a similar problem. $^{12}\text{C}/^{13}\text{C}$ ratios close to 10 or below cannot be obtained by our extra mixing at the base of the convective envelope with the ^{12}C profile as in Fig. 8. A non-standard mixing process seems to be required in low-mass stars ($< 2M_{\odot}$) which can reduce the abundance of ^{12}C by mixing it to the hotter regions of the H-burning shell, allowing for some nuclear processing. Such mixing process is linked to the long evolutionary time of the low-mass stars when ascending the RGB. As discussed in some details in Karakas & Lattanzio (2014), the so-called "thermohaline mixing" or "salt-finger instability" seems to be one reasonable description of this extra mixing in low-mass red giant stars. This is still an unsettled problem in stellar models.

Fig. 13 shows the nitrogen abundances after FDUP and SDUP with and without extra mixing. Given the scatter in the observed data, we find that, on average, our theoretical prediction reasonably reproduces the observationally inferred data.

6. Effect of modified nuclear reaction rates

6.1. Effect on the $^{16}\text{O}/^{17}\text{O}$ ratio

In order to investigate the effect of nuclear reaction rates on the $^{16}\text{O}/^{17}\text{O}$ ratios, we adopt three different evaluations of the proton-capture reactions $^{16}\text{O}(p, \gamma)^{17}\text{F}$, $^{17}\text{O}(p, \gamma)^{18}\text{F}$ and $^{17}\text{O}(p, \alpha)^{14}\text{N}$. In particular, we study the $^{16}\text{O}/^{17}\text{O}$ ratios of the observed sample with the four compilations of the ^{17}O production and destruction reactions as obtained by Sergi et al. (2014) (SE14), Sallaska et al. (2013) (SA13), Iliadis et al. (2010) (IL10) and Chafa et al. (2007) (CH07). The results are shown in Fig. 14 for both cases: standard mixing (left panel) and envelope overshooting (right panel). None of the four sets shows a reasonable agreement between our model predictions and observations unless overshooting is included in our models. The more recent determinations of the rate, in particular SE14, SA13 and IL10, yield slightly higher $^{16}\text{O}/^{17}\text{O}$ ratios for stars in the mass range $1.2 - 2.5M_{\odot}$ with overshooting, which emphasizes the fact that indeed deeper mixing is required to explain the $^{16}\text{O}/^{17}\text{O}$ ratios in these stars to achieve a better agreement with observations.

The effect of uncertainties in the reaction rates on $^{16}\text{O}/^{17}\text{O}$ ratios is also worth exploring. Since the SA13 compilation is based on a Monte Carlo simulation, and the rates have statistically well-defined uncertainties (Longland et al. 2010; Longland 2012; Iliadis et al. 2014), we investigate the $^{16}\text{O}/^{17}\text{O}$ ratios using the recommended, high and low rates, where the rate boundaries correspond to a 95% coverage probability.

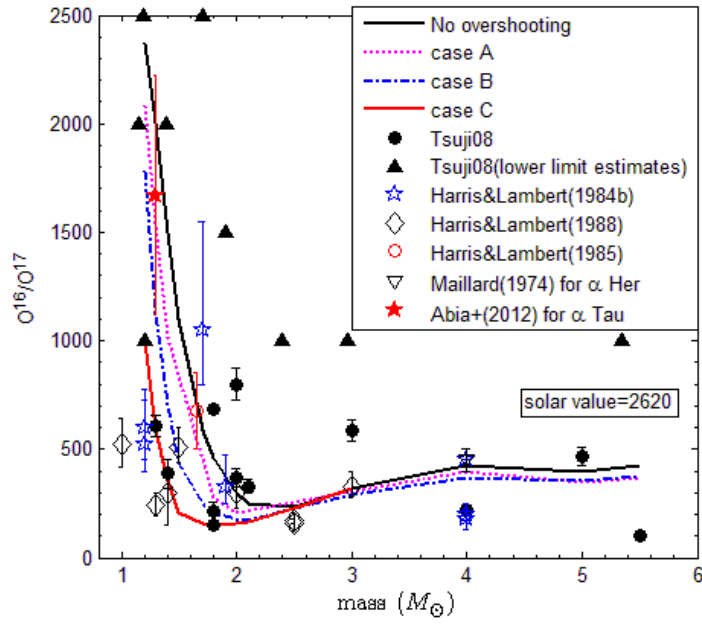


Fig. 11.— $^{16}\text{O}/^{17}\text{O}$ ratio when overshooting below the convective envelope is applied for the three cases A, B and C where each corresponds to a different efficiency of overshooting as discussed in text.

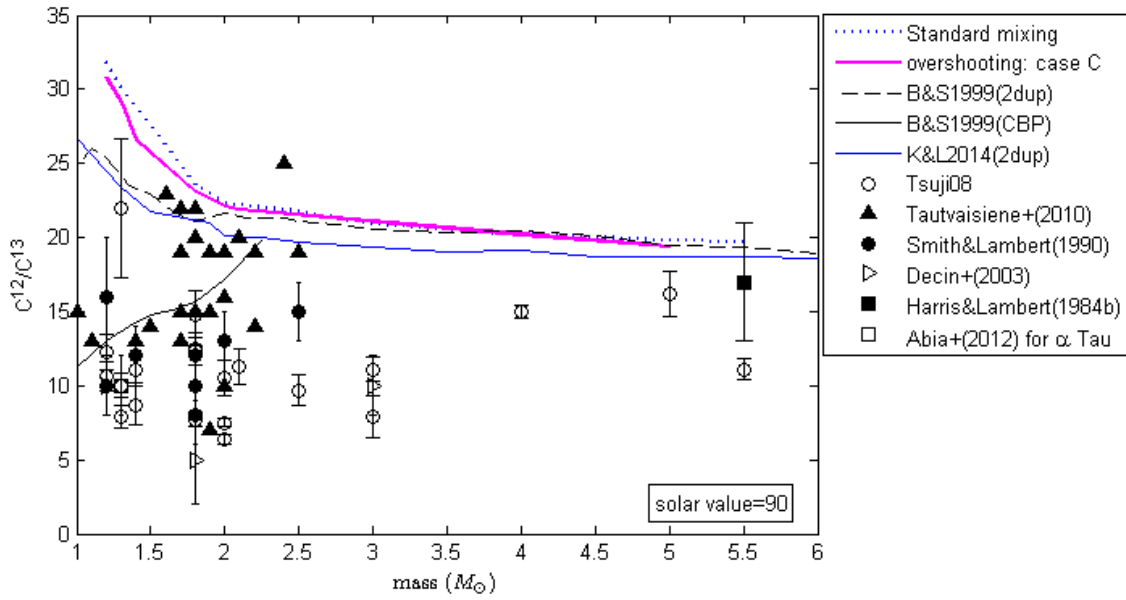


Fig. 12.— Envelope overshooting used in this study cannot explain the low observed $^{12}\text{C}/^{13}\text{C}$ ratios in low mass stars. Note that the results shown from Tautvaišienė et al. (2010) are only for stars with solar-like and near solar composition. Calculations by other groups are also shown for comparison.

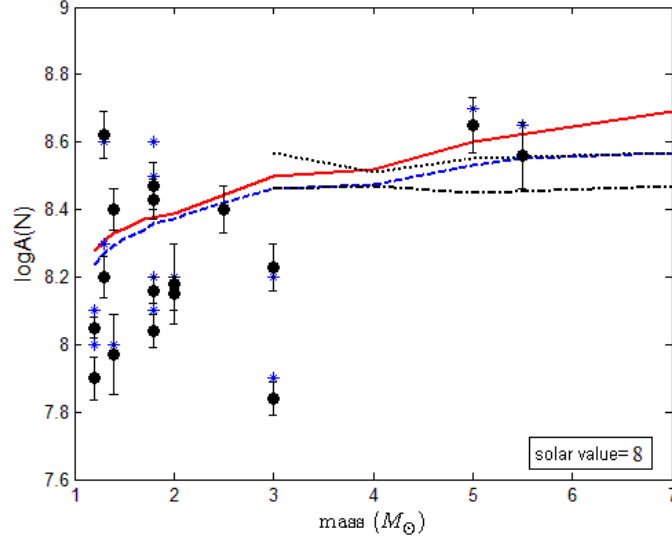


Fig. 13.— The nitrogen abundance calculated for the 21 giants. Abundances after FDUP without and with overshooting (red solid line and dashed blue line, respectively) and after SDUP without and with overshooting (black dotted and dot-dashed lines, respectively). The observational values are by Tsuji08 using two methods: standard abundance analysis (filled black circles) and the curve-of-growth (COG) method (blue astrisks) (see Tsuji08 for details).

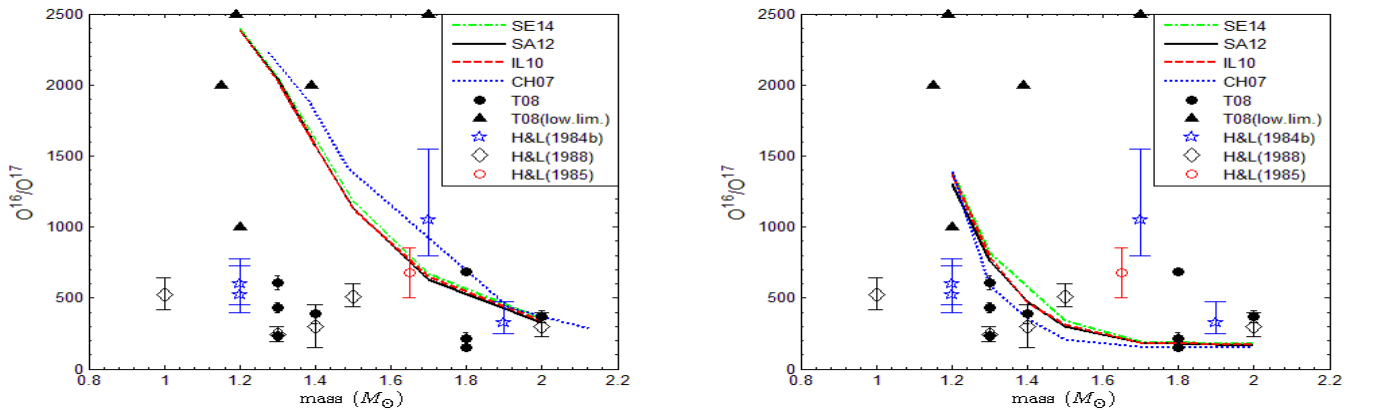


Fig. 14.— The $^{16}\text{O}/^{17}\text{O}$ ratio calculated for the 21 giants, with 4 different sets of compilations of reaction rates. Left panel shows the case with standard mixing and the right panel is that with overshooting. Several observational data are also included.

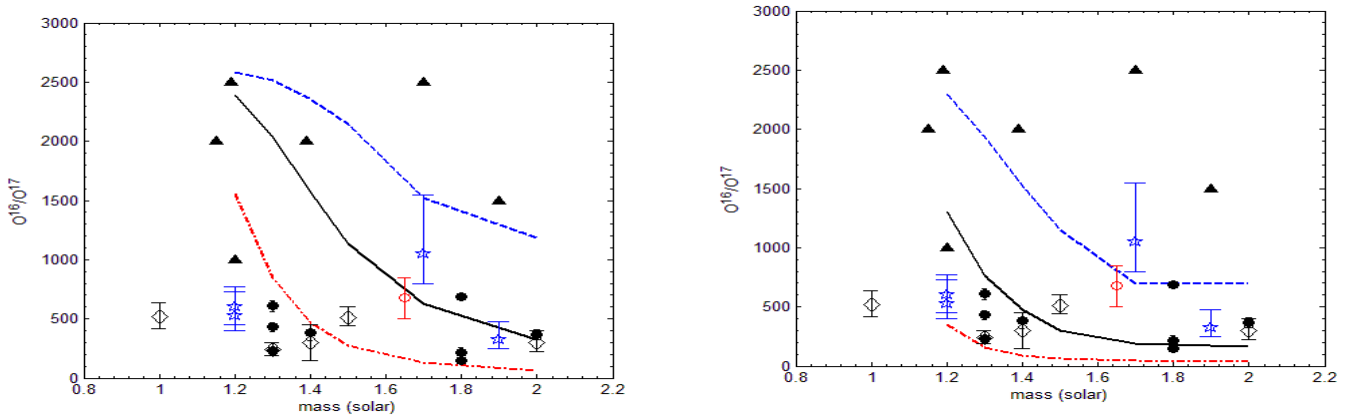


Fig. 15.— The SA13 set of rates without overshooting (left panel) and with overshooting (right panel) (see text for details). We show the median rates (solid line), their upper limits (dot-dashed) and lower limits (dashed). Observational data same as in Fig. 14 and 15.

The result depicted in Fig. 15 shows that without overshooting (left panel), the expected range provided by the uncertainty on the rates is not sufficient to explain the observational data for low masses. When overshooting is taken into account, the observations can be better explained as shown in the right panel of Fig. 15. Note that in both figures, there is a scatter in the observational data. In both cases we cannot explain the data points marked by filled triangles, which represent stars whose weak lines couldn't be measured at all for $^{12}\text{C}^{17}\text{O}$, and thus their $^{16}\text{O}/^{17}\text{O}$ ratios are not well determined, but rather, only a lower limit is provided.

We also performed a separate calculation where we tried to optimize the abundance of ^{17}O in a trial to explain the low $^{16}\text{O}/^{17}\text{O}$ observed in low-mass stars. The most suitable combination to maximize ^{17}O is to use the upper rate of the ^{17}O production reaction $^{16}\text{O}(p, \gamma)^{17}\text{F}$ and the lower rates of the ^{17}O destruction reactions $^{17}\text{O}(p, \gamma)^{18}\text{F}$ and $^{17}\text{O}(p, \alpha)^{14}\text{N}$. This combination yields $^{16}\text{O}/^{17}\text{O}$ values that are very close to those obtained with the upper rates of Fig. 15 (left panel). We conclude that even an optimal choice of reaction rates within the suggested range of uncertainty does not fully explain the $^{16}\text{O}/^{17}\text{O}$ in low mass stars without invoking envelope overshooting.

6.2. Effect on the $^{14}\text{N}/^{15}\text{N}$ ratio

The $^{14}\text{N}/^{15}\text{N}$ ratio is worth considering especially in the light of the new determination of the $^{14}\text{N}(p, \gamma)^{15}\text{O}$ rate (Adelberger et al. 2011; Halabi et al. 2012). Fig. 16 shows this ratio calculated for the whole mass range after FDUP and SDUP. It is clear that our values are higher than those by El Eid (1994) in stars of masses $\geq 3M_{\odot}$. This is due to the NACRE $^{14}\text{N}(p, \gamma)^{15}\text{O}$ rate used by El Eid (1994), which is almost a factor of 2 higher than our new rate in the relevant temperature range (see Halabi et al. (2012) for the expression of this rate and explicit discussion). This difference

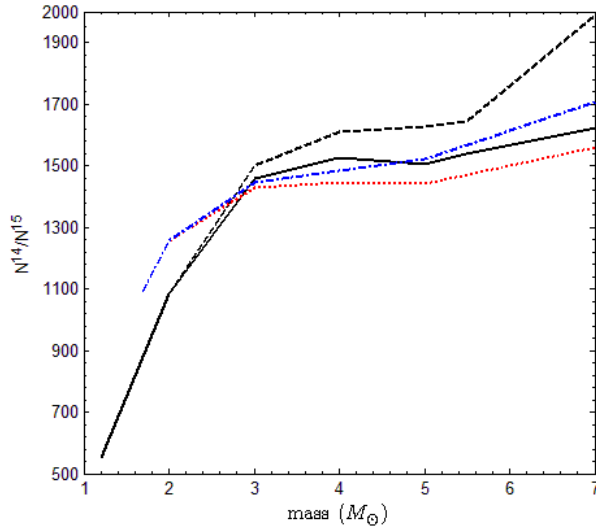


Fig. 16.— $^{14}\text{N}/^{15}\text{N}$ ratio calculated after FDUP (black solid line) and SDUP (black dashed line). The values by El Eid (1994) after FDUP (red dotted line) and SDUP (blue dot-dashed line) are included for comparison.

becomes more pronounced in higher mass stars, in the effect of SDUP, in particular. However, our calculation shows lower $^{14}\text{N}/^{15}\text{N}$ in the low-mass stars.

To explain these results, we argue that the $^{14}\text{N}(p, \gamma)^{15}\text{O}$ rate has different effect in high-mass and low-mass stars. In higher masses, the ^{14}N abundance is mainly affected by the rate efficiency and is thus higher with the lower rate. In lower masses, the lower $^{14}\text{N}(p, \gamma)^{15}\text{O}$ rate results in a less efficient H-burning shell, less expansion on the RGB, thus less deep envelope convection and consequently a less deep FDUP (Halabi et al. 2012). For a $2M_{\odot}$ star for example, the depth of FDUP is $0.2847M_{\odot}$ and $0.2899M_{\odot}$ with NACRE and new rate, respectively. This explains our lower $^{14}\text{N}/^{15}\text{N}$ ratios in the lower masses.

7. Conclusions

In this work we considered a sample of 21 observed RGB and early AGB stars and determined their masses by using extended evolutionary tracks. This was done without the need of extrapolation at lower effective temperatures as it has been done by Tsuji08. The complete evolutionary tracks include the effect of mass-loss, which becomes important during the red giant phases, especially for the higher stellar masses. The investigation also included comparing the CNO surface abundances of the red giants with the observational values. We studied the variation of the CNO isotopes due to additional mixing or overshooting at the base of the convective envelope. In ad-

dition, we considered the effect of recent determinations of the reaction rates on the production and destruction of ^{17}O . The experimentally suggested uncertainty of these rates is not sufficient to explain the $^{16}\text{O}/^{17}\text{O}$ observed in low mass stars. Additional mixing beyond the convective envelope as determined by the Schwarzschild criterion is found to be necessary to better explain the observational CNO surface abundances, especially in low mass stars. Moreover, we study the effect of $^{14}\text{N}(p, \gamma)^{15}\text{O}$ rate on the $^{14}\text{N}/^{15}\text{N}$ ratios in the whole mass range. After showing in a previous work its effect on the extension of blue loops, we find that it is also important for predicting the $^{14}\text{N}/^{15}\text{N}$ ratios, particularly in intermediate mass stars.

In the case of $^{12}\text{C}/^{13}\text{C}$ ratio, the lower values (≤ 18) observed in low-mass red giants ($M < 2M_{\odot}$) cannot be explained by overshooting. Another mechanism of mixing is to be considered during the long evolutionary time needed for the low-mass stars to ascend the red giant branch.

REFERENCES

- Abia, C., Palmerini, S., Busso, M., & Cristallo, S. 2012, *A&A*, 548, A55
- Adelberger, E. G., García, A., Robertson, R. G. H., et al. 2011, *Rev. Mod. Phys.*, 83, 195A
- Amari, S., Nittler, L. R., Zinner, E., Gallino, R., Lugaro, M., & Lewis, R. S. 2001, *ApJ*, 546, 248
- Angulo, C., Arnould, M., Rayet, M., et al. 1999, *Nucl. Phys. A*, 656, 3A
- Baschek, B., Scholz, M., & Wehrse, R. 1991, *A&A*, 246, 374
- Bildsten, L., Paxton, B., Moore, K., Macias, P. J. 2012, *ApJ*, 744L, 6B
- Blackwell, D. E., Petford, A. D., & Shallis, M. J. 1980, *A&A*, 82, 249
- Boothroyd, A. I., Sackmann, I.-J., & Wasserburg, G. J. 1995, *ApJ*, 442, L21
- Boothroyd, A. I. & Sackmann, I.-J. 1999, *ApJ*, 510, 232
- Bowen, G. H., 1988, *ASSL*, 148, 3B
- Busso, M., Trippella, O., Maiorca, E., Palmerini, S. 2014, *AIPC*, 1595, 41B
- Chafa, A. et al., 2007, *PRC* 75, 035810
- Charbonnel, C. 1994, *A&A* 282, 811
- Charbonnel, C. 1995, *ApJ*, 453, L41
- Charbonnel, C., & Do Nascimento, J. D. 1998, *A&A*, 336, 915
- Claret, A. 2004, *A&A*, 424, 919

- Connes, P. 1970, *ARA&A*, 8, 209
- Dearborn, D. S. P. 1992, *Phys. Rep.*, 210, 367
- De Beck, E., Decin, L., de Koter, A., Justtanont, K., Verhoelst, T., Kemper, F. & Menten, K. M., 2010, *A&A* 523, A18
- Decin, L., Cohen, M., Eriksson, K., Gustafsson, B., Huygen, E., Morris, P., Plez, B., Sauval, J., Vandenbussche, B., Waelkens, C. 1997, *ESASP*, 419, 185D
- Decin, L., Vandenbussche, B., Waelkens, C., et al. 2003, *A&A*, 400, 709
- Denissenkov, P. A., & Weiss, A. 1996, *A&A*, 308, 773
- Denissenkov, P., VandenBerg, D., Hartwick, D., Herwig, F., Weiss, A., Paxton, B. 2014, *arXiv1409.1193D*
- El Eid, M. F. 1994, *A&A*, 285, 915
- El Eid, M. F., The, L.-S., & Meyer, B. 2009, *Space Sci. Rev.*, 147, 1
- Freytag, R., Ludwig, H., & Steffen, M. 1996, *A&A*, 313, 497
- Gilroy, K. K. & Brown, J. A. 1991, *ApJ* 371, 578
- Gratton, R. G., Sneden, C., Carretta, E., & Bragaglia, A. 2000, *A&A*, 354, 169
- Guandalini, R., 2010, *A&A* 513, A4
- Halabi, G. M., El Eid, M., Champagne, A., 2012, *ApJ*, 761, 10
- Hall, D. N. B., Ridgway, S. T., Bell, E. A., & Yarborough, J. M. 1979, *Proc. Soc. Photo-Opt. Instrum. Eng.*, 172, 121
- Harris, M. J., Lambert, D. L. & Smith, V.V. 1988, *ApJ*, 325, 768
- Harris, M. J. & Lambert, D. L., 1984a, *Ap,J* 281, 739
- Harris, M. J. & Lambert, D. L., 1984b, *Ap,J* 285, 674
- Harris, M. J., Lambert, D. L. & Smith, V. V. 1985, *ApJ*, 299, 375
- Iben, I., Jr., Renzini, A., 1983, *Ann. rev. Astron. Astrophys.* 21, 271
- Iben, I., Jr., 1964, *ApJ*, 140, 1631I
- Iliadis, C., Longland, R., Champagne, A., Coc, A. 2010, *Nucl.Phys.* A841, 251-322
- Iliadis, C., Longland, R., Coc, A., Timmes, F., X., Champagne, A. 2014 *arXiv:1409.5541*

- Karakas, A. & Lattanzio J. 2014, arXiv:1405.0062
- Kawaler, Steven D. 2012, AAS, 22041904K
- Kippenhahn, R., & Weigert, A. 1990, *Stellar Structure and Evolution* (Berlin: Springer-Verlag)
- Kippenhahn, R., Weigert, A. & Weiss, A. 2012, *Stellar Structure and Evolution - Second Edition* (Springer-Verlag Berlin Heidelberg)
- La Cognata, M. et al. 2010, APJ, 708, 796
- Lambert, D. L., Gustafsson, B., Eriksson, K., Hinkle, K. H. 1986, ApJ Suppl. 62, 373
- Lambert, D. L. & Ries L. M. 1981, ApJ 248, 228
- Langer, N., El Eid, M. F., & Fricke, K. J. 1985, A&A, 145, 179
- Lebzelter, T., Nowotny, W., Höfner, S., Lederer, M. T., Hinkle, K. H., & Aringer, B. 2010, A&A 517, A6
- Longland, R., Iliadis, C., Champagne, A., Newton, J., Ugalde, C., Cocc, A., Fitzgerald, R. 2010, Nucl. Phys. A, 841, 1
- Logland, R. 2012, A&A, 548A, 30L
- Luck, R. E. 1994, ApJS, 91, 309
- Maillard, J. P. 1974, *Highlights Astron.*, 3, 269
- Mocák, M., Campbell, S. W., Müller, E., Kifonidis, K. 2010, A&A, 520, 114
- Mondal, S., & Chandrasekhar, T. 2005, AJ, 130, 842
- Nittler, L. R., Alexander, C. M.O'D., Gao, X., Walker, R. M., & Zinner, E. 1997, Nucl. Phys. A, 621, 113
- Palmerini, S., La Cognata, M., Cristallo, S., & Busso, M. 2011, ApJ, 729, 3
- Palmerini, S., Sergi, M. L., La Cognata, M., Lamia, L., Pizzone, R. G., Spitaleri, C. 2013, ApJ, 764, 128P
- Perrin, G., Coudé du Foresto Ridgway, S. T., et al. 1998, A&A, 331, 619
- Piau, L., Kervella, P., Dib, S. & Hauschildt P. 2011, A&A 526, A100
- Pilachowski, C., Sneden, C., Freeland, E., & Casperson, J. 2003, AJ, 125, 794
- Ramstedt, S., Schöier, F. L. & Olofsson, H., 2009, A&A 499, 515–527
- Ramstedt, S. & Olofsson, H. 2014, A&A, 566A, 145R

- Recio-Blanco, A., & de Laverny, P. 2007, *A&A*, 461, L13
- Reimers, D. 1975, *Mem. Soc. R. Sci Liege*, 8, 369
- Ridgway, S. T., & Brault, J. W. 1984, *ARA&A*, 22, 291
- Sallaska, A. L., Iliadis, C., Champagne, A. E., Goriely, S., Starrfield, S., Timmes, F. X. 2013, *ApJS* 207, 18
- Schöier, F. L. & Olofsson, H. 2001, *A&A* 368, 969
- Sergi, L. et al. 2014, *AIPC*, 1594, 201S
- Shetrone, M. D. 2003, *ApJ*, 585, L45
- Smith, V. V. & Lambert D. L., 1985, *ApJ*, 294, 326
- Straniero, O., Gallino, R., Cristallo, S. 2006, *NuPhA.*, 777, 311S
- Sweigart, A. V., & Mengel, J. G. 1979, *ApJ*, 229, 624
- Tautvaišiene, G., Edvardsson, B., Tuominen, I., & Ilyin, I. 2000, *A&A*, 360, 499
- Tautvaišiene, G., Edvardsson, B., Puzeras, E., & Ilyin, I. 2005, *A&A*, 431, 933
- Tautvaišiene, G., Edvardsson, B., Puzeras, E., Barisevičius, G. & Ilyin, I. 2010, *Mon. Not. R. Astron. Soc.* 409, 1213
- Tsuji, T. 1991, *A&A*, 245, 203
- Tsuji, T. 2008, *A&A* 489, 1271
- van Belle, G. T., Lane, B. F., Thompson, R. R., et al. 1999, *AJ*, 117, 521
- Vassiliadis, E., & Wood, P. R., 1992, *Proc. ASA*, 10, 1
- Winters, J. M., Le Bertre, T., Jeong, K. S., Nyman, L.-Å. & Epchtein, N. 2003, *A&A* 409, 715

Bibliography

- [1] Abia C., de Laverny P., Wahlin R. 2008, *A&A*, 481, 161
- [2] Abia, C., Palmerini, S., Busso, M., & Cristallo, S. 2012, *A&A*, 548, A55
- [3] Adelberger, E. G., García, A., Robertson, R. G. H., et al. 2011, *Rev. Mod. Phys.*, 83, 195A
- [4] Aerts, C., Thoul, A., Daszyńska, J., Scuffaire, R., Waelkens, C., Dupret, M. A., Niemczura, E., & Noels, A. 2003, *Science*, 300, 1926
- [5] Alexander, D. R., & Ferguson, J. W. 1994, *ApJ*, 437, 879
- [6] Alongi, M., Bertelli, G., Bressan, A., & Chiosi, C. 1991, *A&A*, 244, 95
- [7] Angulo, C., Arnould, M., Rayet, M., et al. 1999, *Nucl. Phys. A*, 656, 3A
- [8] Arnould, M., Goriely, S., and Jorissen, A. 1999, *A&A*, 347, 572
- [9] Asplund, M., Grevesse, N., Sauval, A. J., Allende Pietro, C., Kiselman, D., 2005, *A&A* 417, 751
- [10] Baschek, B., Scholz, M., & Wehrse, R. 1991, *A&A*, 246, 374
- [11] Becker, S. A., & Iben, I. J. 1979, *ApJ*, 232, 831
- [12] Becker, S. A., & Iben, I. J. 1980, *ApJ*, 237, 111
- [13] Bertelli, G., Bressan, A., & Chiosi, C. 1985, *A&A*, 13, 279

- [14] Bildsten, L., Paxton, B., Moore, K., Macias, P. J. 2012, ApJ, 744L, 6B
- [15] Blackwell, D. E., Petford, A. D., & Shallis, M. J. 1980, A&A, 82, 249
- [16] Bono, G., Caputo, F., Cassisi, S., et al. 2000, ApJ, 543, 955
- [17] Boothroyd, A. I., Sackmann, I.-J., & Wasserburg, G. J. 1995, ApJ, 442, L21
- [18] Boothroyd, A. I. & Sackmann, I.-J. 1999, ApJ, 510, 232
- [19] Bowen, G. H., 1988, ASSL, 148, 3B
- [20] Bressan, A., Fagotto, F., Bertelli, G., & Chiosi, C. 1993, A&AS, 100, 647
- [21] Briquet et al. 2012, MNRAS, 427, 483
- [22] Busso, M., Chieffi, A., Gallino, R., Limongi, M., Raiteri, C. M., Straniero, O. 1993, IAUS, 155, 361B
- [23] Busso, M., Gallino, R., Lambert, D.L., Travaglio, C., Smith, V.V. 2001, ApJ, 557, 802
- [24] Busso, M., Wasserburg, G. J., Nollett K. M., Calandra A., Can Extra Mixing in RGB and AGB Stars Be Attributed to Magnetic Mechanisms?, 2007, ApJ ,671, 802-810
- [25] Busso, M., Trippella, O., Maiorca, E., Palmerini, S. 2014, AIPC, 1595, 41B
- [26] Carson, T.R. & Stothers, R. B. 1976, ApJ, 204, 461
- [27] Cassisi, S. & Salaris, M. 2011, ApJ, 728, L43
- [28] Caughlan, G. R., & Fowler, W. A. 1988, Atomic Data Nucl. Data Tables, 40, 283
- [29] Chafa, A. et al., 2007, PRC, 75, 035810
- [30] Charbonnel, C. 1994, A&A, 282, 811

- [31] Charbonnel, C. 1995, *ApJ*, 453, L41
- [32] Charbonnel, C., & Do Nascimento, J. D. 1998, *A&A*, 336, 915
- [33] Charbonnel C. & Zahn, J. –P. 2007, *A&A*, 467, L15
- [34] Chen, M. C.; Herwig, F.; Denissenkov, P. A.; Paxton, B. 2014, *MNRAS*, 440, 1274C
- [35] Claret, A. 2004, *A&A*, 424, 919
- [36] Claret, A. 2007, *A&A*, 475, 1019
- [37] Clayton D., Fowler W., Hull T. & Zimmerman B. 1961, *Ann. Phys.*, 12, 331
- [38] Cook, C. W., Fowler, W., Lauritsen, C. C., Lauritsen, T. 1957 *Phys. Rev.*, 107, 508
- [39] Criscienzo, M. Di, Marconi, M., Musella, I., Cignoni, M. & Ripepi, V. 2012, *MNRAS*, sts023, 36
- [40] Cristallo, S., Piersanti, L., & Straniero, O. 2013, *Mem. S.A.It.*, 84, 113
- [41] De Beck, E., Decin, L., de Koter, A., Justtanont, K., Verhoelst, T., Kemper, F. & Menten, K. M., 2010, *A&A*, 523, A18
- [42] Decin, L., Vandenbussche, B., Waelkens, C., et al. 2003, *A&A*, 400, 709
- [43] Denissenkov, P. A., & Weiss, A. 1996, *A&A*, 308, 773
- [44] Denissenkov P. A., Tout C. A., 2003, *MNRAS*, 340, 722
- [45] Denissenkov, P.; Truran, J. W.; Herwig, F.; Jones, S.; Paxton, B.; Nomoto, K.; Suzuki, T.; Toki, H. 2014a, arXiv1407.0248D
- [46] Denissenkov, P. A.; Truran, J. W.; Pignatari, M.; Trappitsch, R.; Ritter, C.; Herwig, F.; Battino, U.; Setoodehnia, K.; Paxton, B 2014b, *MNRAS*, 442, 2058D

- [47] De Smedt, K.; Van Winckel, H.; Kamath, D.; Karakas, A. I.; Siess, L.; Goriely, S.; Wood, P. 2014, *A&A*, 563L, 5D
- [48] Doherty, C., Gil-Pons, P., Lau, H., Lattanzio, J., Siess, L. 2014, *MNRAS*, 437, 195D
- [49] Dominguez, I., Straniero, O., Tornambe, A., & Isern, J. 1996, *ApJ*, 472, 783
- [50] Dupret, M.-A., Thoul, A., Scuflaire, R., Daszyńska-Daszkiewicz, J., Aerts, C., Bourge, P.-O., Waelkens, C., & Noels, A. 2004, *A&A*, 415, 251
- [51] Eggenberger, P., Maeder, A., Meynet, G., Stellar evolution with rotation and magnetic fields IV. The solar rotation profile, 2005, *A&A*, 440, L9-12
- [52] El Eid, M. F. 1994, *A&A*, 285, 915
- [53] El Eid, M. F. 1995, *MNRAS*, 275, 983
- [54] El Eid, M. F., de Loore, C. 1996, *Landolt-Börnstein-Group VI Astronomy and Astrophysics*, Vol. 3, Springer-Verlag, P. 62
- [55] El Eid, M. F., 2005, *Nature*, 433, 117
- [56] El Eid, M. F., The, L.-S., & Meyer, B. 2009, *Space Sci. Rev.*, 147, 1
- [57] Evans, N. R. 1993, *AJ*, 105, 1956
- [58] Fernie, J. D., Evans, N. R., Beattie, B., & Seager, S. 1995, *IBVS*, 4148, 1F
- [59] Fowler, W. A., & Hoyle, F. 1964, *ApJS*, 9, 201
- [60] Freytag, R., Ludwig, H., & Steffen, M. 1996, *A&A*, 313, 497
- [61] Gallino, R., Busso, M., Picchio, G., Raiteri, C. M., Renzini, A. 1988, *ApJ*, 334, 45
- [62] Garcia-Berro, E., Ritossa, C. & Iben, I., J. 1997, *ApJ*, 485, 765

- [63] Gasques, L. R., Afanasjev, A. V., Aguilera, E. F., et al. 2005, *PhRvC*, 72, 025806
- [64] Gasques, L. R., Brown, E. F., Chieffi, A., et al. 2007, *PhRvC*, 76, 035802
- [65] Gilroy, K. K. & Brown, J. A. 1991, *ApJ*, 371, 578
- [66] Gratton, R. G., Sneden, C., Carretta, E., & Bragaglia, A. 2000, *A&A*, 354, 169
- [67] Guandalini, R., 2010, *A&A*, 513, A4
- [68] Guandalini R., Ciprini S., Busso M. Silvestro J., Persi P. 2004, *Mem, S. A.It* , 75, 617
- [69] Guenther, D. B. & Demarque, P. 1997, *ApJ*, 484, 937
- [70] Gutiérrez, J., Canal, R. & Garcia-Berro, E. 2005, *A&A*, 435, 231
- [71] Halabi, G. M., 2012, *PoS (ENAS 6)* 052
- [72] Halabi, G. M., El Eid, M., Champagne, A., 2012, *ApJ*, 761, 10
- [73] Halabi G. M., 2014, *AIP Conf.Proc*, 1595, 264
- [74] Harris, M. J. & Lambert, D. L., 1984, *ApJ*, 281, 739
- [75] Harris, M. J. & Lambert, D. L., 1984, *ApJ*, 285, 674
- [76] Harris, M. J., Lambert, D. L. & Smith, V. V. 1985, *ApJ*, 299, 375
- [77] Harris, M. J., Lambert, D. L. & Smith, V.V. 1988, *ApJ*, 325, 768
- [78] Herwig F., Blocker T., Schonberner D., El Eid M. 1997, *A&A*, 324, L81
- [79] Herwig, F., Langer, N., & Lugaro, M. 2003, *ApJ*, 593, 1056
- [80] Herwig F. 2005, *ARA&A*, 43, 435H
- [81] Hinkle, K. H., Lambert, D. L., & Snell, R. L. 1976, *ApJ*, 210, 684

- [82] Hoyle, F., Danbar, P. N. F., Wenzel, W., Whiling, W. 1953 Phys. Rev., 92, 1095
- [83] Iben, I., Renzini, A., 1984, Physics Letters, 105, 6, 329
- [84] Iglesias, C. A. & Rogers, F. J. 1996, ApJ, 464, 943
- [85] Iliadis, C. 2007, Nuclear Physics of Stars (WILEY-VCH Verlag), p. 385
- [86] Iliadis, C., Longland, R., Champagne, A., Coc, A. 2010, Nucl.Phys., A841, 251-322
- [87] Iliadis, C., Longland, R., Coc, A., Timmes, F., X., Champagne, A. 2014 arXiv:1409.5541
- [88] Imbriani, G., Costantini, H., Formicola, A., et al. 2005, Eur. Phy. J. A, 25, 455
- [89] Jones, S. et al, 2013, ApJ, 772, 150
- [90] Käppeler, F., Beer, H., Wisshak, K., Clayton, D. D., Macklin, R. L., Ward, R. A. 1982, ApJ, 257, 821K
- [91] Karakas, A. & Lattanzio J. 2014, arXiv:1405.0062
- [92] Karttunen, H. 2003, Fundamental Astronomy (Springer Science & Business Media)
- [93] Kawaler, Steven D. 2012, AAS, 22041904K
- [94] Kippenhahn, R., & Weigert, A. 1990, Stellar Structure and Evolution (Berlin: Springer-Verlag)
- [95] Kippenhahn, R., Weigert, A. & Weiss, A. 2012, Stellar Structure and Evolution - Second Edition (Springer-Verlag Berlin Heidelberg)
- [96] La Cognata, M. et al. 2010, APJ, 708, 796
- [97] Lai, X. J., & Li, Y. 2011, RAA, 11, 1351
- [98] Lambert, D. L. & Ries L. M. 1981, ApJ, 248, 228

- [99] Lambert, D. L., Gustafsson, B., Eriksson, K., Hinkle, K. H. 1986, ApJ Suppl. 62, 373
- [100] Lambert, D. L. 1989, in IAU Colloq. 106: Evolution of Peculiar Red Giant Stars, ed. H. R. Johnson & B. Zuckerman, 101-130
- [101] Langer, N., El Eid, M. F., & Fricke, K. J. 1985, A&A, 145, 179
- [102] Langer, N., Heger, A., Wellstein, S., & Herwig, F. 1999, A&A, 346, L37
- [103] Lattanzio, J. & Wood, P. 2003, 'Evolution, Nucleosynthesis, and Pulsation of AGB Stars', in Harm J. Harbing, Hans Olofsson (ed.), Asymptotic Giant Branch Stars, Springer, New York, USA, pp. 23-104
- [104] Lebzelter, T., Nowotny, W., Höfner, S., Lederer, M. T., Hinkle, K. H., & Aringer, B. 2010, A&A, 517, A6
- [105] Longland, R., Iliadis, C., Champagne, A., Newton, J., Ugalde, C., Cocc, A., Fitzgerald, R. 2010, Nucl. Phys. A, 841, 1
- [106] Longland, R. & Iliadis, C. 2012, JPhCS, 337a, 2047L
- [107] Luck, R. E. 1994, ApJS, 91, 309
- [108] Lugaro, M., Herwig, F., Lattanzio, J., Gallino, R., & Straniero, O. 2003, ApJ, 586, 1305
- [109] Lugaro, M., Tagliente, G., Karakas, A., Milazzo, P. M., Kappeler, F., Davis, A. M. & Savina, M. R. 2014, ApJ, 780, 95L
- [110] Maeder, A., & Meynet, G. 1989, A&A, 210, 155
- [111] Magic, Z., Collet, R., Asplund, M., et al. 2013, A&A, 557, A26
- [112] Magic, Z., Weiss, A., Asplund, M., 2014, arxiv: 1403.1062v2

- [113] Mahmoud (Halabi), G., 2006, MS Thesis, American University of Beirut
- [114] Maillard, J. P. 1974, *Highlights Astron.*, 3, 269
- [115] Matraka, B., Wassermann, C., & Weigert, A. 1982, *A&A*, 107, 283
- [116] Merrill, P. W. 1952a, *ApJ*, 116, 21
- [117] Merrill, P. W. 1952b, *Science*, 115, 484
- [118] Mermilliod, J. C. 1981, *A&AS*, 44, 467
- [119] Meyer, B 2012, *PoS (NICXII)* 096
- [120] Mocák, M., Campbell, S. W., Müller, E., Kifonidis, K. 2010, *A&A*, 520, 114
- [121] Neilson, H. R., Cantiello, M. & Langer, N. 2011, *ASP Conf. Ser.*, 448, 155
- [122] Neilson, H. R., & Langer, N. 2012, *A&A*, 537, A26
- [123] Neilson, H. R., Langer, N., Engle, S. G., Guinan, E. & Izzard, R. 2012, *ApJ*, 760, L18
- [124] Nicolussi G. K., Pellin, M. J., Lewis, R.S., Davis, A.M., Clayton, R. N. & Amari, S. 1998, *ApJ*, 504, 492
- [125] Palmerini, S., La Cognata, M., Cristallo, S., & Busso, M. 2011, *ApJ*, 729, 3
- [126] Palmerini, S., Sergi, M. L., La Cognata, M., Lamia, L., Pizzone, R. G., Spitaleri, C. 2013, *ApJ*, 764, 128P
- [127] Parker, E. N., *The instability of strong magnetic fields in stellar interiors*, 1974, *Ap&SS*, 31, 261-266
- [128] Piau, L., Kervella, P., Dib, S. & Hauschildt P. 2011, *A&A*, 526, A100
- [129] Piersanti, L., Cristallo, S., & Straniero, O. 2013, *ApJ*, 774, 98

- [130] Pignatari M., et al. 2013, ApJ, 762, 31
- [131] Pilachowski, C., Sneden, C., Freeland, E., & Casperson, J. 2003, AJ, 125, 794
- [132] Prada Moroni, P. G., Gennaro, M., Bono, G. et al. 2012, ApJ, 749, 108
- [133] Ramstedt, S., Schöier, F. L. & Olofsson, H., 2009, A&A 499, 515–527
- [134] Ramstedt, S. & Olofsson, H. 2014, A&A, 566A, 145R
- [135] Recio-Blanco, A., & de Laverny, P. 2007, A&A, 461, L13
- [136] Reimers, D. 1975, Mem. Soc. R. Sci. Liege, 6e Ser. 8, 369
- [137] Richer H. B., Olander N., Westerland B. E. 1979, ApJ, 230, 724
- [138] Rolfs, C. E., Rodney, W. S. 1988, *Cauldrons in the Cosmos* (Chicago: University of Chicago Press)
- [139] Sallaska, A. L., Iliadis, C., Champagne, A. E., Goriely, S., Starrfield, S., Timmes, F. X. 2013, ApJS, 207, 18
- [140] Salpeter, E., E. 1952a, Phys. Rev., 88, 547
- [141] Salpeter, E., E. 1952b, ApJ, 115, 326
- [142] Sandage, A. R., & Walker, M. F. 1966 ApJ, 413, 313
- [143] Schmidt, E. G. 1984, ApJ, 287, 261
- [144] Schöier, F. L. & Olofsson, H. 2001, A&A, 368, 969
- [145] Seeger, P. A., Fowler, W. A. & Clayton, D. D. 1965, ApJ Suppl., 11, 2
- [146] Sergi, L. et al. 2014, AIPC, 1594, 201S
- [147] Shaya W., 1999, MSc. Thesis, American University of Beirut

- [148] Shetrone, M. D. 2003, ApJ, 585, L45
- [149] Shwarzschild, M. & Härm, R. 1965, ApJ, 142, 855
- [150] Siess, L., Goriely, S., & Langer, N. 2004, A&A, 415, 1089
- [151] Siess, L. 2006, A&A, 448, 717
- [152] Smith, V. V. & Lambert D. L., 1986, ApJ, 311, 843
- [153] Smith V. V. & Lambert D. L. 1990, ApJS, 72, 387
- [154] Spillane, T., Raiola, F., Rolfs, C., et al. 2007, PhRvL, 98, 122501
- [155] Spruit, H. C., Overview of Solar Luminosity Variation Mechanisms, American Geophysical Union, Spring Meeting, 2001, American Geophysical Union, SP31, B01
- [156] Stancliffe, R., Tout, C. & Pols, O. R., 2004, Mon. Not. R. Astron. Soc., 352, 984
- [157] Stothers, R. B. 1991, ApJ, 383, 820
- [158] Stothers, R. B., & Chin, C. W. 1991, ApJ, 374, 288
- [159] Straniero, O., Gallino, R., Busso, M., Chieffi, A., Raiteri, C. M., Salaris, M., Limongi, M. 1995, AIPC, 327, 407S
- [160] Straniero, O., Chieffi, A., Limongi, M., Busso, M., Gallino, R., Arlandini, C. 1997, ApJ, 478, 332S
- [161] Straniero, O., Gallino, R., Cristallo, S. 2006, NuPhA., 777, 311S
- [162] Sweigart, A. V., & Mengel, J. G. 1979, ApJ, 229, 624
- [163] Tautvaišiene, G., Edvardsson, B., Tuominen, I., & Ilyin, I. 2000, A&A, 360, 499
- [164] Tautvaišiene, G., Edvardsson, B., Puzeras, E., & Ilyin, I. 2005, A&A, 431, 933

- [165] Tautvaišienė, G., Edvardsson, B., Puzeras, E., Barisevičius, G. & Ilyin, I. 2010, *Mon. Not. R. Astron. Soc.*, 409, 1213
- [166] Thé, L-S., El Eid, M. F., Meyer, B. 2007, *ApJ*, 655, 1058T
- [167] Trippella, O., Busso, M., Maiorca, E., Kappeler, F. & Palmerini, S. 2014, *ApJ*, 787, 41
- [168] Tsuji, T. 1991, *A&A*, 245, 203
- [169] Tsuji, T. 2008, *A&A*, 489, 1271
- [170] Umeda, H., & Nomoto, K. 1999, *ApJ*, 513, 861
- [171] Vassiliadis, E., & Wood, P. R., 1992, *Proc. ASA*, 10, 1
- [172] Ventura, P., Castellani, M. & Straka, C.W. 2005, *A&A*, 440, 623
- [173] Weiss, A., Serenelli, A., Kitsikis, A., Schlattl, H., & Christensen-Dalsgaard, J. 2005, *A&A*, 441, 1129
- [174] Whitelock, P.A., Feast, M.W., van Loon, J.Th., Zijlstra, A.A.: 2003, *MNRAS*, 342, 86
- [175] Winters, J. M., Le Bertre, T., Jeong, K. S., Nyman, L.-Å. & Epchtein, N. 2003, *A&A*, 409, 715
- [176] Zinner, E. 2005, in *Treatise of Geochemistry I. Meteorites, Comets, and Planets*, ed. A. M. Davis (Amsterdam: Elsevier), 17
- [177] Xu, H. Y., & Li, Y. 2004, *A&A*, 418, 213